
CHALMERS
UNIVERSITY OF TECHNOLOGY

# Dynamic Line Rating Based on Phasor Measurements: An Uncertainty Analysis

Master's thesis in Engineering Mathematics and Computational Science

Karl Olsson-Lalor

Department of Electrical Engineering

CHALMERS UNIVERSITY OF TECHNOLOGY
Gothenburg, Sweden 2026
www.chalmers.se

Master's thesis 2026

# Master's thesis in Engineering Mathematics and Computational Science

Karl Olsson–Lalor


CHALMERS

Department of Electrical Engineering
Chalmers University of Technology
Gothenburg, Sweden 2026

Dynamic Line Rating Based on Phasor Measurements: An Uncertainty Analysis
Karl Olsson-Lalor



Examiner: Jimmy Ehnberg, Department of Electrical Engineering, Chalmers University of Technology
Advisor: Tor Johansson, Vattenfall Eldistribution AB

Master's Thesis 2026
Department of Electrical Technology
Chalmers University of Technology
SE–412 96 Gothenburg
Telephone +46 31 772 1000

Typeset in LaTeX
Gothenburg, Sweden 2026

---

*Acknowledgements, dedications, and similar personal statements reflect the author's own views.*

Dynamic Line Rating Based on Phasor-Measurements: An Uncertainty Analysis

Karl Olsson-Lalor
Department of Electrical Engineering
Chalmers University of Technology

# Abstract

Rising electricity demand from energy-intensive technologies has heightened the need for reliable power transmission. Conventional static line ratings, based on conservative seasonal assumptions, often underutilize available capacity. Dynamic Line Rating (DLR) overcomes this by estimating ampacity from real-time conditions, but most implementations rely on extensive weather monitoring that limits scalability. Phasor-based DLR offers a scalable alternative by using synchronized voltage and current measurements to infer conductor temperature and power losses, enabling higher utilization without additional infrastructure.

This thesis investigates the theoretical performance of phasor-based DLR for short 130 kV overhead lines, with a focus on error propagation. Statistical inference methods are used to estimate conductor temperature from synthetic measurements while accounting for sensor accuracy. The impact of multiple measurements on estimating both static and dynamic estimation line parameters is examined.

The results show that single-measurement temperature estimates are fundamentally limited by amplified uncertainty in power loss calculations, requiring measurement accuracy improvements of at least two orders of magnitude over current standards. Multiple measurements improve accuracy and precision but require $10^3$-$10^5$ samples, depending on prior assumptions and sensor quality. Dynamic methods perform well under most conditions, achieving RMSEs of 0.8-2.6 °C for high-accuracy measurements, but abrupt current changes degrade accuracy while maintaining high model confidence, indicating model over-confidence.

These findings suggest that phasor-based DLR can reach accuracy levels comparable to weather-based approaches under ideal conditions, but practical deployment is constrained by measurement uncertainty, inference assumptions, and fundamental information limits. Further development of phasor-based DLR will require more robust uncertainty modelling, and stronger integration of physical priors in both static and dynamic estimation frameworks.

**Keywords:** Dynamic Line Rating, Conductor Temperature Estimation, Overhead Line, Temperature Estimation, Error Propagation, Bayesian Inference, Kalman Filtering

# Acknowledgements

I would first and foremost like to extend my gratitude to my advisor, Tor Johansson, for bringing this project to light, giving me the opportunity to carry it out, and providing great assistance throughout the entire process. It has truly been a wonderful cooperation, and I have greatly appreciated his enthusiasm and availability, both of which have greatly benefited me.

Alongside my advisor, Per Kriewitz, has also been of great help during the project, by assisting with documentation and operational experience in areas where I may lack experience, and for that I am very grateful.

This thesis has been full of hard work, stress, and untimely inconveniences, and throughout these tough times my family, partner Erika, and roommate Mikael, have all been of great moral support. I truly cannot describe the gratitude and love I feel for them for being there for me in all their own ways.

Lastly, I would like to extend my most enthusiastic and borderline excessive gratitude to Alina, whose contribution to this thesis cannot be measured in equations, figures, or appendices, but rather in morale, sanity, and timely laughter.

# Contents

# List of Acronyms

| Acronym | Meaning |
|---|---|
| MAE | Mean Absolute Error |
| RMSE | Root Mean Square Error |
| DLR | Dynamic Line Rating |
| OHL | Overhead Line |
| PACS | Protection and Control Systems |
| PMU | Phasor Measurement Unit |
| CT | Current Transformer |
| PT | Potential Transformer |
| ADC | Analog-to-Digital Converter |
| KDE | Kernel Density Estimator |
| HDI | Highest Density Interval |
| MC | Monte Carlo |
| UKF | Unscented Kalman Filter |
| HMC | Hamiltonian Monte Carlo |
| NUTS | No-U-Turn Sampler |

# 1 Introduction

With the rapid growth of energy-intensive technologies, ensuring a reliable supply of electricity has become essential for sustaining technological progress. A critical aspect of this challenge is guaranteeing that the power grid can transmit the required electrical energy without exceeding the ampacity limits of individual transmission lines. Expanding transmission capacity by constructing new transmission lines is often costly, time-consuming, and politically sensitive. Consequently, alternative strategies aimed at maximizing the utilization of existing infrastructure have gained significant attention.

Traditionally, transmission lines are rated using static seasonal assumptions, such as fixed summer or winter conditions. These conservative ratings frequently underestimate the actual real-time transmission capacity. By accurately determining conductor temperatures under prevailing operating and environmental conditions, Dynamic Line Rating (DLR) offers a more flexible and efficient approach, potentially unlocking additional transmission capacity without physical grid expansion [1].

For several years, Vattenfall Eldistribution AB has operated weather-based DLR on a limited number of transmission lines. This implementation relies on meteorological measurements, transmission line geometry, ground roughness mapping, and vendor-supplied computational models. While effective, this method requires extensive input data and considerable manual effort to accurately capture environmental effects on the transmission lines. Since conductor temperature depends on multiple factors—such as solar insolation, ambient temperature, wind speed, and wind direction—that may vary significantly over short spatial scales, this approach is considered difficult to scale across larger portions of the grid.

As a result, Vattenfall Eldistribution AB, along with other utilities, are investigating alternative DLR solutions with lower data and maintenance requirements. One such approach is phasor-based DLR, which utilizes synchronized voltage and current measurements at the sending and receiving ends of a transmission line. From these measurements, real-time power losses and conductor temperature estimates can be derived, enabling dynamic line ratings without direct reliance on weather measurements or detailed environmental modelling [2]. However, the accuracy and practical applicability of phasor-based conductor temperature estimation remain subjects requiring further investigation.

## 1.1 Aim and Purpose

The purpose of this thesis is to assess the potential of phasor-based measurement techniques as an alternative approach to DLR that reduces dependence on extensive weather data and detailed environmental modelling. By enabling conductor temperature estimation directly from synchronized electrical measurements, phasor-based DLR offers a potentially more scalable and operationally efficient solution for transmission system op-

erators.

To achieve this purpose, this thesis aims to investigate how accurately phasor measurements can be used to estimate the average conductor temperature of a transmission line and to compare the accuracy and precision of estimates with results obtained using established weather-based DLR methods.

## 1.2 Scope

The scope of this thesis is limited to a theoretical and simulation-based investigation of phasor-based DLR. The technical analysis begins with a detailed formulation of the governing equations underlying phasor-based DLR. The physical conditions under which these equations are derived are stated explicitly, along with the assumptions and simplifications involved, and the extent to which these assumptions may break down in practical applications. The expected deviations on temperature estimates due to modelling assumptions will then be calculated and discussed.

Measurement data used throughout the thesis are artificially generated, enabling controlled analysis of uncertainty propagation across different accuracy classes. The impact of measurement-chain imperfections is investigated, including device-related errors, time synchronization inaccuracies. In addition, the largest sources of estimation inaccuracy and imprecision are modelled to illustrate what to prioritise in terms of measurement accuracy improvement. In addition, the influence of transmission line parameters on temperature accuracy is assessed to identify the most suitable Overhead Lines (OHL) model types for this estimation method.

Both static and dynamic estimation frameworks are considered. Static Bayesian inference is used to study temperature estimation under stationarity assumptions and repeated measurements, providing a baseline for performance under controlled conditions. Dynamic approaches are implemented to relax these assumptions and allow for time-varying electrical and thermal quantities. Within the dynamic framework, multiple modelling scenarios are evaluated to assess performance across different operating conditions and measurement characteristics. This enables an investigation of the conditions under which dynamic modelling is reliable and practically applicable. Performance is evaluated using structured error metrics, and phasor-based DLR is benchmarked against weather-based DLR for contextual comparison.

## 1.3 Limitations

This thesis is limited to the analysis of 130 kV OHLs operating at currents close to, or above, their static ampacity. Since the primary objective of applying DLR is to increase the permissible current relative to static ratings, the results presented are only considered

relevant for high-load operating conditions. Lower current regimes are therefore outside the scope of this work and are not analysed further.

To reduce variability arising from differences in conductor geometry and material properties, the study is further limited to two specific conductor models currently used by Vattenfall Eldistribution. The first, Model Bohus, represents the thinnest conductor in use, with a cross-sectional area of 454 $mm^2$. The second, Model Gota, is a significantly thicker conductor with a cross-sectional area of 910 $mm^2$. Both conductor types are analysed at fixed line lengths. These lengths are provided by Vattenfall Eldistribution and are each approximately 20 km, chosen to represent a median length of the company's 130 kV overhead line installations. The maximum operational temperature ($T_{MO}$) varies between individual overhead lines depending on conductor design and operational standards. At Vattenfall Eldistribution AB, conductors are typically designed for a maximum operating temperature of either 50 °C or 70 °C. To constrain the scope of the study while still allowing for occasional exceeding of nominal temperature limits, simulations and calculations are restricted to cases where the average conductor temperature does not exceed 70 °C.

Variations in system frequency are not considered. The analysis assumes a constant system frequency, with current and voltage having identical frequencies and differing only by a phase shift. This assumption is consistent with standard power system operation under steady-state conditions.

Measurement and modelling errors are assumed to be random, independent and identically distributed. Systematic errors, correlated disturbances, and long-term sensor drift are not explicitly modelled.

Finally, this thesis focuses on the statistical estimation of conductor temperature rather than detailed electromagnetic or transmission line modelling. As a result, the transmission line is represented using a lumped-parameter $\pi$-model. For the line lengths considered in this work, approximately 20 km, the $\pi$-model provides sufficient accuracy and is significantly more precise than simplified models recommended for such lengths. More detailed distributed-parameter models are therefore not considered necessary for the purposes of this study.

## 1.4 Societal, ethical and ecological implications

Beyond the technical and economic advantages of phasor-based DLR, its wider implications for society, ethics, and the environment deserve careful consideration. As the technology influences how electricity is delivered, who benefits from its deployment, and how it interacts with sustainability goals, it is important to look beyond operational efficiency. The following sections highlight key societal, ethical, and ecological dimensions that shape the broader impact of implementing phasor-based DLR.

Societal implications of phasor-based DLR are largely positive. DLR improves grid

reliability and resilience by providing more accurate assessments of safe operating limits, reducing the risk of overloads and outages [1, 3]. It can also lower system costs by deferring or avoiding expensive new transmission projects, potentially benefiting consumers through more affordable electricity [4]. Importantly, DLR enables higher renewable integration by relieving congestion, which supports a fairer and broader access to clean energy [2]. However, implementation requires some advanced sensing and communication infrastructure. If network owners Protection And Control Systems (PACS) are up-to-date, phasor measurements should be technically and economically viable. This level of sophistication may well be adopted for higher voltages even in less developed countries [5], as a reliable PACS is an integral part of any transmission line investment. The other pre-requisite concerns advanced time synchronization. GPS, being a global system, should be accessible for any utility. Therefore, regions generally lacking in financial or technical resources would not necessarily need to be left behind. Additionally, there exists a certain risk with relying too much on DLR estimates. With the current use of static line ratings there are large safety margins in place to ensure that line temperatures never exceed the maximum temperature they were designed for [6]. With the application of DLR, these safety margins are minimized for the purpose of efficiency, which comes at the cost of increasing the risk of surpassing designed maximum temperatures which would be a safety issue.

The Ethical implications center on the balance between efficiency and risk. DLR allows lines to operate closer to their physical limits, increasing utilization but reducing traditional safety margins. Operators and regulators must weigh the pursuit of efficiency against their responsibility to ensure public safety and service continuity. There are also concerns about the equitable distribution of benefits and costs: if financial gains primarily accrue to utilities or large industrial users while costs are socialized, fairness may be questioned [7]. As utilities typically are state regulated monopolies, implementation of a new technology such as phasor-based DLR calls for updated regulations. Thus, both costs and benefits can be duly socialized in accordance to domestic circumstances. Additionally, DLR relies on complex models and algorithms, raising issues of transparency, accountability, and public trust—especially in the event of failures.

Ecological implications of DLR are mostly positive. By maximizing the capacity of existing infrastructure, DLR reduces or delays the need for new transmission lines, avoiding ecological disruption from land-use change, deforestation, and habitat fragmentation. It also facilitates deeper penetration of renewables, supporting decarbonization goals [1]. Nonetheless, the technology itself has an environmental footprint. The production, deployment, and eventual disposal of sensors, communication hardware, and supporting ICT infrastructure carry impacts in terms of material use, energy demand, and electronic waste [8]. This footprint should however be compared to the alternative for building new, or upgrade existing, transmission lines.

In summary, phasor-based DLR can significantly support the energy transition by improving efficiency, enabling renewable integration, and reducing ecological harm from new infrastructure. At the same time, it raises important societal and ethical questions about equity, risk management, and transparency. Addressing these concerns will be essential for ensuring that the benefits of DLR are shared broadly and sustainably.

## 1.5 Thesis structure

This thesis is organized to progressively develop the theoretical background, methodology, and analysis required to evaluate phasor-based temperature estimation for dynamic line rating. It begins by introducing the relevant technical and physical background related to transmission line modelling, DLR, and phasor measurements. This includes requirements on estimation precision, applicable standards governing phasor measurement accuracy, and the basis for comparing weather-based and phasor-based DLR approaches.

The thesis then presents the mathematical foundations of uncertainty propagation and statistical inference. This section details the theoretical principles underlying the employed methods and highlights the key factors that influence methodological choices and estimation performance.

Subsequently, the methodology chapter describes the selected approaches for uncertainty propagation, variance decomposition, and temperature inference. Both analytical relationships and numerical case studies are introduced, along with the computational frameworks used to implement and evaluate the proposed methods.

Finally, the results are presented and analysed, followed by a discussion that interprets the findings in light of the underlying assumptions, limitations, and practical implications for phasor-based dynamic line rating.

# 2 Technical and Physical Background

This section aims to explain the necessary background to follow this thesis. It will begin by describing the operational constraints imposed on OHLs, detailing the necessity of precise temperature estimation for transmission lines from a regulatory perspective. This will be followed by a physical explanation of how current and voltage phasors are modelled in transmission lines, and common lumped-sum approximations. Next, both weather and phasor-based DLR will be explained, along with similarities and differences between the two methods as well as derivations of the deterministic temperature equation for phasor-based DLR. Finally, the acquisition of phasor measurements is described, describing the measurement chain. This part will also explain the cause, nature and magnitude of phasor measurement errors.

## 2.1 Operational Constraints of Overhead Lines and the Role of Conductor Temperature

The maximum permissible current of an overhead transmission line is ultimately constrained by mechanical and safety considerations rather than purely electrical limits.

As current increases, resistance causes temperature to rise, which in turn leads to expansion of the conductor material. This expansion results in increased sag which reduces ground clearance and thus potentially violates safety requirements Insufficient clearance may pose risks such as contact with vegetation, structures, or the public, and is therefore a primary operational constraint for overhead lines [6, 9].

Although conductor sag is the physical quantity linked to safety regulations, it is rarely measured or monitored directly in power systems such as the ones in question. Instead, conductor temperature is commonly used as a proxy variable, since sag is a deterministic function of temperature for fixed mechanical conditions [10]. By ensuring that the conductor temperature remains below a specified thermal limit, compliance with statutory ground-clearance requirements can be maintained with an appropriate safety margin. Since conductor sag is strongly temperature dependent, uncertainties in temperature estimation translate directly into clearance uncertainty, and it is thus important to ensure that the temperature is not being significantly underestimated. Engineering guidance therefore specifies acceptable tolerances in thermal calculations linked to sag accuracy. CIGRE and IEEE report that sag deviations corresponding to conductor temperature differences of approximately 10-15 °C represent the upper bound of engineering accuracy in line thermal assessments, with 10 °C commonly adopted as a conservative design tolerance [11].

DLR techniques are based on this principle. Rather than limiting current according to conservative worst-case assumptions, DLR allows higher ampacity by estimating the

conductor temperature under prevailing environmental and loading conditions. Accurate knowledge of the exact sag is therefore not required; it is sufficient to estimate conductor temperature with adequate accuracy and confidence to ensure that sag-related clearance limits are not exceeded. This makes conductor temperature a central state variable for both safe operation and the practical implementation of DLR. Operational monitoring and DLR applications typically target substantially lower temperature uncertainties to preserve clearance margins in real time. For the conductor models considered in this work, a safety margin of 5 °C is adopted; thus, temperature estimation methods should achieve accuracies well within ±5 °C to ensure reliable compliance with clearance constraints.

Consequently, this thesis focuses on the estimation of conductor temperature as the key enabler for increased transmission capacity and keeps mechanical modelling of sag outside its scope.

## 2.2 Transmission Line Modelling

Transmission lines are spatially distributed systems that convey electrical power over long distances. Their behaviour is fundamentally governed by Maxwell's equations, but for power-frequency operation these can be simplified into one-dimensional telegrapher's equations that describe the voltage and current as functions of distance $x$ and time $t$.

### 2.2.1 Derivation of Distributed-Parameter Model

Consider a differential segment of length $\Delta x$ within a transmission line. Let $\widetilde{V}(x,t)$ and $\widetilde{I}(x,t)$ denote instantaneous voltage and current at position $x$ and time $t$, respectively. Each infinitesimal segment is characterized by per-unit-length parameters:

- R [Ω /m]: series resistance (accounts for conductor losses),
- L [H/m]: series inductance (accounts for magnetic coupling),
- G [S/m]: shunt conductance (dielectric losses),
- C [F/m]: shunt capacitance (electric field storage).

Assuming sinusoidal steady-state operation with angular frequency $\omega$, yields the Telegrapher's equations (2.1):

$$\frac{\partial \widetilde{V}(x)}{\partial x} = -\left(R + j\omega L\right) I(x), \qquad \frac{\partial \widetilde{I}(x)}{\partial x} = -\left(G + j\omega C\right) V(x). \tag{2.1}$$

Differentiating once more in terms of $x$ yields

$$\frac{d^2\widetilde{V}}{dx} = \gamma^2 V, \qquad \frac{d^2\widetilde{I}}{dx} = \gamma^2 I,$$

with the propagation constant ($\gamma$) and characteristic impedance $Z_c$ defined as

$$\gamma = \sqrt{(R + j\omega L)(G + j\omega C)}, \qquad Z_c = \sqrt{\frac{R + j\omega L}{G + j\omega C}}.$$

The general solutions to these differential equations are

$$\widetilde{V}(x) = \widetilde{V}^{+}e^{-\gamma x} + \widetilde{V}^{-}e^{\gamma x}, \qquad \widetilde{I}(x) = \frac{1}{Z_c}\left(\widetilde{V}^{+}e^{-\gamma x} + \widetilde{V}^{-}e^{\gamma x}\right), \tag{2.2}$$

representing the forward and backward travelling waves.

### 2.2.2 Approximations and Lumped-Parameter Models

Although equation (2.2) describes the full distributed behaviour, for most power-system studies the line are usually approximated by lumped equivalents depending on the transmission line's length ($l$). To this end, we define $\widetilde{V}^{(r)}$ and $\widetilde{I}^{(r)}$ as the voltage and current received at one end of the transmission line, as well as $\widetilde{V}^{(s)}$ and $\widetilde{I}^{(s)}$ as the voltage and current sent from the other end.

1. **Short Line Approximation (<80 km)** When $\gamma \ll 1$, the effect of shunt capacitance is negligible. The line reduces to a simple series impedance, where $I$ is assumed constant and
$$\widetilde{V}^{(s)} = \widetilde{V}^{(r)} + (R + j\omega L)\,\widetilde{I}. \tag{2.3}$$

2. **Medium Line Approximation (80-250 km)** capacitance is modelled by shunt elements at each end, yielding the **$\pi$-model**:
$$\begin{bmatrix}\widetilde{V}^{(s)}\\ \widetilde{I}^{(s)}\end{bmatrix} = \begin{bmatrix}1 + \frac{1}{2}YZ & Z\\ Y\left(1 + \frac{1}{4}YZ\right) & 1 + \frac{1}{2}YZ\end{bmatrix}\begin{bmatrix}\widetilde{V}^{(r)}\\ \widetilde{I}^{(r)}\end{bmatrix}, \tag{2.4}$$
where
$$Z = (R + j\omega L), \qquad Y = j\omega C l.$$

### 2.2.3 Resistance Temperature Dependece

The conductor resistance varies with temperature according to the temperature coefficient differential law:

$$\frac{dR}{dT} = \alpha R, \tag{2.5}$$

where some initial condition $R_{AC} = R(T_{\text{ref}})$ is given, and $\alpha$ is temperature independent. The analytical solution to this differential equation is

$$R = R_{AC}e^{\alpha(T - T_{\text{ref}})},$$

and in most cases it is linearly approximated using the Taylor expansion of $e^x$, yielding

$$R = R_{AC}\left(1 + \alpha\left(T - T_{\text{ref}}\right)\right) + \mathcal{O}\left(\alpha^2\left(T - T_{\text{ref}}\right)^2\right), \tag{2.6}$$

where $\mathcal{O}\left(\alpha^2\left(T - T_{\text{ref}}\right)^2\right)$ is the order of error caused by the approximation.

### 2.2.4 Transmission Line Parameters

The main transmission line parameters used in this thesis are those for the Gota and Bohus lines of Vattenfall Eldistribution AB, which have been chosen to represent the median lengths for thick and thin transmission lines, respectively. The parameters for these lines are as shown in Table 2.1. Only 130kV OHLs are considered, and thus each individual conductor of the transmission line will have a voltage slightly above $130000/\sqrt{3}$.

Table 2.1: Transmission line parameters for models Bohus and Gota.

| Model | Quantity | Value | Unit |
|---|---|---|---|
| Bohus | $l$ | 17.25 | km |
| | A | 454 | $\text{mm}^2$ |
| | $R_{\text{AC}}$ | 0.0729 | $\Omega$/km |
| | $\alpha$ | 0.00403 | 1/K |
| | $\omega L$ | 0.38 | $\Omega$/km |
| | $T_{MO}$ | 70 | °C |
| | $I^A_{\text{RATE}}$ | 1009 | A |
| | $I^C_{\text{RATE}}$ | 813 | A |
| Gota | $l$ | 21.95 | km |
| | A | 910 | $\text{mm}^2$ |
| | $R_{\text{AC}}$ | 0.0348 | $\Omega$/km |
| | $\alpha$ | 0.00403 | 1/K |
| | $\omega L$ | 0.38 | $\Omega$/km |
| | $T_{MO}$ | 70 | °C |
| | $I^A_{\text{RATE}}$ | 1625 | A |
| | $I^C_{\text{RATE}}$ | 1305 | A |

## 2.3 Dynamic Line Rating

DLR refers to methods that determine the permissible current or operating temperature of an overhead transmission line based on actual operating conditions rather than conservative worst-case assumptions. Two separate approaches to DLR are weather-based line rating and phasor-based line rating. While both aim to increase transmission capacity without breaking thermal constraints, they differ fundamentally in the type of measurements they rely on and their sources of uncertainty.

**Weather-based line rating** Weather-based line rating determines the conductor ampacity by explicitly solving the thermal balance equation using measured or estimated environmental conditions. The method requires real-time measurements of weather variables such as ambient temperature, wind speed and direction, and solar radiation, typically obtained from weather stations installed near the transmission line itself. These measurements are used as inputs to a physical thermal model of the conductor, commonly based on standards and recommendations such as *Thermal Behaviour of Overhead Conductors* [3] or *IEEE Standard for Calculating the Current-Temperature Relationship of Bare Overhead Conductors* [6].

Using the measured weather data, the steady-state or transient conductor temperature is calculated, and the maximum allowable current is determined such that a predefined temperature limit is not exceeded. As a result, weather-based DLR directly links ampacity to external cooling conditions and solar heating. However, this approach depends strongly on the accuracy of the weather measurements, and the sensor coverage as local variations in wind or solar exposure along the line may not be fully captured by a limited number of sensors.

Weather-based DLR systems have reached a level of maturity that enables reasonably accurate conductor temperature estimation. Reported root-mean-square errors (RMSE) range between 1.57 °C and 2.61 °C, depending on the specific modelling approach and meteorological input data [12]. The validation study in Martinez et al. [12] was conducted on 220 kV overhead lines, whereas the present work considers 130 kV lines. Sensor comparison studies on 100kV further show that parallel temperature measurements typically deviate by less than 2.23 °C in 75 % of observations, with median deviations around 0.94 °C, and manufacturer-specified accuracies on the order of ±1 °C [13]. Review literature similarly places the accuracy of surface temperature sensing in the range of 1-2 °C, while noting that single-point measurements may not fully capture spatial thermal variability along a span [14].

Complementary evidence from direct line-monitoring deployments indicates higher temperature accuracy when using conductor-mounted sensing technologies. Field evaluations on 110 kV overhead lines report temperature measurement accuracies of approximately ±1 °C within a 95 % confidence interval [13].

**Phasor-based line rating** Phasor-based line rating determines conductor temperature and ampacity indirectly from synchronized electrical measurements. Using voltage and current phasors, typically obtained from PMUs, the method tracks temperature-dependent variations in line parameters, most notably conductor resistance. From these electrically inferred parameter changes, an average conductor temperature can be estimated and evaluated against thermal operating limits.

Because the temperature estimate is derived from electrical system behaviour, environ-

mental influences such as wind cooling and solar heating are inherently embedded in the measurements rather than explicitly modelled. This removes the need for detailed thermal balance calculations and dedicated weather instrumentation, shifting the methodological emphasis toward accurate line parameter modelling and high-quality synchronized data acquisition.

The principal uncertainties in phasor-based DLR therefore arise from measurement noise, parameter-identification errors, and modelling assumptions. Moreover, the inferred temperature typically represents an electrically equivalent average over the monitored line section, limiting the method's ability to resolve localized thermal hot spots.

**Comparison of the two approaches** Both weather-based and phasor-based DLR seek to increase transmission utilization while ensuring compliance with thermal limits, yet they differ primarily in how conductor temperature is observed and where uncertainty enters the rating process. Weather-based methods estimate temperature through a forward thermal model driven by environmental measurements, whereas phasor-based methods infer temperature indirectly from electrically observed changes in line parameters.

A key distinction therefore lies in observability. Weather-based DLR provides a physics-explicit description of the conductor heat balance and can resolve the influence of individual cooling and heating mechanisms. However, its accuracy depends on the representativeness and spatial coverage of meteorological measurements along the line. Phasor-based DLR, by contrast, captures the net thermal state of the conductor as reflected in electrical behaviour, inherently incorporating the aggregate effect of environmental conditions without requiring direct weather inputs.

This difference also affects spatial resolution. Weather-based approaches can, in principle, identify localized thermal constraints if sufficient sensor coverage is available, while phasor-based methods yield an averaged temperature over the monitored line section. Consequently, phasor-based ratings may be less sensitive to localized hot spots, whereas weather-based ratings may be more sensitive to local meteorological variability.

In practice, the two approaches can be viewed as complementary: weather-based DLR offers physically interpretable and spatially aware thermal insight, while phasor-based DLR provides system-integrated temperature averages derived from electrical measurements.

### 2.3.1 Relationship between current, temperature, and ampacity.

The temperature of an overhead transmission line is governed by the balance between internally generated heat and heat exchanged with the surrounding environment. Under steady-state conditions, the conductor temperature $T$ is determined by an equilibrium between heat gains and heat losses. For overhead conductors, this steady-state heat

balance can be written as [3, 6]

$$P_{\mathrm{J}} + P_{\mathrm{S}} = P_{\mathrm{C}} + P_{\mathrm{R}}, \tag{2.7}$$

where $P_{\mathrm{J}}$ is Joule heating, $P_{\mathrm{S}}$ denotes absorbed solar radiation, $P_{\mathrm{C}}$ is convective heat loss to the surrounding air, and $P_{\mathrm{R}}$ is radiative heat loss.

The dominant internal heat source is Joule heating caused by the current $I$, which can be expressed as

$$P_{\mathrm{J}} = I^2 R(T), \tag{2.8}$$

where $R(T)$ is the temperature-dependent electrical resistance of the conductor. For typical conductor materials, the resistance may be approximated as a linear function of temperature as per Equation (2.6).

### 2.3.2 Electrical Power Loss Representation Using Phasors

Over a transmission line, the Joule heating power $P_{\mathrm{J}}$ is equal to the real power loss $P_\ell$ in the conductor. This loss can be expressed using complex voltage and current phasors at the sending and receiving ends of the line as

$$\begin{aligned} P_{\mathrm{J}} = P_\ell &= \Re\left(\widetilde{V}^{(s)}\widetilde{I}^{(s)*} - \widetilde{V}^{(r)}\widetilde{I}^{(r)*}\right), \\ &= \nu^{(s)}\iota^{(s)}\cos\left(\theta_\nu^{(s)} - \theta_\iota^{(s)}\right) - \nu^{(r)}\iota^{(r)}\cos\left(\theta_\nu^{(r)} - \theta_\iota^{(r)}\right), \\ &= s^{(s)}\cos\left(\phi^{(s)}\right) - s^{(r)}\cos\left(\phi^{(r)}\right), \end{aligned} \tag{2.9}$$

where $(\cdot)^{(s)}$ and $(\cdot)^{(r)}$ denote sending and receiving ends, respectively, $\nu$ and $\iota$ are voltage and current magnitudes, $\theta_\nu$ and $\theta_\iota$ their corresponding phase angles, $s$ is the apparent power, and $\phi$ is the power factor angle.

### 2.3.3 Joule Heating in Overhead Line Conductors

For alternating current operation, the generated thermal power can be expressed as

$$P_{\mathrm{J}} = k_j I_{AC}^2 R_{AC} l \left(1 + \alpha \left(T_{\mathrm{AV}} - T_{\mathrm{ref}}\right)\right), \tag{2.10}$$

where $k_j$ is an experimentally determined correction factor accounting for non-ideal effects such as skin and proximity effects, $T_{\mathrm{AV}}$ denotes the average conductor temperature over the considered line section, and $I_{\mathrm{AC}} = \sqrt{\left(\iota^{(s)}\right)^2 + \left(\iota^{(r)}\right)^2}$ is the effective current.

Rearranging the expression yields an explicit relationship between Joule heating and the average conductor temperature,

$$T_{\mathrm{AV}} = T_{\mathrm{ref}} + \frac{1}{\alpha}\left(\frac{P_{\mathrm{J}}}{k_j I_{AC}^2 R_{AC} l} - 1\right). \tag{2.11}$$

This expression provides a direct link between electrical quantities and average temperature, forming the basis for temperature estimation from electrical measurements. Substituting the electrical loss expression (2.9) into (2.11) yields a closed-form relationship between synchronized phasor measurements and the average conductor temperature. This relationship constitutes the main thermal-electrical coupling equation used in this thesis and enables temperature estimation based solely on electrical measurements and conductor properties, without direct observation of environmental conditions.

## 2.4 Phasor Measurements

PMUs provide time-synchronized measurements of electrical quantities in transmission lines delivered in the form of phasor representations of voltages and currents. These are then referenced to a common time source, allowing direct comparison of measurements taken at geographically different locations [15].

Acquisition of analog voltage and current signals from the power system are typically done via voltage transformers (VTs) or current transformers (CT), depending on the measured quantity. These signals represent instantaneous waveforms of the system quantities at the PMU location. The waveforms are sampled at a fixed sampling rate by an Analog-to-Digital Converter (ADC), and the resulting discrete-time signals are then used to estimate the phasor quantities. Under steady-state conditions, a sinusoidal voltage or current signal can be represented by a phasor. PMUs therefore compute the phasor magnitude and phase angle of the voltage and current signals.

A defining characteristic of PMU measurements is their precise time synchronization. Each PMU is equipped with a time reference [16], which ensures that phasor estimates are aligned to a global time reference, often with sub-microsecond accuracy. As a result, phaser quantities measured by different PMUs across the power system are directly comparable.

While PMUs are designed to provide highly accurate and time-aligned phasor measurements, the measurement process is subject to various sources of error. These include imperfections in instrument transformers, synchronization inaccuracies, noise, and quantization effects, which will be discussed in the following sections.

### 2.4.1 Noise and Uncertainty in Phasor Measurements

When measuring voltage and current phasors using PMUs, uncertainty is introduced at multiple stages of the measurement chain. These uncertainties originate from the PMU internal hardware, including ADCs and digital signal processing, as well as from external components such as instrument transformers and secondary circuits. To enable an uncertainty analysis, the dominant sources of error are quantified and categorized according to their physical origin.

The uncertainty bounds associated with PMU-internal effects and secondary circuit or signal chain errors are summarized in Tables 2.2 and 2.3 for voltage and current measurements, respectively. PMU internal calibration errors represent residual magnitude and phase inaccuracies inherent to the PMU after factory calibration. Secondary circuit uncertainties account for errors introduced by burden effects, analog input stages, and scaling within the PMU. In the case of voltage measurements, a systematic secondary circuit offset is additionally considered to model bias caused by cabling, which is omitted for current measurements.

Table 2.2: Error bounds for voltage PMU measurements and secondary circuit / signal chain errors.

| Cause | | Magnitude [%] | | Angle [min] | Source |
|---|---|---|---|---|---|
| PMU internal calibration | $R_{VU}$ | $\pm 0.04$ | $\Theta_{VU}$ | $\pm 2$ | [a] |
| Secondary circuit offset | $R_{VS_O}$ | $\{-0.05, 0\}$ | $\Theta_{VS_O}$ | 0 | [a] |
| Secondary circuit uncertainty | $R_{VS_U}$ | $\pm 1$ | $\Theta_{VS_U}$ | $\pm 12$ | [17] |

[a] Expert assessment.

Table 2.3: Error bounds for current PMU measurements and secondary circuit / signal chain errors.

| Cause | | Magnitude [%] | | Angle [min] | Source |
|---|---|---|---|---|---|
| PMU internal calibration | $R_{CU}$ | $\pm 0.04$ | $\Theta_{VU}$ | $\pm 2$ | [a, b] |
| Secondary circuit uncertainty | $R_{CS_U}$ | $\pm 1$ | $\Theta_{VS_U}$ | $\pm 12$ | [17] |

[a] Expert assessment.
[b] Manufacturer.

Uncertainties arising from instrument transformers are treated separately and summarized in Table 2.4. These include ratio errors affecting the measured magnitude and phase displacement errors affecting the measured phase angle. The bounds are specified according to standardized accuracy classes for VTs and CTs. By explicitly parameterizing transformer uncertainties by accuracy class, the analysis can be adapted to different substation configurations and measurement installations. The stochastic variables for voltage and current transformer errors follow the same nomenclature as other sources of error, with $R_{VT}$ and $R_{CT}$ for magnitude, as well as $\Theta_{VT}$ and $\Theta_{CT}$ for angle.

Together, the uncertainty models presented in Tables 2.2–2.4 form the basis for the subsequent analysis of phasor measurement errors.

### 2.4.2 Synchronization of Phasor Measurements

In addition to the magnitude and phase uncertainties discussed in the previous section, phasor measurements are subject to errors arising from imperfect time synchronization between geographically distributed measurement units. PMUs estimate voltage and current phasors from simultaneously sampled waveforms and associate each estimate with

Table 2.4: Error bounds for errors caused by voltage and current transformers uncertainty for different accuracy classes.

| Type | Class | Magnitude [%] | Angle [Minutes] | Source |
|---|---|---|---|---|
| Voltage Transformer | 0.2S | ±0.2 | ±10 | [18, 19] |
| | 0.5S | ±0.5 | ±30 | [18, 19] |
| Current Transformer | 0.1 | ± 0.1 | ± 5 | [19] |
| | 0.2 | ±0.2 | ±10 | [19] |
| | 0.5 | ±0.5 | ±10 | [19] |
| | 5P | ±1 | ±60 | [19] |

a time stamp derived from a common time reference. While sampling within a single PMU is internally synchronized, small timing mismatches may exist between different measurement stations.

According to the synchrophasor measurement standard, the maximum time synchronization error between PMUs is on the order of one microsecond, corresponding to a small but finite phase angle error at the nominal system frequency [17]. For the class of systems considered in this thesis, these synchronization errors are assumed to be negligible. As demonstrated in [20], even abrupt changes in convective heat dissipation do not result in immediate or rapid variations in conductor temperature, implying that the underlying voltage and current magnitudes evolve slowly relative to the time scales associated with PMU synchronization accuracy.

It should nevertheless be noted that the scope of this thesis includes the estimation of voltage and current phasors themselves, rather than solely derived steady-state quantities. Consequently, the omission of synchronization errors should be reconsidered in applications involving rapidly varying electrical conditions, such as fast transients, protection studies, or systems with significant frequency deviations.

For a system operating at a stable and uniform frequency, without abrupt changes in voltage or current amplitude, the time-average of the instantaneous real power associated with the phasor product $\widetilde{V}\widetilde{I}^*$ remains constant under short periods of time. Under such steady-state conditions, small relative time shifts between synchronized measurements do not affect the averaged power quantities considered in this work.

# 3 Mathematical Theory

## 3.1 Complex Phasors

A complex phasor provides a mathematical representation of sinusoidal functions through the use of complex exponentials. Consider a real-valued sinusoidal function

$$x(t) = A\cos(\omega t + \phi), \tag{3.1}$$

where $A \in \mathbb{R}^+$ denotes the RMS-magnitude, $\omega \in \mathbb{R}$ the angular frequency, and $\phi \in \mathbb{R}$ a phase offset. Using Euler's identity, this function can be written as

$$x(t) = \Re\{Ae^{j(\omega t+\phi)}\} = \Re\{(Ae^{j\phi})e^{j\omega t}\}. \tag{3.2}$$

The complex constant

$$\widetilde{X} = Ae^{j\phi} = A\angle\phi \tag{3.3}$$

is defined as the complex phasor associated with $x(t)$. The time dependence is fully contained in the exponential term $e^{j\omega t}$, while the phasor $\widetilde{X}$ encodes the amplitude and phase of the sinusoid.

The phasor representation establishes a relation between sinusoidal functions and complex numbers in the exponential form. This relation can be viewed as a mapping

$$\mathcal{P} : A\cos(\omega t + \phi) \;\mapsto\; \widetilde{X} = Ae^{j\phi}, \tag{3.4}$$

together with the inverse mapping

$$\mathcal{P}^{-1}(\widetilde{X}) = \Re\{\widetilde{X}e^{j\omega t}\}. \tag{3.5}$$

### 3.1.1 Complex Conjugation

Complex conjugation plays a central role in maintaining the correspondence between real-valued and complex-valued representations. The conjugate of the exponential function is given by

$$\left(e^{j\omega t}\right)^* = e^{-j\omega t}, \tag{3.6}$$

and thus, for a general phasor $\widetilde{X} = Ae^{j\phi}$,

$$\widetilde{X}^* = \left(Ae^{j\omega t}\right)^* = Ae^{-j\omega t}. \tag{3.7}$$

The real-valued sinusoid can equivalently be expressed as the mean of a complex exponential and its conjugate:

$$x(t) = \frac{1}{2}\left(\widetilde{X}e^{j\omega t} + \widetilde{X}^* e^{-j\omega t}\right). \tag{3.8}$$

This form demonstrates that every real sinusoidal function corresponds to a symmetric pair of complex exponentials located at frequencies $+\omega$ and $-\omega$. The conjugate pair ensures that the imaginary components cancel, leaving a purely real function.

Complex conjugation also preserves important algebraic symmetries. For instance, the magnitude of a phasor is invariant under conjugation:

$$|\widetilde{X}|^2 = \widetilde{X}\widetilde{X}^*, \tag{3.9}$$

and the conjugate of a product satisfies

$$(\widetilde{A}\widetilde{B})^* = \widetilde{A}^*\widetilde{B}^*, \tag{3.10}$$

for all $\widetilde{A}, \widetilde{B} \in \mathbb{C}$, where $\mathbb{C}$ is the complex plane.

In summary, complex conjugation acts as a reflection across the real axis in the complex plane, enforcing the condition of being real-valued in signals and preserving the analytic structure of phasor representations.

## 3.2 Uncertainty and Error Propagation

Most experimental measurements and numerical simulations are subject to uncertainty due to limitations in measurement instruments, numerical approximations, and modelling assumptions. Quantifying these uncertainties and understanding how they propagate through mathematical models is essential for assessing the reliability and accuracy of results.

### 3.2.1 Types of Uncertainty

Uncertainty can generally be classified into two categories: systematic and random uncertainties. Systematic uncertainties arise from consistent biases such as calibration errors or modelling assumptions and tend to shift results in a predictable manner. Random uncertainties, on the other hand, originate from stochastic variations such as measurement noise or numerical round-off errors and are typically characterized using statistical methods.

### 3.2.2 Representation of Uncertainty

Let a quantity $x$ be measured or estimated with an associated uncertainty $\Delta x$. The result is commonly expressed as

$$x = \bar{x} \pm \Delta x, \tag{3.11}$$

where $\bar{x}$ denotes the best estimate, typically the mean value, and $\Delta x$ represents the standard uncertainty, often taken as the standard deviation.

For multiple independent variables $x_1, x_2, \ldots, x_n$ with uncertainties $\Delta x_1, \Delta x_2, \ldots, \Delta x_n$, uncertainty propagation must be considered when evaluating a function

$$y = f(x_1, x_2, \ldots, x_n). \tag{3.12}$$

### 3.2.3 Error Propagation Using Linear Approximation

Assuming the uncertainties are small and the function $f$ is sufficiently smooth, the propagated uncertainty in $y$ can be approximated using a first-order Taylor expansion. The total differential of $y$ is given by

$$\mathrm{d}y = \sum_{i=1}^{n} \frac{\partial f}{\partial x_i} \mathrm{d}x_i. \tag{3.13}$$

If the input variables are uncorrelated, the variance of $y$ is

$$(\Delta y)^2 = \sum_{i=1}^{n} \left( \frac{\partial f}{\partial x_i} \right)^2 (\Delta x_i)^2, \tag{3.14}$$

which leads to the standard uncertainty

$$\Delta y = \sqrt{\sum_{i=1}^{n} \left( \frac{\partial f}{\partial x_i} \right)^2 (\Delta x_i)^2}. \tag{3.15}$$

This formulation is commonly referred to as the Gaussian error propagation law and is widely used due to its simplicity and general applicability.

### 3.2.4 Correlated Uncertainties

When the input variables are correlated, covariance terms must be included. The propagated variance then becomes

$$(\Delta y)^2 = \sum_{i=1}^{n} \left( \frac{\partial f}{\partial x_i} \right)^2 (\Delta x_i)^2 + 2 \sum_{i=1}^{n} \sum_{j=i+1}^{n} \frac{\partial f}{\partial x_i} \frac{\partial f}{\partial x_j} \operatorname{Cov}(x_i, x_j), \tag{3.16}$$

where $\operatorname{Cov}(x_i, x_j)$ denotes the covariance between $x_i$ and $x_j$.

### 3.2.5 Relative Uncertainty

For multiplicative or power-law relationships, it is often convenient to express uncertainty in relative form. For a quantity

$$y = \prod_{i=1}^{n} x_i^{a_i}, \tag{3.17}$$

the relative uncertainty is approximated by

$$\left(\frac{\Delta y}{y}\right)^2 = \sum_{i=1}^{n} a_i^2 \left(\frac{\Delta x_i}{x_i}\right)^2, \tag{3.18}$$

assuming uncorrelated variables.

### 3.2.6 Limitations

The linear error propagation method assumes small uncertainties and neglects higher-order terms in the Taylor expansion. For strongly non-linear models or large uncertainties, this approximation may become inaccurate. In such cases, alternative methods such as Monte Carlo (MC)simulations are useful, after which one can estimate the probability density.

## 3.3 Monte Carlo Simulation

A MC simulation is a stochastic numerical method based on repeated random draws from probability distributions to approximate statistical properties of a system. The method is particularly useful when analytical analysis is impractical due to complex model structure or nonlinearity [21].

Consider a model described by a mapping

$$Y = \mathcal{F}(\boldsymbol{X}) \tag{3.19}$$

where $\boldsymbol{X} = (X_1, X_2, \ldots, X_d)$ is a vector of random input variables. Each input variable is characterized by a prescribed probability distribution reflecting its uncertainty or variability. In an MC simulation, a large number $N$ or independent realizations $\{\boldsymbol{X}_i\}_{i=1}^{N}$ are generated by drawing samples from these distributions. For each realization, the model output $Y_i = \mathcal{F}(\boldsymbol{X}_i)$ is evaluated.

The ensemble of model outputs obtained from these random draws is used to approximate the statistical behaviour of $Y$. In particular, moments such as the expected value and variance can be estimated as

$$\mathbb{E}[Y] \approx \frac{1}{N}\sum_{i=1}^{N} Y_i, \qquad \mathrm{Var}(Y) \approx \frac{1}{N-1}\sum_{i=1}^{N} \left(Y_i - \mathbb{E}[Y]\right)^2. \tag{3.20}$$

As the number of realizations increases, these estimates converge to their true values under very mild assumptions on the underlying probability distributions. As a result, MC simulation provides a general and robust framework for exploring the statistical properties of complex models driven by random inputs.

### 3.3.1 Kernel Density Estimation

When making use MC simulations one receives as a result an ensemble of discrete data points, from which one can easily make a histogram to get a rough estimate on the probability density. However, should one want a continuous probability density one can make use of kernel smoothing. Let $\{Y_i\}_{i=1}^N = \mathcal{F}(\boldsymbol{X}_i)$ be independent and identically distributed samples drawn from some distribution with density $f$. The Kernel Density Estimator (KDE) is

$$\hat{f}_h(x) = \frac{1}{N}\sum_{i=1}^{N} K_h(x - Y_i) = \frac{1}{nh}\sum_{i=1}^{N} K\left(\frac{x - Y_i}{h}\right), \tag{3.21}$$

where $K$ is a kernel of choice, and $h > 0$ is the bandwidth, a parameter for determining how smooth the estimate becomes [22]. A multitude of different kernel functions may be used, but a common and convenient choice is the normal kernel, which is defined as

$$\hat{f}_h(x) = \frac{1}{nh\sigma}\frac{1}{\sqrt{2\pi}}\sum_{i=1}^{N} \exp\left(-\frac{(x - Y_i)^2}{2h^2\sigma^2}\right), \tag{3.22}$$

where $\sigma$ is the standard deviation of the samples $\{Y_i\}_{i=1}^N$. The bandwidth can be any chosen scalar, with lower bandwidths being preferable for its increased resolution, but it has higher requirements for the amount of data needed to produce an accurate estimate. As such, rules of thumb have been taken forth, one of which is Scott's Rule which defines $h = N^{-\frac{1}{d+4}}$, where d is the number of dimensions to the data[23].

### 3.3.2 Highest Density Intervals and Confidence Intervals

When characterizing uncertainty in estimated probability densities, interval estimates are commonly used to summarize the range within which a parameter or random variable is likely to lie. Two widely used interval measures are Confidence Intervals (CIs) and Highest Density Intervals (HDIs). Although similar in appearance, they differ fundamentally in interpretation and construction.

A $(1-\alpha)$ confidence interval is a frequentist construct defined such that, under repeated sampling, the true parameter value lies within the interval a fraction $(1-\alpha)$ of the time. Formally, for an estimator $\hat{\theta}$ of a parameter $\theta$, a confidence interval $[L, U]$ satisfies

$$\mathbb{P}\big(L \leq \theta \leq U\big) = 1 - \alpha, \tag{3.23}$$

where the probability is taken over repeated realizations of the data, not over the parameter itself [24]. Confidence intervals therefore describe the reliability of the estimation procedure rather than the probability of the parameter lying within a specific realized interval.

In Bayesian inference, uncertainty is quantified directly through the posterior distribution. An HDI is defined as the region containing a specified probability mass $(1 - \alpha)$ with the requirement for every point inside the interval to have higher posterior density than any point outside. For a posterior density $p(\theta \mid \mathcal{D})$, the HDI $[a, b]$ satisfies

$$\int_a^b p(\theta \mid \mathcal{D})\, d\theta = 1 - \alpha, \tag{3.24}$$

with the additional constraint that

$$p(\theta_1 \mid \mathcal{D}) \geq p(\theta_2 \mid \mathcal{D}), \tag{3.25}$$

for all $\theta_1 \in [a, b]$ and $\theta_2 \notin [a, b]$. A normal measure of distribution precision is the HDI half-width, which is simply calculated as $\frac{a-b}{2}$.

The distinction between the two interval types is particularly relevant for non-Gaussian or skewed distributions. Confidence intervals describe long-run sampling properties, whereas HDIs provide a direct probability statement about the parameter given the observed data. HDIs depend on the posterior distribution and therefore incorporate prior information, while confidence intervals are prior-independent. For symmetric unimodal distributions, the two interval types often coincide; however, for skewed or multimodal distributions, HDIs better capture regions of highest probability density. Additionally, HDIs are not constrained to be centred and will shift toward high-density regions, whereas many confidence intervals are constructed symmetrically about an estimator.

In the context of MC-based uncertainty propagation and Bayesian temperature inference, HDIs provide a more informative summary of posterior uncertainty, particularly when the resulting densities deviate from normal distributions.

## 3.4 Sobol Indices

Consider a deterministic model

$$Y = f(X_1, X_2, \ldots, X_d), \tag{3.26}$$

where the inputs $X_1, \ldots, X_d$ are mutually independent random variables, and $Y$ has finite variance.

### 3.4.1 Variance Decomposition

The model output variance can be uniquely decomposed into contributions from individual variables and their interactions. For any non-empty index set $u \subseteq \{1, \ldots, d\}$, define the partial variance

$$V_u = \mathrm{Var}(\mathbb{E}[\, Y \mid X_u \,]) - \sum_{v \subsetneq u} V_v. \tag{3.27}$$

The total variance satisfies

$$\mathrm{Var}(Y) = \sum_{u \subseteq \{1,\ldots,d\}} V_u. \tag{3.28}$$

### 3.4.2 First-Order Sobol Indices

The first-order Sobol index of input $X_i$ is the fraction of output variance attributable solely to variations in $X_i$ [25]:

$$S_i = \frac{V_i}{\mathrm{Var}(Y)} = \frac{\mathrm{Var}(\mathbb{E}[Y \mid X_i])}{\mathrm{Var}(Y)}. \tag{3.29}$$

### 3.4.3 Higher-Order Sobol Indices

For any subset $u = \{i_1, \ldots, i_k\}$ of inputs, the $k$-th order Sobol index is

$$S_u = \frac{V_u}{\mathrm{Var}(Y)}. \tag{3.30}$$

These indices quantify interaction effects, e.g., the second-order interaction between $X_i$ and $X_j$ is

$$S_{ij} = \frac{\mathrm{Var}(\mathbb{E}[Y \mid X_i, X_j])}{\mathrm{Var}(Y)} - S_i - S_j. \tag{3.31}$$

### 3.4.4 Total-Effect Sobol Indices

The total-effect index of input $X_i$ measures the contribution of $X_i$ including all interactions of any order. It is defined as

$$T_i = 1 - \frac{\mathrm{Var}(\mathbb{E}[Y \mid X_{\sim i}])}{\mathrm{Var}(Y)}, \tag{3.32}$$

where $X_{\sim i}$ denotes all variables except $X_i$.

Equivalently, it is the sum of all Sobol indices for subsets that contain $i$:

$$T_i = \sum_{u:\, i \in u} S_u. \tag{3.33}$$

### 3.4.5 Properties

Sobol indices satisfy

$$0 \leq S_u \leq 1, \qquad 0 \leq T_i \leq 1, \tag{3.34}$$

and the completeness relation

$$\sum_{\emptyset \neq u \subseteq \{1,\ldots,d\}} S_u = 1. \tag{3.35}$$

For additive models $f(X_1, \ldots, X_d) = \sum_i g_i(X_i)$,

$$T_i = S_i, \tag{3.36}$$

as no interaction terms exist.

### 3.4.6 Numerical Calculation of Sobol Indices

Let

$$\boldsymbol{X} = \{r_x^{(s)}, r_x^{(r)}, \theta_x^{(s)}, \theta_x^{(r)}\}_{x \in \mathcal{X}}$$

denote the vector of independent uncertain inputs, with total dimension $M = 4|\mathcal{X}|$, and let the model output be $Y = f(\boldsymbol{X})$.

The Sobol decomposition expresses the variance as

$$\mathrm{Var}(Y) = \sum_{i=1}^{M} V_i + \sum_{i<j} V_{ij} + \cdots + V_{1\ldots M}, \tag{3.37}$$

where $V_i$ is the variance contribution of $X_i$ alone and $V_{ij}$ represents pairwise interaction effects.

The corresponding Sobol indices are defined as

$$S_i = \frac{V_i}{\mathrm{Var}(Y)}, \qquad S_{ij} = \frac{V_{ij}}{\mathrm{Var}(Y)}, \tag{3.38}$$

with total-effect index

$$T_i = 1 - \frac{V_{\sim i}}{\mathrm{Var}(Y)}, \tag{3.39}$$

where $V_{\sim i}$ is the variance of all terms not involving $X_i$ [25].

Using Saltelli sampling, two independent sample matrices

$$\mathbf{A}, \mathbf{B} \in \mathbb{R}^{N \times M}$$

are generated. For each variable $X_i$, a hybrid matrix $\mathbf{A}_\mathbf{B}^{(i)}$ is defined as

$$\left(\mathbf{A}_{\mathbf{B}}^{(i)}\right)_{k,j} = \begin{cases} B_{k,j}, & j = i, \\ A_{k,j}, & j \neq i, \end{cases} \tag{3.40}$$

Evaluating the model for all samples yields $\mathbf{Y_A}$, $\mathbf{Y_B}$, and $\mathbf{Y}_{\mathbf{A}_{\mathbf{B}}^{(i)}}$, from which first-order indices are estimated as

$$S_i \approx \frac{\frac{1}{N}\sum_{k=1}^{N} Y_{\mathbf{B}}^{(k)} \left( Y_{\mathbf{A}_{\mathbf{B}}^{(i)}}^{(k)} - Y_{\mathbf{A}}^{(k)} \right)}{\mathrm{Var}(\mathbf{Y})}, \tag{3.41}$$

and total-effect indices as

$$T_i \approx 1 - \frac{\frac{1}{N}\sum_{k=1}^{N} Y_{\mathbf{A}}^{(k)} \left( Y_{\mathbf{A}_{\mathbf{B}}^{(i)}}^{(k)} - Y_{\mathbf{B}}^{(k)} \right)}{\mathrm{Var}(\mathbf{Y})}. \tag{3.42}$$

Higher-order interaction indices are obtained through analogous mixed sample constructions.

## 3.5 Bayesian Inference

Bayesian inference is a statistical framework in which uncertainty about unknown quantities is represented using probability distributions. In this framework, parameters are treated as random variables rather than fixed but unknown constants, allowing uncertainty to be explicitly quantified and updated as new information becomes available.

Let $\boldsymbol{\theta}$ denote a vector of unknown parameters and let $\mathcal{D}$ represent the set of observed data. Bayesian inference is based on Bayes' theorem [26],

$$p(\boldsymbol{\theta} \mid \mathcal{D}) = \frac{p(\mathcal{D} \mid \boldsymbol{\theta})\, p(\boldsymbol{\theta})}{p(\mathcal{D})}, \tag{3.43}$$

where $p(\boldsymbol{\theta})$ is the prior distribution encoding beliefs about the parameters before observing the data, $p(\mathcal{D} \mid \boldsymbol{\theta})$ is the likelihood function describing the data-generating process, and $p(\boldsymbol{\theta} \mid \mathcal{D})$ is the posterior distribution representing updated beliefs after conditioning on the data. The denominator

$$p(\mathcal{D}) = \int p(\mathcal{D} \mid \boldsymbol{\theta})\, p(\boldsymbol{\theta})\, d\boldsymbol{\theta} \tag{3.44}$$

is known as the marginal likelihood or evidence and serves as a normalization constant.

### 3.5.1 Prior Distributions

The prior distribution expresses all available knowledge or assumptions about the parameters before data are observed. Priors may be informative, reflecting strong domain

knowledge, or weakly informative and non-informative, providing regularization while allowing the data to dominate the inference. The choice of prior can play a critical role in Bayesian analysis, especially in settings where data is limited or noisy [27].

### 3.5.2 Likelihood Function and Log-Likelihood

The likelihood function quantifies the probability of observing the data given specific values of the model parameters. It is determined by assumptions about the stochastic process underlying the observations, including noise characteristics and independence structure. The likelihood function serves as the mechanism through which information from the observed data is used for the inference.

Let $\boldsymbol{\theta}$ denote a vector of unknown parameters and let $\mathcal{D} = \{x_1, x_2, \ldots, x_n\}$ represent the set of observed data. Assuming that the observations are independent, the likelihood function is defined as

$$L(\boldsymbol{\theta} \mid \mathcal{D}) = \prod_{i=1}^{n} p(x_i \mid \boldsymbol{\theta}), \tag{3.45}$$

where $p(x_i \mid \boldsymbol{\theta})$ is the probability density or mass function for a single observation $x_i$.

In many applications, it is convenient to consider the log-likelihood function, obtained by taking the natural logarithm of the likelihood:

$$\ell(\boldsymbol{\theta} \mid \mathcal{D}) = \log L(\boldsymbol{\theta} \mid \mathcal{D}) = \sum_{i=1}^{n} \log p(x_i \mid \boldsymbol{\theta}). \tag{3.46}$$

The logarithmic transformation converts the product of probabilities into a sum, which simplifies both analytical derivations. Log-likelihoods are widely employed in parameter estimation, as they preserve the location of maxima of the likelihood function while improving numerical stability.

### 3.5.3 Posterior Distribution

The posterior distribution combines prior information and data through Bayes' theorem and represents the complete probabilistic description of the unknown parameters after observation. Most statistical inferences, such as point estimates, credible intervals, and predictive distributions, are derived from the posterior [28]. Common summaries include the posterior mean, median, mode, and HDI.

### 3.5.4 Soft Physical Constraints in Bayesian Inference

In many physical inference problems, model parameters are governed by known feasibility ranges derived from engineering practice, safety considerations, or empirical observations. In a Bayesian framework, such knowledge can be incorporated either as hard constraints

or as soft constraints. Hard constraints strictly prohibit parameter values outside a predefined domain, whereas soft constraints assign decreasing probability to implausible regions without excluding them entirely.

Soft physical constraints are particularly advantageous when the underlying physical limits are uncertain, approximate, or context-dependent. Rather than truncating the parameter space, soft constraints modify the posterior distribution by introducing a continuous penalty that discourages violations while preserving probabilistic continuity and differentiability.

Formally, let $p(\boldsymbol{\theta} \mid \mathcal{D})$ denote the unconstrained posterior distribution. A soft constraint is incorporated by defining an augmented posterior

$$p^*(\boldsymbol{\theta} \mid \mathcal{D}) \propto p(\boldsymbol{\theta} \mid \mathcal{D}) \exp\big(\Psi(\boldsymbol{\theta})\big), \tag{3.47}$$

where $\Psi(\boldsymbol{\theta}) \leq 0$ is a penalty function that encodes prior physical knowledge. Within the admissible region, $\Psi(\boldsymbol{\theta}) = 0$, while outside this region the function smoothly decreases, reducing posterior probability mass.

This formulation can be interpreted as introducing an additional prior term or as a relaxation of a hard constraint into a probabilistic preference. Importantly, soft constraints preserve the differentiability of the log-posterior, which is essential for gradient-based samplers such as Hamiltonian Monte Carlo (HMC).

In physical systems characterized by noisy measurements and imperfect models, soft constraints provide a principled mechanism for balancing data-driven inference against physical plausibility, avoiding overconfidence and boundary-induced sampling artifacts.

### 3.5.5 Hamiltonian Monte Carlo and the No-U-Turn Sampler

In Bayesian inference, the aim is to characterise the posterior distribution $p(\boldsymbol{\theta} \mid \mathcal{D})$ of unknown parameters $\boldsymbol{\theta}$ given observed data $\mathcal{D}$. For most realistic models, this distribution cannot be evaluated or normalised analytically. Instead, inference is performed by sampling from the posterior. Sampling means generating a collection of parameter values whose empirical distribution approximates the true posterior. Posterior expectations, credible intervals, and correlations are then estimated directly from these samples.

Monte Carlo MC methods generate such samples by constructing a sequence of parameter vectors that forms a Markov chain with the posterior as its stationary distribution. Each new sample is proposed from the current one and is either accepted or rejected in a way that ensures that, over time, the chain visits parameter values with frequencies proportional to their posterior probability.

HMC improves the efficiency of this process by proposing new samples through structured, directed moves rather than random local perturbations. Starting from a current parameter vector $\boldsymbol{\theta}$, HMC introduces an auxiliary momentum variable $\mathbf{p}$ and uses gra-

dient information of the log-posterior to propose a new candidate state. This allows the sampler to move efficiently across regions of high posterior probability while respecting the geometry of the distribution, which is particularly important in high-dimensional or strongly correlated parameter spaces [29].

Because the proposed move is constructed using approximate dynamics, the resulting candidate sample does not necessarily have exactly the same posterior probability as the current one. To ensure that the sampling procedure still targets the correct posterior distribution, HMC employs a Metropolis acceptance step. In this step, the proposed parameter vector's posterior probability is compared to that of the current one. If the proposed state has higher posterior probability, it is always accepted. If it has lower posterior probability, it is accepted with a probability that decreases with the loss in posterior density. This acceptance rule allows occasional moves to lower-probability regions while still favouring samples from regions of high posterior mass.

If the proposal is accepted, the candidate parameter vector becomes the next sample in the Markov chain; if it is rejected, the sampler remains at the current parameter value. Repeating this procedure produces a collection of samples that approximate the posterior distribution.

An important practical consequence of HMC is that posterior inference applies not only to parameters that are directly observed. Any latent variables in the model, as well as any differentiable deterministic quantities derived from the parameters, can be evaluated at each accepted sample. This yields posterior distributions for these quantities and naturally propagates uncertainty through the model [30].

The efficiency of HMC depends on algorithmic parameters such as the step size and the length of the proposed trajectory. Choosing these parameters manually can be challenging and model dependent. The No-U-Turn Sampler (NUTS) is an adaptive extension of HMC that automatically determines an appropriate trajectory length by detecting when further movement would begin to retrace already explored regions of parameter space [31].

During an initial warm-up phase, NUTS also adapts the step size to better match the geometry of the posterior distribution. This makes NUTS robust and well suited for complex Bayesian models with correlated parameters and non-linear structure.

For reliable posterior estimation using HMC and NUTS, the geometry of the posterior distribution is critical. Smooth posterior contours and gradual curvature enable efficient exploration and well-mixed samples. In contrast, sharp edges, discontinuities, or irregular posterior geometries can degrade sampling performance and lead to biased or unreliable uncertainty estimates.

## 3.6 Kalman Filtering

Kalman filtering is a Bayesian estimation technique for linear dynamical systems with normally distributed and additive noise. It provides an optimal estimate of the system state by combining a model-based prediction with noisy measurements.

A discrete-time linear system is described by

$$\mathbf{x}_k = \mathbf{F}\mathbf{x}_{k-1} + \mathbf{w}_k, \tag{3.48a}$$

$$\mathbf{z}_k = \mathbf{H}\mathbf{x}_k + \mathbf{v}_k, \tag{3.48b}$$

where $\mathbf{x}_k$ is the state vector, $\mathbf{z}_k$ is the measurement vector, $\mathbf{F}$ is the state transition matrix, and $\mathbf{H}$ is the measurement matrix. The process noise $\mathbf{w}_k \sim \mathcal{N}(\mathbf{0}, \mathbf{Q})$ models uncertainties in the systems evolution, while $\mathbf{v}_k \sim \mathcal{N}(\mathbf{0}, \mathbf{R})$ represents measurement inaccuracies.

The Kalman filter operates in two steps to estimate the state; first predicting the next state estimate and its covariance forward in time and then updating the prediction based on the real measurement. The correction is weighted by the Kalman gain $\mathbf{K}_G$, which aims to balance trust between the model and the measurements.

While optimal for linear systems, the classical Kalman filter performs poorly when applied to non-linear systems, as linearization errors can significantly affect estimation accuracy.

### 3.6.1 Unscented Kalman Filtering Theory

The Unscented Kalman Filter (UKF) extends the Kalman filter to non-linear systems without requiring explicit linearization. Instead of approximating non-linear functions via Jacobians, the UKF uses the unscented transform; a set of sigma points is generated around the current state estimate and propagated through the non-linear system equations.

For a non-linear system

$$\mathbf{x}_k = f(\mathbf{x}_{k-1}) + \mathbf{w}_k, \tag{3.49a}$$

$$\mathbf{z}_k = h(\mathbf{x}_k) + \mathbf{v}_k, \tag{3.49b}$$

the UKF approximates the mean and covariance of the transformed variables by propagating the sigma points through $f(\cdot)$ and $h(\cdot)$.

At time step $k-1$, the state distribution is represented by a set of $2n+1$ sigma points, where $n$ is the state dimension. Given the prior state estimate $\hat{\mathbf{x}}_{k-1}$ and covariance $\mathbf{P}_{k-1}$,

the sigma points are defined as

$$\boldsymbol{\chi}_{k-1}^{(0)} = \hat{\mathbf{x}}_{k-1}, \tag{3.50a}$$

$$\boldsymbol{\chi}_{k-1}^{(i)} = \hat{\mathbf{x}}_{k-1} + \left(\sqrt{(n+\lambda)\mathbf{P}_{k-1}}\right)_i, \quad i = 1, \ldots, n, \tag{3.50b}$$

$$\boldsymbol{\chi}_{k-1}^{(i)} = \hat{\mathbf{x}}_{k-1} - \left(\sqrt{(n+\lambda)\mathbf{P}_{k-1}}\right)_{i-n}, \quad i = n+1, \ldots, 2n, \tag{3.50c}$$

where $\lambda = \alpha^2(n+\kappa) - n$ is a scaling parameter and the matrix square root is typically obtained via the Cholesky decomposition, for more information read *Cholesky's Decomposition - an Overview | ScienceDirect Topics* [32]. The associated weights for computing the mean and covariance are

$$W_m^{(0)} = \frac{\lambda}{n+\lambda}, \tag{3.51a}$$

$$W_c^{(0)} = \frac{\lambda}{n+\lambda} + (1 - \alpha^2 + \beta), \tag{3.51b}$$

$$W_m^{(i)} = W_c^{(i)} = \frac{1}{2(n+\lambda)}, \quad i = 1, \ldots, 2n, \tag{3.51c}$$

where the parameters $\alpha$, $\beta$, and $\kappa$ determine the spread and higher-order moment matching of the sigma points.

In the time-update (prediction) step, each sigma point is individually propagated through the state transition function,

$$\boldsymbol{\chi}_{k|k-1}^{(i)} = f\left(\boldsymbol{\chi}_{k-1}^{(i)}\right), \quad i = 0, \ldots, 2n. \tag{3.52}$$

The predicted state mean and covariance are then obtained as

$$\hat{\mathbf{x}}_{k|k-1} = \sum_{i=0}^{2n} W_m^{(i)} \boldsymbol{\chi}_{k|k-1}^{(i)}, \tag{3.53a}$$

$$\mathbf{P}_{k|k-1} = \sum_{i=0}^{2n} W_c^{(i)} \left(\boldsymbol{\chi}_{k|k-1}^{(i)} - \hat{\mathbf{x}}_{k|k-1}\right)\left(\boldsymbol{\chi}_{k|k-1}^{(i)} - \hat{\mathbf{x}}_{k|k-1}\right)^\top + \mathbf{Q}_k, \tag{3.53b}$$

where $\mathbf{Q}_k$ denotes the process noise covariance.

To incorporate measurements, the predicted sigma points must be transformed and enter the measurement space,

$$\boldsymbol{\gamma}_k^{(i)} = h\left(\boldsymbol{\chi}_{k|k-1}^{(i)}\right), \quad i = 0, \ldots, 2n. \tag{3.54}$$

Then, the predicted measurement mean and covariance are computed as

$$\hat{\mathbf{z}}_k = \sum_{i=0}^{2n} W_m^{(i)} \boldsymbol{\gamma}_k^{(i)}, \tag{3.55a}$$

$$\mathbf{S}_k = \sum_{i=0}^{2n} W_c^{(i)} \left(\boldsymbol{\gamma}_k^{(i)} - \hat{\mathbf{z}}_k\right) \left(\boldsymbol{\gamma}_k^{(i)} - \hat{\mathbf{z}}_k\right)^\top + \mathbf{R}_k, \tag{3.55b}$$

where $\mathbf{R}_k$ is the measurement noise covariance. The cross-covariance between the state and measurement is given by

$$\mathbf{P}_{xz,k} = \sum_{i=0}^{2n} W_c^{(i)} \left(\boldsymbol{\chi}_{k|k-1}^{(i)} - \hat{\mathbf{x}}_{k|k-1}\right) \left(\boldsymbol{\gamma}_k^{(i)} - \hat{\mathbf{z}}_k\right)^\top. \tag{3.56}$$

The Kalman gain is then computed as

$$\mathbf{K}_G = \mathbf{P}_{xz,k} \mathbf{S}_k^{-1}. \tag{3.57}$$

Using the measurement $\mathbf{z}_k$, the state estimate and covariance are updated according to

$$\hat{\mathbf{x}}_k = \hat{\mathbf{x}}_{k|k-1} + \mathbf{K}_G \left(\mathbf{z}_k - \hat{\mathbf{z}}_k\right), \tag{3.58a}$$

$$\mathbf{P}_k = \mathbf{P}_{k|k-1} - \mathbf{K}_k \mathbf{S}_k \mathbf{K}_k^\top. \tag{3.58b}$$

An important measure of how well a measurement was predicted is the measurement innovation, which is defined as

$$\boldsymbol{\nu}_k = \mathbf{z}_k - \hat{\mathbf{z}}_k, \tag{3.59}$$

with associated innovation covariance $\mathbf{S}_k$ as given in (3.55). A normalized innovation magnitude is then computed as

$$\eta_k = \boldsymbol{\nu}_k^\top \mathbf{S}_k^{-1} \boldsymbol{\nu}_k. \tag{3.60}$$

The innovation vector is normally distributed under the assumption of zero-mean Gaussian measurement noise and a correctly specified measurement model. Consequently, the normalized innovation magnitude $\eta_k = \boldsymbol{\nu}_k^\top \mathbf{S}_k^{-1} \boldsymbol{\nu}_k$ corresponds to the sum of squared, normalized Gaussian random variables. By definition, this quantity follows a chi-square distribution with degrees of freedom equal to the measurement dimension

# 4 Method

This work follows a structured, four-stage methodology to assess and improve the estimation of temperature from phasor measurements. In the first stage, uncertainty propagation is employed to quantify how model assumptions and uncertainties in phasor measurements affect the temperature estimate. A forward model relating the measured phasors to temperature is defined, and uncertainties in the input quantities are propagated through this model using analytical linearization and MC sampling. This yields a probabilistic characterization of the temperature estimate and establishes a baseline understanding of the impact of the error sources.

In the second stage, a global sensitivity analysis is performed using Sobol indices to identify the dominant contributors to the variance of the temperature estimate. By decomposing the total output variance into first-order effects and higher-order interaction terms, this analysis reveals which measurement parameters, model inputs, or calibration factors most strongly influence the inferred temperature. These results are used to prioritize sources of uncertainty and guide improvements in measurement design and modelling assumptions.

In the third stage, Bayesian inference is applied to evaluate the reliability of the full measurement chain under static conditions. Prior knowledge is incorporated through engineering constraints and physics-informed models governing the relationship between temperature and phasor behaviour. Artificial observations will be generated using different accuracy classes to sample noise according to their respective accuracy and precision levels. Both single-measurement and multiple-measurement scenarios are considered, enabling the assessment of information gain from repeated observations. The resulting posterior distributions provide a quantitative measure of confidence in the temperature estimates and allow systematic comparison of reliability across different simulated measurement accuracy classes.

In the final stage, the methodology is extended to the dynamic case, where both nominal conductor temperature and nominal phasors may vary over time. Temporal models are introduced to capture the thermal dynamics of the conductor and the time evolution of the electrical phasors under changing operating conditions. State-space formulations are explored, enabling the use of sequential Bayesian estimation techniques such as UKF. This stage focuses on assessing observability, tracking performance, and uncertainty evolution in time, thereby laying the groundwork for real-time or near-real-time dynamic temperature estimation based on streaming phasor measurements.

## 4.1 Propagation of Uncertainties

### 4.1.1 Physical Uncertainties

The main uncertainty caused by the physical model that will be evaluated in this thesis is the linear approximation of resistance, as per Section 2.2.3.The approximation is done using a Taylor expansion, and thus the error caused can be simply evaluated. Using Equations (2.6) and (2.10) in tandem yields

$$P_\ell = k_j I_{AC}^2 \left(R_{AC} l \left(1 + \alpha \left(T_{\text{AV}} - T_{\text{ref}}\right) + \mathcal{O}\left(\alpha^2 \left(T_{AV} - T_{\text{ref}}\right)^2\right)\right)\right), \tag{4.1a}$$

$$\Rightarrow T_{\text{AV}} = T_{\text{ref}} + \frac{1}{\alpha}\left(\frac{P_\ell}{k_j I_{AC}^2 R_{AC} l} - 1\right) + \mathcal{O}\left(R_{\text{AC}} l \alpha \left(T_{\text{AV}} - T_{\text{ref}}\right)^2\right), \tag{4.1b}$$

$$= T_{\text{ref}} + \frac{1}{\alpha}\left(\frac{P_\ell}{k_j I_{AC}^2 R_{AC} l} - 1\right) + T_{\text{ERR}} \tag{4.1c}$$

To ensure that the error caused by model assumptions' order of magnitude is smaller than some $T_{\text{ERR}}$, the required difference between operational and reference temperature can be calculated as the solutions to $R_{\text{AC}} l \alpha (T_{\text{OM}} - T_{\text{ref}})^2 = T_{\text{ERR}}$

### 4.1.2 Measurement Uncertainties

To quantify the impact of measurement uncertainties on the estimated temperature, we follow a systematic error-propagation procedure based on the underlying measurement model.

**1. Measurement Model** The measured real power on the sending or receiving side is modelled as a product of the measured real voltages and currents, each perturbed by small ratio errors $r_x$, and modified by the small phase errors $\theta_x$:

$$\Re\left(\widetilde{V}^{(\cdot)}_{\text{MEAS}}\right) = \nu^{(\cdot)} \prod_{x \in X_V} \left(1 + r_x^{(\cdot)}\right) \cos\left(\theta_\nu^{(\cdot)} + \sum_{x \in X_V} \theta_x^{(\cdot)}\right) \tag{4.2a}$$

$$\Re\left(\widetilde{I}^{(\cdot)}_{\text{MEAS}}\right) = \iota^{(\cdot)} \prod_{x \in X_C} \left(1 + r_x^{(\cdot)}\right) \cos\left(\theta_\iota^{(\cdot)} + \sum_{x \in X_C} \theta_x^{(\cdot)}\right) \tag{4.2b}$$

where $(\cdot) \in \{(r), (s)\}$, and $\mathcal{X}_\mathcal{V} = \{VU, VS_U, VS_O, VT\}$ and $\mathcal{X}_\mathcal{C} = \{CU, CS_U, CT\}$ denote the set of all voltage and current uncertainties, respectively. This yields,

$$P^{(\cdot)}_{\text{MEAS}} = \Re\left(\widetilde{V}^{(\cdot)}_{\text{MEAS}} \widetilde{I^*}^{(\cdot)}_{\text{MEAS}}\right) = s^{(\cdot)} \prod_{x \in \mathcal{X}} (1 + r_x^{(\cdot)}) \cos\left(\phi^{(\cdot)} + \sum_{x \in \mathcal{X}_V} \theta_x^{(\cdot)} - \sum_{x \in \mathcal{X}_C} \theta_x^{(\cdot)}\right), \tag{4.3}$$

where $\mathcal{X} = \mathcal{X}_V \cup \mathcal{X}_C$.

**2. Expansion of Ratio Errors** The multiplicative product of ratio errors is expanded using a binomial-type series. We consider both:

- First-order truncation, retaining only the sum of individual ratio errors.
- Second-order truncation, including all pairwise products of ratio errors.

This allows for systematic approximation of the effect of measurement errors to the desired order of accuracy. The product of ratio errors can be exactly expanded as

$$\prod_{x\in\mathcal{X}}(1+r_x^{(\cdot)}) = 1+\sum_{x\in\mathcal{X}} r_x^{(\cdot)} + \sum_{x<y} r_x^{(\cdot)} r_y^{(\cdot)} + \sum_{x<y<z} r_x^{(\cdot)} r_y^{(\cdot)} r_z^{(\cdot)} + \cdots + \prod_{x\in\mathcal{X}} r_x^{(\cdot)}. \tag{4.4}$$

For small ratio errors $|r_x^{(\cdot)}| \ll 1$, we can truncate:

**First-order truncation:**

$$\prod_{x\in\mathcal{X}}(1+r_x^{(\cdot)}) \approx 1+\sum_{x\in\mathcal{X}} r_x^{(\cdot)} \equiv 1 + r_{(1\text{st})}^{(\cdot)}. \tag{4.5}$$

**Second-order truncation:**

$$\prod_{x\in\mathcal{X}}(1+r_x^{(\cdot)}) \approx 1+\sum_{x\in\mathcal{X}} r_x^{(\cdot)} + \sum_{x<y} r_x^{(\cdot)} r_y^{(\cdot)} \equiv 1 + r_{(2\text{nd})}^{(\cdot)}. \tag{4.6}$$

**3. Expected Measured Power** Assuming that ratio and phase errors are independent random variables with known means and variances, the expectation of the measured power is computed. Second-order terms are retained to capture contributions from both non-zero means and variances of the errors.

**4. Absolute Biases** The absolute bias of a measurable quantity $X$ is defined as the difference between its expected measured value and the nominal value:

$$\Delta X = \mathbb{E}[X_{\text{MEAS}}] - X_{\text{NOM}}. \tag{4.7}$$

The power loss bias is obtained as the difference between sending and receiving side biases, and the absolute bias of the temperature estimate is computed by propagating the power-loss bias through the known linear relationship between temperature and power loss.

**5. Variance Propagation** To quantify the uncertainty of the measurements, the variance of each quantity is computed using linearization for small phase deviations. The variance of the measured power is propagated to the power loss and, subsequently, to the temperature estimate using standard linear-error propagation formulas.

**6. Relative Biases** Relative biases are defined as the ratio of the expected value to the true value minus one:

$$\delta X = \frac{\mathbb{E}[X_{\text{MEAS}}]}{X} - 1, \tag{4.8}$$

where $X$ can be the power loss or the estimated temperature. This quantifies the systematic scaling effect of measurement uncertainties in a relative sense, complementary to the absolute bias.

This method provides a systematic framework for propagating both random and systematic measurement errors through the non-linear measurement model to the estimated temperature.

### 4.1.3 Numerical Modelling of Measurement Uncertainty

A vectorized MC framework was developed to quantify the propagation of measurement uncertainties through power system quantities and their impact on conductor temperature distributions. The approach considers multiple independent voltage and current measurements and models both amplitude and phase errors. From defined nominal phasors at the receiving-end of the transmission line and a chosen nominal temperature $T_{\text{NOM}}$, the $\pi$-model is used to calculate nominal sent-end phasors and temperature-dependent conductor parameters are calculated. After computing nominal phasors, measurement errors are modelled as random perturbations on amplitude and phase, see Equation (4.2). The modelled errors are chosen as per Tables 2.2, 2.3, and 2.4. The MC simulation generates $n_{\text{samp}}$ realizations of the perturbed measurements for both sending and receiving ends, from which RMS-power samples are computed as per Equation (4.3).

Conductor temperature is estimated from power loss and effective AC current using the linearized model from Equation (2.11). Vectorized computation allows evaluation of temperature distributions over all MC realizations, providing statistical estimates such as mean, variance, as well as absolute and relative biases. Lastly, the produced measurements are used to create KDEs using a Gaussian kernel and choosing the bandwidth using Scott's Rule.

The method is implemented in Python using the PyTensor and SciPy packages. This approach enables robust statistical characterization of the propagated uncertainty in voltage, current, power, and temperature, providing a rigorous framework for calculating uncertainty propagation.

### 4.1.4 Set-Up for Numerical Modelling and Comparisons

The computations are done with conductor parameters defined for model Bohus, nominal temperature $T_{\text{NOM}} = 50°\text{C}$, and nominal receiving end phasors defined as

$$\widetilde{V}^{(r)} = 140000/\sqrt{3}\angle\phi^{(r)}, \qquad \widetilde{I}^{(r)} = I^{\text{C}}_{\text{RATE}}\angle 0, \qquad \phi^{(r)} = \arccos(0.8) \approx 0.644. \tag{4.9}$$

From this the nominal sent phasors are calculated using the $\pi$-model to be

$$\widetilde{V}^{(s)} \approx 85006\angle 0.686, \qquad \widetilde{I}^{(s)} \approx 810.5\angle 0.004, \qquad \phi^{(s)} \approx 0.682. \tag{4.10}$$

The Errors applied to the samples were drawn from th intervals in Tables 2.2, 2.3, and 2.4 according to chosen accuracy class and applied to each quantity.

For high accuracy classes, the transformer inaccuracies become significantly smaller than secondary circuit uncertainties. This causes the errors to still be on the order of magnitude of the secondary circuit uncertainties, making the change of accuracy class close to irrelevant. Thus, to counteract this, it will be assumed that the error margins of these may also be decreased to the same extent as those for transformers. Thus, secondary circuit uncertainty boundaries will be at most as defined in Tables 2.2 and 2.3, and if the transformer errors are smaller than these, then the secondary circuit uncertainty will be equivalent to the transformer errors. Lastly, for both conductor models a sweep over current amplitudes will be made to compare temperature variances.

## 4.2 Sobol Indices

### 4.2.1 Model Formulation

The average temperature in Equation (2.11) is almost entirely linear in the measured power difference, so Sobol indices for $T_{\mathrm{AV}}$ are close to identical to those of $P_{\ell,\mathrm{MEAS}}$. Receiving and sending-end measurements depend on distinct sets of uncertain variables:

$$P^{(s)}_{\mathrm{MEAS}} = s^{(s)} A^{(s)}\, g^{(s)}(\Theta^{(s)}), \qquad A^{(s)} = \prod_{x\in\mathcal{X}} (1 + r^{(s)}_x), \qquad \Theta^{(s)} = \sum_{x\in\mathcal{X}} \theta^{(s)}_x, \tag{4.11a}$$

$$P^{(r)}_{\mathrm{MEAS}} = s^{(r)} A^{(r)}\, g^{(r)}(\Theta^{(r)}), \qquad A^{(r)} = \prod_{x\in\mathcal{X}} (1 + r^{(r)}_x), \qquad \Theta^{(r)} = \sum_{x\in\mathcal{X}} \theta^{(r)}_x. \tag{4.11b}$$

The cosine terms are

$$g^{(s)}(u) = \cos\big(\phi^{(s)} + u\big), \tag{4.12a}$$

$$g^{(r)}(u) = \cos\big(\phi^{(r)} + u\big). \tag{4.12b}$$

All uncertain quantities

$$\{r^{(s)}_x, r^{(r)}_x, \theta^{(s)}_x, \theta^{(r)}_x\}_{x\in\mathcal{X}}$$

are mutually independent. Means and variances are denoted

$$\mu_{r^{(s)}_x} = \mathbb{E}[r^{(s)}_x], \quad \sigma^2_{r^{(s)}_x} = \mathrm{Var}(r^{(s)}_x), \quad \text{etc.} \tag{4.13}$$

### 4.2.2 Mean-Corrected Expansion

Introduce fluctuations about the mean:

$$\tilde{r}_x^{(s)} = r_x^{(s)} - \mu_{r_x^{(s)}}, \quad \tilde{\theta}_x^{(s)} = \theta_x^{(s)} - \mu_{\theta_x^{(s)}}, \quad \text{etc.} \tag{4.14}$$

Define the mean amplitude products and mean phase sums:

$$\bar{A}^{(s)} = \prod_x (1 + \mu_{r_x^{(s)}}), \quad \bar{A}^{(r)} = \prod_x (1 + \mu_{r_x^{(r)}}), \tag{4.15}$$

$$\bar{\Theta}^{(s)} = \sum_x \mu_{\theta_x^{(s)}}, \quad \bar{\Theta}^{(r)} = \sum_x \mu_{\theta_x^{(r)}}. \tag{4.16}$$

### 4.2.3 Justification for Second-Order Expansion

If the deviations of the uncertain variables from their means are small, i.e.

$$|\tilde{r}_x^{(s)}| \ll 1, \quad |\tilde{r}_x^{(r)}| \ll 1, \quad |\tilde{\theta}_x^{(s)}| \ll 1, \quad |\tilde{\theta}_x^{(r)}| \ll 1, \tag{4.17}$$

then a Taylor expansion of both the multiplicative amplitude products and the trigonometric functions around the mean provides an accurate approximation of the model. Retaining only the first-order terms corresponds to a purely linear model in the fluctuations, capturing the main contributions to the variance from individual variables. Including second-order terms introduces pairwise interaction terms between the fluctuations which account for how variable interactions influence the total variance. Consequently, in this study we will use the second-order expansion to compute Sobol indices, allowing both first-order and second-order contributions to be quantified. This provides insight into how interactions among the uncertain inputs affect the variance of the measured power and, by extension, the average temperature.

### 4.2.4 Second-Order Polynomial Expansion Around the Mean

**Amplitudes:** Expanding multiplicatively around the mean:

$$A^{(\cdot)} \approx \bar{A}^{(\cdot)} \left( 1 + \sum_x \frac{\tilde{r}_x^{(\cdot)}}{1 + \mu_{r_x^{(\cdot)}}} + \sum_{x<y} \frac{\tilde{r}_x^{(\cdot)} \tilde{r}_y^{(\cdot)}}{(1 + \mu_{r_x^{(\cdot)}})(1 + \mu_{r_y^{(\cdot)}})} \right) \tag{4.18}$$

**Cosines:** Expand around the mean phase sums:

$$\cos(\phi^{(\cdot)} + \Theta^{(\cdot)}) \approx C'^{(\cdot)} - S'_s \, \tilde{\Theta}^{(\cdot)} - \frac{1}{2} C'^{(\cdot)} (\tilde{\Theta}^{(\cdot)})^2 \tag{4.19}$$

where

$$C'^{(\cdot)} = \cos(\phi^{(\cdot)} + \bar{\Theta}^{(\cdot)}), \quad S'^{(\cdot)} = \sin(\phi^{(\cdot)} + \bar{\Theta}^{(\cdot)}). \tag{4.20}$$

### 4.2.5 Second-Order Model for Measured Power Loss

Combining the above expansions gives a polynomial in the centered variables $\tilde{r}_x^{(\cdot)}, \tilde{\theta}_x^{(\cdot)}$:

$$P_{\ell|\mathrm{MEAS}} \approx s^{(s)} A^{(s)} g^{(s)}(\Theta^{(s)}) - s^{(r)} A^{(r)} g^{(r)}(\Theta^{(r)}), \tag{4.21}$$

with all $A^{(\cdot)}, g^{(\cdot)}$ replaced by their mean-corrected expansions.

### 4.2.6 Sobol Indices and Total-Effect Indices

Sobol indices are defined in terms of the general theory in Section 3.4:

- First-order: Equation (3.29)
- Higher-order: Equation (3.30)
- Second-order pairwise: Equation (3.31)
- Total-effect: Equations (3.32)–(3.33)

Because the model is polynomial in the centred variables, all conditional variances can be computed in closed form. Each total-effect index is the sum of all first-order and second-order terms involving that variable, as in Equations (3.32)–(3.33). For example:

$$T_{\tilde{r}_x^{(s)}} = S_{\tilde{r}_x^{(s)}} + \sum_{y \neq x} S_{\tilde{r}_x^{(s)}, \tilde{r}_y^{(s)}} + \sum_{y} S_{\tilde{r}_x^{(s)}, \tilde{\theta}_y^{(s)}} + \sum_{y} S_{\tilde{r}_x^{(s)}, \tilde{r}_y^{(r)}} + \sum_{y} S_{\tilde{r}_x^{(s)}, \tilde{\theta}_y^{(r)}}, \tag{4.22a}$$

$$T_{\tilde{\theta}_x^{(s)}} = S_{\tilde{\theta}_x^{(s)}} + \sum_{y \neq x} S_{\tilde{\theta}_x^{(s)}, \tilde{\theta}_y^{(s)}} + \sum_{y} S_{\tilde{\theta}_x^{(s)}, \tilde{r}_y^{(s)}} + \sum_{y} S_{\tilde{\theta}_x^{(s)}, \tilde{r}_y^{(r)}} + \sum_{y} S_{\tilde{\theta}_x^{(s)}, \tilde{\theta}_y^{(r)}}. \tag{4.22b}$$

All variances entering the Sobol indices are computed using the centred random variables $\tilde{r}_x, \tilde{\theta}_x$, ensuring correct contributions for non-zero mean inputs.

### 4.2.7 Numerical Implementation

Sobol indices for the full non-linear temperature model were computed using the SALib Python package, which implements the Saltelli sampling and estimation framework described in (3.37)–(3.42).

Given the uncertain input vector $\boldsymbol{X}$, SALib generates the base sample matrices $\mathbf{A}$ and $\mathbf{B}$ together with the hybrid matrices defined in (3.40). The temperature model is then evaluated for all sample sets, producing the output ensembles required by the estimators in (3.41) and (3.42).

From these evaluations, first-order, total-effect, and second-order Sobol indices are computed, enabling variance decomposition of the complete non-linear formulation without relying on Taylor-series approximations.

## 4.3 Bayesian Inference for Temperature Estimation

The Bayesian modelling in this work is implemented using PyMC, a probabilistic programming library that facilitates the construction and inference of complex probabilistic models. The core idea behind the Bayesian approach is to represent unknown quantities as random variables and update their distributions in light of observed data, using Bayes' theorem, see Equation (3.43).

### 4.3.1 Observed Data and Measurement Generation

The observed data for this method are $n$ sets of artificially generated phasor measurements. The measurements are generated by choosing a single set of nominal values for received phasor quantities

$$\nu_{\text{NOM}}^{(r)} = 140000/\sqrt{3}, \tag{4.23a}$$
$$\iota_{\text{NOM}}^{(r)} = I_{\text{RATE}}^{\text{C}}, \tag{4.23b}$$
$$\theta_{\nu|\text{NOM}}^{(r)} = \arccos(0.8), \tag{4.23c}$$
$$\theta_{\iota|\text{NOM}}^{(r)} = 0, \tag{4.23d}$$
$$T_{\text{NOM}} = 50, \tag{4.23e}$$

which were used to calculate nominal sent phasor values using the $\pi$-model, see Equation (2.4). After definition of nominal phasor values, $n$ sets of measurement errors were sampled for chosen accuracy classes according to Tables 2.2, 2.3, and 2.4, and applied as per equations (4.2). For higher accuracy classes, errors for secondary circuit uncertainty was sampled similarly as in Section 4.1.4. The sampled errors were then applied to phasor values as described in Equation (4.2), to create $N$ sets of noisy measurements.

### 4.3.2 Choice of prior distributions

In this model, the Bayesian framework requires explicit specification of the prior distributions for all latent and free variables. Two sets of priors are implemented, where the first is engineering-informed and based on operational experience to give an initial estimate of current and voltage phasors. The second is physics-informed and uses a combination of the operational experience described and the $\pi$-model allowing uncertainty propagation through this physical relation.

For both sent and received phasors the engineering-informed priors are defined as

$$\nu_{\text{EST}}^{(\cdot)} \sim \mathcal{U}\left[0.9\nu_{\text{NOM}}^{(\cdot)}, 1.1\nu_{\text{NOM}}^{(\cdot)}\right], \qquad \iota_{\text{EST}}^{(\cdot)} \sim \mathcal{U}\left[0.9\iota_{\text{NOM}}^{(\cdot)}, 1.1\iota_{\text{NOM}}^{(\cdot)}\right], \tag{4.24a}$$
$$\theta_{\nu|\text{EST}}^{(\cdot)} \sim \mathcal{U}\left[0.9\theta_{\nu,\text{NOM}}^{(\cdot)}, 1.1\theta_{\nu|\text{NOM}}^{(\cdot)}\right], \qquad \theta_{\iota|\text{EST}}^{(\cdot)} \sim \mathcal{U}\left[0.9\theta_{\iota,\text{NOM}}^{(\cdot)}, 1.1\theta_{\iota|\text{NOM}}^{(\cdot)}\right], \tag{4.24b}$$

where $\mathcal{U}$ is a uniform distribution and $\nu^{(\cdot)}_{\text{EST}}, \iota^{(\cdot)}_{\text{EST}}, \theta^{(\cdot)}_{\nu|\text{EST}}, \theta^{(\cdot)}_{\iota|\text{EST}}$ are estimations of the respective quantities.

The physics-informed have equivalently defined priors for receiving-end phasor quantities. However, we then introduce a latent prior for the temperature estimate as

$$p(T_{\text{EST}}) \sim \text{SN}\big(70,\ 10^2,\ -5\big)\,, \tag{4.25}$$

where $\text{SN}(\xi, \omega, \alpha)$ denotes the skew-normal distribution with location parameter $\xi$, scale parameter $\omega$, and shape parameter $\alpha$.

The negative shape parameter induces a left skew, concentrating most of the probability density below the mode while producing a long right tail. For this choice of parameters, the mode remains near 70 °C, while the mean is slightly shifted above the mode due to the skew, ensuring that higher temperatures are less probable but still allowed. This asymmetric prior therefore biases the posterior toward conservative, higher temperature estimates: it reduces the risk of underestimating the conductor temperature while preserving a small probability for extreme values.

With priors defined for the receiving-end phasors and the latent temperature, the transmission line $\pi$-model may be used to induce a prior predictive distribution over the sending-end quantities through deterministic physical transformations. By enforcing deterministic coupling between all phasor quantities, the measurements are no longer treated as conditionally independent, which constrains the feasible parameter space and improves identifiability of the latent states. As a result, uncertainty is shared across measurements in a physically consistent manner, leading to posterior contraction and a reduced sensitivity to noise in individual phasor observations.

### 4.3.3 Likelihood functions

The likelihood functions for the measured phasor angles and magnitudes are modelled as Normal distributions. Logarithms are applied to the magnitudes to stabilize numerical evaluation and to better account for the multiplicative errors:

$$\log(\nu^{(\cdot)}_{\text{OBS}}) \sim \mathcal{N}(\log \nu^{(\cdot)}_{\text{EST}}, \sigma^2_{\log \nu}), \quad \log(\iota^{(\cdot)}_{\text{OBS}}) \sim \mathcal{N}(\log \iota^{(\cdot)}_{\text{EST}}, \sigma^2_{\log \iota}), \tag{4.26}$$

where

$$\begin{aligned}\sigma^2_{\log\nu} &= \mathrm{Var}(\log \nu_{\mathrm{MEAS}}) \\ &= \mathrm{Var}(\log \nu \prod_{x\in\mathcal{X}_\mathcal{V}} (1 + r_x)) \\ &= \mathrm{Var}(\log \nu + \sum_{x\in X_V} \log(1 + r_x)) \\ &= \sum_{x\in X_V} \mathrm{Var}(\log(1 + r_x)),\end{aligned} \tag{4.27}$$

and analogously for $\sigma^2_{\log\iota}$. Phasor angles are modelled without said logarithms as

$$\theta^{(\cdot)}_{\nu|\mathrm{OBS}} \sim \mathcal{N}(\theta^{(\cdot)}_{\nu|\mathrm{EST}}, \sigma^2_{\theta_\nu}), \quad \theta^{(\cdot)}_{\iota|\mathrm{OBS}} \sim \mathcal{N}(\theta^{(\cdot)}_{\iota|\mathrm{EST}}, \sigma^2_{\theta_\iota}), \tag{4.28}$$

where

$$\begin{aligned}\sigma^2_{\theta_\nu} &= \mathrm{Var}(\theta_{\nu|\mathrm{MEAS}}), \\ &= \mathrm{Var}(\theta_\nu + \sum_{x\in X_V} \theta_x), \\ &= \sum_{x\in X_V} \mathrm{Var}(\theta_x)\end{aligned} \tag{4.29}$$

and analogously for $\sigma^2_{\theta_\iota}$.

### 4.3.4 Deterministic Relations for Temperature

With estimates in place, the conductor temperature can be deterministically defined using Equation (2.11) as

$$T_{\mathrm{AV}} \sim T_{\mathrm{ref}} + \frac{1}{\alpha}\left(\frac{s^{(s)}_{\mathrm{EST}} \cos\left(\phi^{(s)}_{\mathrm{EST}}\right) - s^{(r)}_{\mathrm{EST}} \cos\left(\phi^{(r)}_{\mathrm{EST}}\right)}{k_j R_{AC} I^2_{AC|\mathrm{EST}}} - 1\right) \tag{4.30}$$

with

$$s^{(\cdot)}_{\mathrm{EST}} = \nu^{(\cdot)}_{\mathrm{EST}} \cdot \iota^{(\cdot)}_{\mathrm{EST}}, \tag{4.31a}$$

$$\phi^{(\cdot)}_{\mathrm{EST}} = \theta^{(\cdot)}_{\nu|\mathrm{EST}} - \theta^{(\cdot)}_{\iota|\mathrm{EST}}, \tag{4.31b}$$

$$I_{AC|\mathrm{EST}} = \sqrt{(\iota^{(s)}_{\mathrm{EST}})^2 + (\iota^{(r)}_{\mathrm{EST}})^2}. \tag{4.31c}$$

### 4.3.5 Implementation of Soft Physical Constraints

Soft physical constraints are optionally applied to the inferred average conductor temperature $T_{\mathrm{AV}}$ in order to discourage thermally implausible operating conditions while

maintaining a fully Bayesian formulation.

Operational experience suggests that the conductor temperature typically remains within a bounded range when currents are near rated capacities, with boundaries $T_{\min} = 30$ and $T_{\max} = 70$. Rather than enforcing these limits as hard bounds, a quadratic penalty function is introduced outside the admissible interval:

$$\Psi(T) = \begin{cases} -\frac{1}{2}\left(\frac{T_{\min}-T}{\sigma_T}\right)^2, & T < T_{\min}, \\ 0, & T_{\min} \leq T \leq T_{\max}, \\ -\frac{1}{2}\left(\frac{T-T_{\max}}{\sigma_T}\right)^2, & T > T_{\max}, \end{cases} \tag{4.32}$$

where $\sigma_T = 10$ controls the softness of the constraint and determines how rapidly the penalty increases outside the feasible region.

This penalty is exponentiated and multiplied with the posterior density as resulting in a new posterior density as per equation (3.47), thereby modifying the posterior distribution without altering the likelihood or the deterministic physical model.

The chosen quadratic form ensures smoothness and differentiability across the entire parameter space, enabling efficient sampling with HMC/NUTS. Importantly, the soft constraint does not prevent excursions beyond the nominal temperature bounds but assigns them lower probability, allowing the inference to remain data-driven while respecting physical intuition.

### 4.3.6 Use of PyMC for Posterior Sampling

The posterior distributions in this work are estimated using PyMC, a probabilistic programming framework that allows models to be specified in terms of priors, likelihoods, and deterministic relationships. PyMC was selected because it provides straightforward support for gradient-based sampling algorithms, in particular HMC and its adaptive variant, NUTS [33]. For this purpose, acceptance rate was chosen as 95 %, and 4000 samples were drawn, with an additional 1000 for the warm-up phase. Sampling was done over four chains to ensure correct posterior estimation.

The framework also allows convenient extraction of posterior samples for further analysis, such as computing credible intervals or propagating uncertainty to derived quantities. The choice of PyMC thus reflects a balance between flexibility in model specification, ease of implementing HMC/NUTS, and the ability to obtain comprehensive posterior inference from a single framework.

## 4.4 Unscented Kalman Filtering for Temperature Estimation

For the application of the Unscented Kalman Filter, the state vector, measurement vector, and the corresponding non-linear state transition and measurement functions must be specified in accordance with (3.49). These definitions must enable prediction of the system state and measurements using only the current state estimate and the associated noise statistics.

The state and measurement vectors are defined as

$$\mathbf{x}_k = \begin{bmatrix} T_{\text{AV}} & \log \nu^{(r)} & \log \iota^{(r)} & \phi^{(r)} & \phi^{(s)} \end{bmatrix}^\top, \tag{4.33a}$$

$$\mathbf{z}_k = \begin{bmatrix} \log \nu^{(r)} & \log \iota^{(r)} & \phi^{(r)} & \log \nu^{(s)} & \log \iota^{(s)} & \phi^{(s)} \end{bmatrix}^\top. \tag{4.33b}$$

The state transition function is chosen as a random-walk model,

$$\boldsymbol{\chi}_{k|k-1}^{(i)} = f(\boldsymbol{\chi}_{k-1}) = \boldsymbol{\chi}_{k-1} + \mathbf{w}_k, \tag{4.34}$$

such that the state evolution is given by

$$\mathbf{x}_k = \mathbf{x}_{k-1} + \mathbf{w}_k, \tag{4.35}$$

where $\mathbf{w}_k \sim \mathcal{N}(\mathbf{0}, \mathbf{Q}_k)$ denotes zero-mean normal process noise with variances $\mathbf{Q}_k$. As a consequence, the sigma points defined in (3.50) are propagated almost unchanged through the state transition step according to (3.52). The predicted state distribution therefore represents a normally distributed random walk, where the growth of uncertainty is governed solely by $\mathbf{Q}_k$.

The measurement prediction is performed using a non-linear measurement function $h(\cdot)$ based on the transmission-line $\pi$-model. For each predicted sigma point $\boldsymbol{\chi}_{k|k-1}^{(i)}$, the corresponding predicted measurement sigma point $\boldsymbol{\gamma}_k^{(i)}$ is computed in accordance with (3.54). The function $h(\cdot)$ evaluates the $\pi$-model equations to compute the sending-end voltages, currents, and phase angles based on the current state estimate.

Measurement uncertainty is modelled as additive zero-mean normal noise,

$$\mathbf{v}_k \sim \mathcal{N}(\mathbf{0}, \mathbf{R}_k), \tag{4.36}$$

with covariance matrix $\mathbf{R}_k$. These uncertainties are incorporated in the predicted measurement covariance $\mathbf{S}_k$ as defined in (3.55).

By combining a stochastic random-walk state model with a physics-based $\pi$-model measurement function, the UKF enables consistent estimation of slowly varying system parameters while explicitly accounting for the non-linear electrical relationships between states and measurements. This method of estimation will be used for four different cases,

where the quantities may vary dynamically. From these estimates, graphs will be created showing temperature estimates compared to nominal temperature, including a confidence interval of 95 %. Furthermore, the RMSE and mean absolute error (MAE) will be calculated for each case.

### 4.4.1 Cases for Dynamic Quantities

Four cases will be studied over a measurement period of $n \in \{1, 10, 100\}$ minutes, assuming measurement frequency of $f_m = 6000$ measurements per minute, for the purpose of evaluating UKF as a means of estimating $T_{\text{AV}}$.

In the first case, small non-linear changes are applied to receiving current amplitude as well as nominal temperature. These changes will measure the models ability to estimate conductor temperature where only small changes are present, similar to the conditions that one would require for the static Bayesian inference. The measurements created here will serve as a baseline for the other cases, who will also include additional more drastic changes to nominal quantities.

The second case will have an additional convection-driven cooling, a step in convective heat transfer will cause a drop in nominal temperature $T_{\text{NOM}}$ modelled in similarity to the results in Lindberg [20], and this will be the dominant source of change in estimated quantities. As temperature decreases, the conductor resistance follows, altering the relationship between sending- and receiving-end phasors. These temperature-driven changes cause a gradual drift in voltage and current magnitudes and phase differences, which the UKF must interpret as a change in the underlying thermal state rather than as random disturbance. This scenario primarily evaluates the estimator's ability to track slow, smooth changes in the system parameters.

Current-driven heating will be added to the third case. The nominal current amplitude will include a step function in the middle of the measurement period. This step in current will induce a temperature increase as per Lindberg [20]. Here, changes in current directly affect both the measured phasors and the thermal state through Joule heating. As the current operating point shifts, the corresponding phasor magnitudes and angle differences change, effectively dragging the temperature estimate along with them. This case highlights the coupling between electrical loading and thermal dynamics, and tests the UKF's ability to adapt to current-induced variations.

Finally, a combined scenario is considered in which both convective heat transfer and current steps are introduced, at different times during the measurement period. This represents a more realistic operating condition, where environmental influences and load changes occur concurrently. In this case, the phasor measurements are influenced by multiple interacting factors, and the UKF must rely on the full non-linear measurement model to maintain a consistent estimate of the temperature. The results from this scenario demonstrate the robustness of the estimator under complex, time-varying conditions and

provide insight into its practical applicability.

### 4.4.2 Measurement generation

Synthetic measurement sequences are generated to evaluate the UKF performance under different operating conditions. All scenarios share a common nominal initialization of receiving-end quantities,

$$\{\nu^{(r)}\}_{i=1}^{m} = 138000, \tag{4.37a}$$

$$\{\iota^{(r)}\}_{i=1}^{m} = 800 + 25\sin\left(4\frac{i}{m}\right), \tag{4.37b}$$

$$\{\theta_{\nu}^{(r)}\}_{i=1}^{m} = 0, \tag{4.37c}$$

$$\{\theta_{\iota}^{(r)}\}_{i=1}^{m} = -\arccos(0.8) + 0.05\sin\left(4\frac{i}{m}\right), \tag{4.37d}$$

$$\{T_{\mathrm{NOM}}\}_{i=1}^{m} = 55 + 2\sin\left(5\frac{i}{m}\right), \tag{4.37e}$$

where $m = n \cdot f_m$ denotes the total number of measurements. The nominal temperature represents slow ambient variations in the absence of external disturbances.

To study the filter response to dynamic thermal behaviour, four scenarios are considered, corresponding to different combinations of convection- and current-driven effects:

1. **Baseline case**: No additional temperature or current perturbations are applied. The conductor temperature follows only the nominal variation $T_{\mathrm{NOM}}$.

2. **Convection-driven cooling**: A gradual temperature reduction is introduced to emulate increased convective cooling, modelled as a smooth transient. The updated nominal temperature becomes:

$$\{T_{\mathrm{NOM},i}\} = 55 + 2\sin\left(5\frac{i}{m}\right) - A_{\mathrm{conv}}\left(1 - e^{-\frac{i-i_c}{\tau_{\mathrm{conv}}}}\right)\mathbb{I}_{i\geq i_{\mathrm{conv}}}, \tag{4.38}$$

   where $A_{\mathrm{conv}} = 10$ is the cooling magnitude, $\tau_{\mathrm{conv}} = f_m \cdot 8$ the thermal time constant, $i_{\mathrm{conv}} = m \cdot \frac{1}{4}$ the onset index, and $\mathbb{I}$ the indicator function.

3. **Current-driven heating**: A step increase in current amplitude is applied to represent a load change,

$$\iota_i^{(r)} = 800 + 25\sin\left(4\frac{i}{m}\right) + \Delta I\,\mathbb{I}_{i\geq i_I}, \tag{4.39a}$$

$$T_{\mathrm{NOM},i} = 55 + 2\sin\left(5\frac{i}{m}\right) + A_{\mathrm{curr}}\left(1 - e^{-\frac{i-i_c}{\tau_{\mathrm{curr}}}}\right)\mathbb{I}_{i\geq i_{\mathrm{curr}}}, \tag{4.39b}$$

   which results in an indirect temperature rise through increased resistive losses. The

relevant constants are defined as $\Delta I = 400$, $A_{\text{curr}} = 15$ is the heating magnitude, $\tau_{\text{curr}} = f_m \cdot 13$ the thermal time constant, $i_{\text{curr}} = m \cdot \frac{1}{2}$ the onset index.

4. **Combined case**: Both convection-driven cooling and current-driven heating are applied simultaneously, yielding competing thermal effects,

$$\iota_i^{(r)} = 800 + 25 \sin\left(4\frac{i}{n}\right) + \Delta I \, \mathbb{I}_{i \geq i_I}, \tag{4.40a}$$

$$\begin{aligned} T_{\text{NOM},i} = 55 + 2 \sin\left(5\frac{i}{n}\right) - A_{\text{conv}} \left(1 - e^{-\frac{i-i_c}{\tau_{\text{conv}}}}\right) \mathbb{I}_{i \geq i_{\text{conv}}} \\ + A_{\text{curr}} \left(1 - e^{-\frac{i-i_c}{\tau_{\text{curr}}}}\right) \mathbb{I}_{i \geq i_{\text{curr}}}, \end{aligned} \tag{4.40b}$$

For each scenario, the receiving-end phasors and conductor temperature are used as inputs to the $\pi$-model to compute the corresponding sending-end phasors based on the Bohus conductor parameters. Measurement noise is then applied to all phasor magnitudes and angles according to the selected accuracy class and the uncertainties described in Tables 2.2, 2.3, and 2.4. As in Sections 4.1.4 and 4.3.1, secondary circuit uncertainties are reduced for higher accuracy classes to remain consistent with transformer uncertainty limits.

### 4.4.3 Measurement and Process Noise

The performance of the UKF is strongly influenced by the choice of measurement and process noise covariance matrices, $\mathbf{R}_k$ and $\mathbf{Q}_k$, respectively. These matrices determine the relative trust placed in the measurements and the state prediction.

**Measurement noise covariance** PMU magnitude errors are typically specified as relative uncertainties. If linear magnitudes are used directly, this would require $\mathbf{R}_k$ to be updated at each time step. By instead expressing voltage and current magnitudes in logarithmic form, relative magnitude errors are transformed into additive noise terms. As a result, the measurement noise covariance can be defined as time-invariant,

$$\mathbf{R}_k = \mathbf{R} = \begin{bmatrix} \sum_{x \in \mathcal{X}_V} \text{Var}[\log(1 + r_x)] \\ \sum_{x \in \mathcal{X}_C} \text{Var}[\log(1 + r_x)] \\ \sum_{x \in \mathcal{X}} \text{Var}(\theta_x) \\ \sum_{x \in \mathcal{X}_V} \text{Var}[\log(1 + r_x)] \\ \sum_{x \in \mathcal{X}_C} \text{Var}[\log(1 + r_x)) \\ \sum_{x \in \mathcal{X}} \text{Var}(\theta_x) \end{bmatrix}. \tag{4.41}$$

**Process noise covariance** The state evolution model is chosen as a random walk, as described in (4.35). Given the high reporting rate of PMUs, the process noise covariance

is selected to be small, such that the filter primarily relies on state prediction while allowing for slow temporal variations in the estimated quantities. This reduces sensitivity to measurement noise, while still permitting the state estimate to drift towards new operating points when persistent measurement deviations are observed.

A suitable baseline process noise covariance is defined as

$$\mathbf{Q}_0 = \frac{1}{5 \cdot f_m} \begin{bmatrix} 0.1 \\ 0.1 \\ 0.01 \\ 0.00001 \\ 0.00001 \end{bmatrix}. \tag{4.42}$$

This choice allows for the largest variations in the average conductor temperature, followed by phasor magnitudes, and finally the smallest variations in phasor angle differences.

**Adaptive process noise** To improve responsiveness during rapid system changes, the process noise covariance is adaptively increased when a significant mismatch between predicted and observed measurements is detected.

If the innovation magnitude exceeds a predefined threshold $\eta_{\text{th}}$, the process noise covariance is temporarily increased according to

$$\mathbf{Q}_k = \begin{cases} \gamma\, \mathbf{Q}_0, & \text{if } \eta_k > \eta_{\text{th}}, \\ \mathbf{Q}_0, & \text{otherwise}, \end{cases} \tag{4.43}$$

where $\gamma = 10$ is a scalar gain factor. This adaptive scaling increases the filter responsiveness to subsequent measurements, thereby enabling rapid convergence following abrupt changes such as step variations in current magnitude.

Due to the innovation magnitude being chi-squared distributed the threshold was chosen to be the 90-th percentile of the six degrees of freedom chi-squared distribution, $\eta_{th} = 10.6$. One could choose a higher percentile, but as UKF assumes normal errors, whereas the measurements actually follow distributions as per Figures 5.1-5.4, the tails of the normal distribution are actually less likely than the model assumes.

This adaptive process noise strategy preserves robustness during steady-state operation while allowing fast tracking of rapid quantity changes.

# 5 Results

## 5.1 Model Error Propagation

The model error given by Equation (4.1) can introduce temperature deviations of the order of magnitude shown in Tables 5.1 and 5.2. As seen in Table 5.1, the linearization of resistance leads to significant temperature errors at $T_{\mathrm{MO}}$ when the conductor–reference temperature difference is large (50 °C in this case), with errors exceeding 10 °C for the Bohus model and approaching this scale for the Gota model.

Table 5.1: Maximum errors caused by linearization of resistance for both conductor models.

| Conductor Model | $R_{\mathrm{AC}} l \alpha$ | $T_{\mathrm{MO}} - T_{\mathrm{ref}}$ [°C] | $T_{\mathrm{ERR}}$ [°C] |
|---|---|---|---|
| Bohus | 0.0051 | 50 | 12.67 |
| Gota | 0.0031 | 50 | 7.70 |

Table 5.2 shows that achieving small errors, e.g., $T_{\mathrm{ERR}} = 1$ or 0.1 °C, requires a substantially reduced temperature difference, on the order of only a few to tens of degrees Celsius, depending on conductor model.

Table 5.2: Maximum difference between conductor and reference temperatures to ensure temperature error smaller than specified for both conductor models.

| Conductor Model | $T_{\mathrm{ERR}} = 1$ | $T_{\mathrm{ERR}} = 0.1$ |
|---|---|---|
| Bohus | ± 14.00 | ± 4.28 |
| Gota | ± 17.96 | ± 5.68 |

## 5.2 Analytical Error Propagation

Below are the resulting analytical expressions for expected values, variances, and biases as taken forth using the method described in Section 4.1.

### 5.2.1 Expected Value of Measured Power

Assume the total ratio and phase errors on each side have means and variances

$$\mu_r^{(\cdot)} = \mathbb{E}(r_{2nd}^{(\cdot)}), \qquad \mu_\theta = \mathbb{E}(\sum_{x \in \mathcal{X}} \theta_x^{(\cdot)}), \tag{5.1a}$$

$$\sigma_r^2 = \mathrm{Var}(r_{2nd}^{(\cdot)}), \qquad \sigma_\theta^2 = \mathrm{Var}(\sum_{x \in \mathcal{X}} \theta_x^{(\cdot)}), \tag{5.1b}$$

, respectively, and are independent. The expected measured power is

$$\mathbb{E}[P_{\text{meas}}^{(\cdot)}] \approx \nu^{(\cdot)}\iota^{(\cdot)}\Big[\cos\phi^{(\cdot)} + \mu_r^{(\cdot)}\cos\phi^{(\cdot)} - \mu_\theta^{(\cdot)}\sin\phi^{(\cdot)} - \mu_r^{(\cdot)}\mu_\theta^{(\cdot)}\sin\phi^{(\cdot)} - \tfrac{1}{2}(\sigma_\theta^{2(\cdot)} + (\mu_\theta^{(\cdot)})^2)\cos\phi^{(\cdot)}\Big]. \tag{5.2}$$

### 5.2.2 Absolute Bias

The expected deviations from the true values are defined as

$$\Delta P_{\text{meas}}^{(\cdot)} \equiv \mathbb{E}[P_{\text{meas}}^{(\cdot)}] - P^{(\cdot)} \approx \nu^{(\cdot)}\iota^{(\cdot)}\mathcal{B}^{(\cdot)}, \tag{5.3a}$$

$$\Delta P_{\ell,\text{meas}} \equiv \Delta P_{\text{meas}}^{(s)} - \Delta P_{\text{meas}}^{(r)} \approx \nu^{(s)}\iota^{(s)}\mathcal{B}^{(s)} - \nu^{(r)}\iota^{(r)}\mathcal{B}^{(r)}, \tag{5.3b}$$

$$\Delta T_{A,\text{meas}} \equiv \frac{\Delta P_{\ell,\text{meas}}}{\alpha R_{AC} k_j I_{AC}^2}, \tag{5.3c}$$

where

$$\mathcal{B}^{(\cdot)} \equiv \mu_r^{(\cdot)}\cos\phi^{(\cdot)} - \mu_\theta^{(\cdot)}\sin\phi^{(\cdot)} - \mu_r^{(\cdot)}\mu_\theta^{(\cdot)}\sin\phi^{(\cdot)} - \tfrac{1}{2}(\sigma_\theta^{2(\cdot)} + (\mu_\theta^{(\cdot)})^2)\cos\phi^{(\cdot)}. \tag{5.4}$$

### 5.2.3 Relative Bias

The relative deviations can be calculated as

$$\delta P_\ell \equiv \frac{\mathbb{E}[P_{\ell,\text{meas}}]}{P_\ell} - 1 = \frac{\Delta P_{\ell,\text{meas}}}{P_\ell}, \tag{5.5a}$$

$$\delta T_A \equiv \frac{\mathbb{E}[T_{A,\text{meas}}]}{T_A} - 1 = \frac{\Delta T_{A,\text{meas}}}{T_A} \approx \frac{\nu^{(s)}\iota^{(s)}\mathcal{B}^{(s)} - \nu^{(r)}\iota^{(r)}\mathcal{B}^{(r)}}{\nu^{(s)}\iota^{(s)}\cos\phi^{(s)} - \nu^{(r)}\iota^{(r)}\cos\phi^{(r)}}. \tag{5.5b}$$

### 5.2.4 Temperature and Measured Power Variance

Using linearization for small $|\theta^{(\cdot)}|$:

$$\text{Var}(P_{\text{meas}}^{(\cdot)}) \approx (\nu^{(\cdot)}\iota^{(\cdot)})^2\Big[\cos^2(\phi^{(\cdot)})\text{Var}(r) + \sin^2(\phi^{(\cdot)})\text{Var}(\theta)\Big], \tag{5.6a}$$

$$\text{Var}(P_{\ell,\text{meas}}) = \text{Var}(P_{\text{meas}}^{(s)}) + \text{Var}(P_{\text{meas}}^{(r)}), \tag{5.6b}$$

$$\text{Var}(T_{A,\text{meas}}) \approx \left(\frac{1}{\alpha R_{AC} k_j I_{AC}^2}\right)^2 \text{Var}(P_{\ell,\text{meas}}). \tag{5.6c}$$

## 5.3 Monte Carlo Sampling for Error Propagation

The results of Monte Carlo uncertainty propagation are shown below. First, results will be brought forth using the same accuracy classes for potential and current transformers currently in use at Vattenfall Eldistribution AB. This will be followed by similar results for other accuracy classes, and lastly a clear comparison between the different accuracy classes' precision in temperature estimation.

### 5.3.1 Error for accuracy classes CT(5P), VT(0.2S)

The KDEs of current and voltage amplitudes, phase differences, and real powers, for both the sent and received ends are shown in Figure 5.1. Similarly, the KDEs of power loss and temperature are shown in Figure 5.2.

For the voltage and current amplitudes, as well as the phase angle differences, normal distribution fits are overlaid on top of the KDEs. These normal fits align with the empirical distributions, capturing both the central tendency and spread with good accuracy. However, the normal distributions concentrate probability mass around the mean more than the distributions for voltage amplitude and phase difference. Furthermore, the normal distribution allows tail-values that are not statistically present in the KDEs.

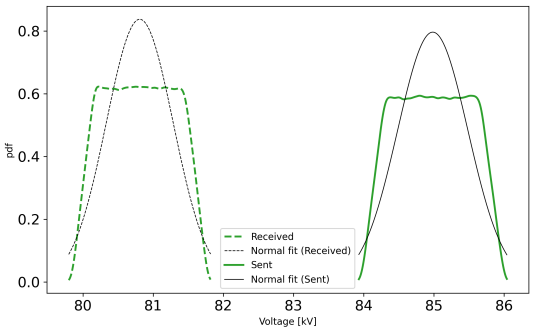


(a) Voltage amplitude
Rec: $\mu = 8.0809 \times 10^4$, $\sigma = 4.7660 \times 10^2$
Sent: $\mu = 8.4984 \times 10^4$, $\sigma = 5.0113 \times 10^2$

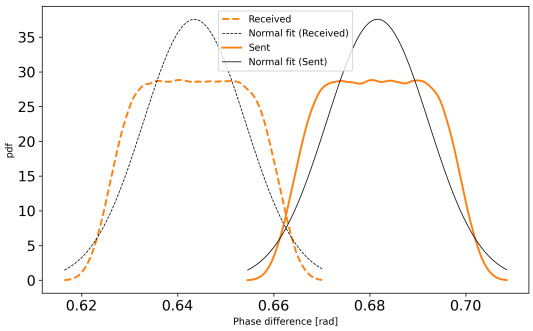


(c) Phase difference
Rec: $\mu = 0.6435$, $\sigma = 0.0106$
Sent: $\mu = 0.6816$, $\sigma = 0.0106$

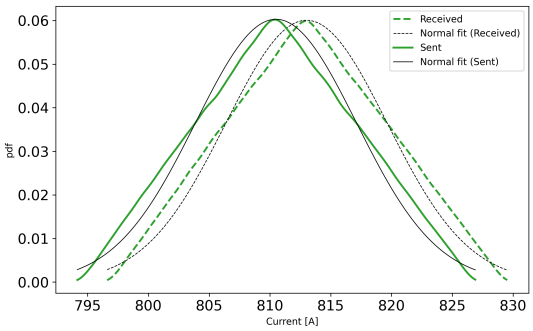


(b) Current amplitude
Rec: $\mu = 813.01$, $\sigma = 6.64$
Sent: $\mu = 810.50$, $\sigma = 6.62$

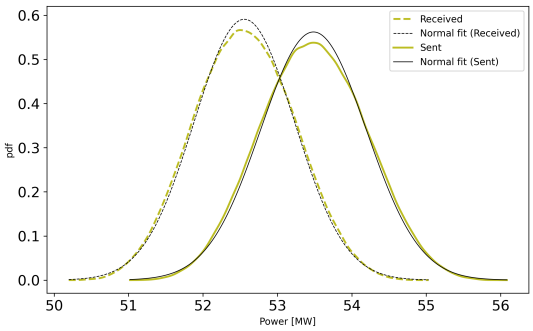


(d) Real power
Rec: $\mu = 5.2556 \times 10^7$, $\sigma = 6.7505 \times 10^5$
Sent: $\mu = 5.3485 \times 10^7$, $\sigma = 7.0959 \times 10^5$

Figure 5.1: KDEs of sent and received voltage and current amplitudes, phase differences, and real powers using accuracy classes CT(5P) and VT(0.2S).

### 5.3.2 Error for accuracy classes CT(0.1), VT(0.2S)

The KDEs of current and voltage amplitudes, phase differences, and real powers, for both the sent and received ends are shown in Figure 5.3. Similarly, the KDEs of power loss and temperature are shown in Figure 5.4.

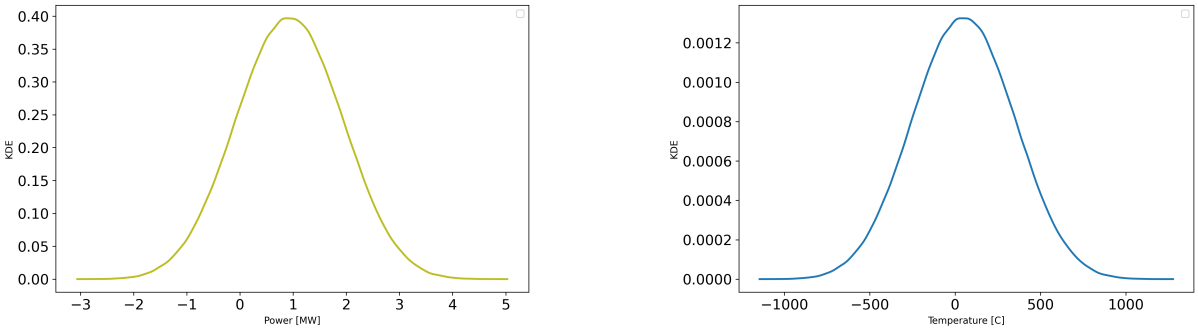


(a) Power loss
$\mu = 9.2881 \times 10^5$, $\sigma = 9.7934 \times 10^5$

(b) Temperature
$\mu = 50.008°\text{C}$, $\sigma = 293.28°\text{C}$

Figure 5.2: KDEs of power loss and temperature using accuracy classes CT(5P) and VT(0.2S).

For the voltage and current amplitudes, as well as the phase angle differences, normal distribution fits are overlaid on top of the KDEs. In this case, the normal fits are very well suited to the empirical distributions, showing close agreement in both central tendency and spread for the sent and received quantities. The sampled errors are of more similar magnitude, leading to distributions that more closely approximate normal behaviour, which is reflected in the strong alignment between the fitted normal curves and the KDEs.

### 5.3.3 Temperature Standard Deviation per Conductor Model

Sweeping over currents between 500 and 2200 A results in temperature standard deviations as shown in Figure 5.5. The lines have been highlighted within the interval $\left[0.8I^C_{\text{RATE}},, 1.2I^A_{\text{RATE}}\right]$ for the respective conductor models to indicate the expected operational loading range.

Within this interval, the two conductor models exhibit very similar temperature standard deviations. Despite differences in their physical parameterisations, the propagated measurement uncertainties lead to comparable spreads in the inferred temperature.

## 5.4 Sobol indices

Sobol indices were taken forth to emphasize the main contributors to temperature variance. To begin with, Sobol-indices of the first order will be introduced, with analytical expressions, numerically computed indices for all error sources, and lastly a Sobol indices over a sweep of power factors. Then, expressions and numerical computations of second-order Sobol indices will be introduced. Lastly, numerically computed total-effect Sobol indices will be shown.

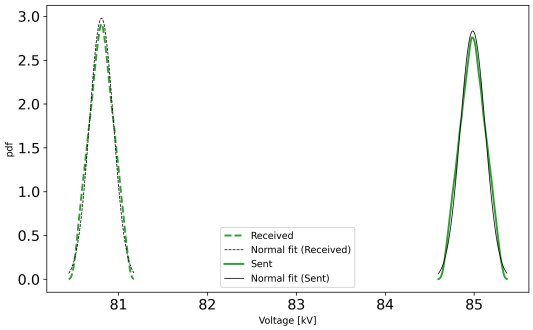


(a) Voltage amplitude
Rec: $\mu = 8.0809 \times 10^4$, $\sigma = 1.3395 \times 10^2$
Sent: $\mu = 8.4984 \times 10^4$, $\sigma = 1.4080 \times 10^2$

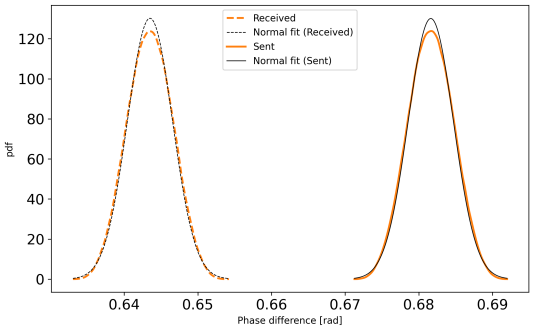


(c) Phase difference
Rec: $\mu = 0.6435$, $\sigma = 0.0031$
Sent: $\mu = 0.6816$, $\sigma = 0.0031$

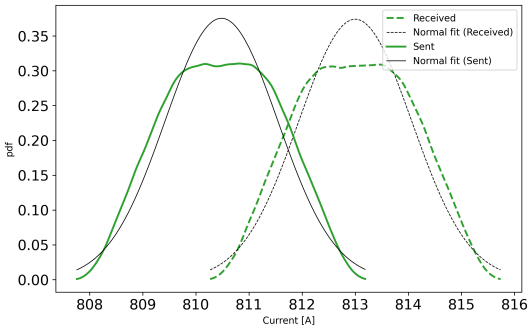


(b) Current amplitude
Rec: $\mu = 813.00$, $\sigma = 1.07$
Sent: $\mu = 810.48$, $\sigma = 1.06$

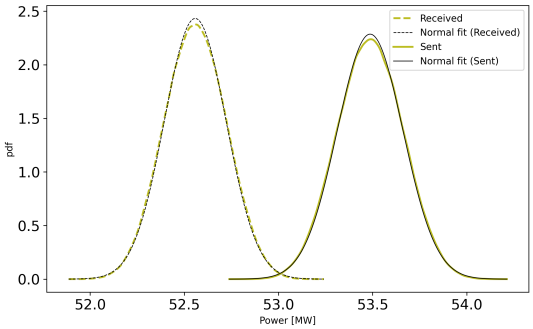


(d) Real power
Rec: $\mu = 5.2558 \times 10^7$, $\sigma = 1.6405 \times 10^5$
Sent: $\mu = 5.3487 \times 10^7$, $\sigma = 1.7454 \times 10^5$

Figure 5.3: KDEs of sent and received voltage and current amplitudes, phase differences, and real powers using accuracy classes CT(0.1) and VT(0.2S).

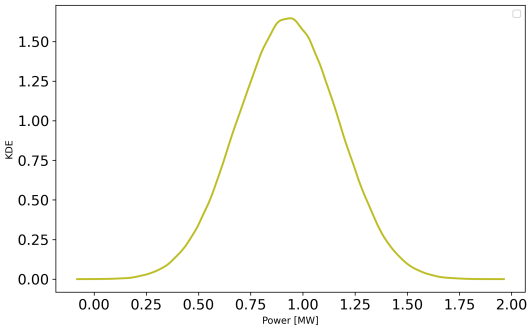


(a) Power loss
$\mu = 9.2866 \times 10^5$, $\sigma = 2.3960 \times 10^5$

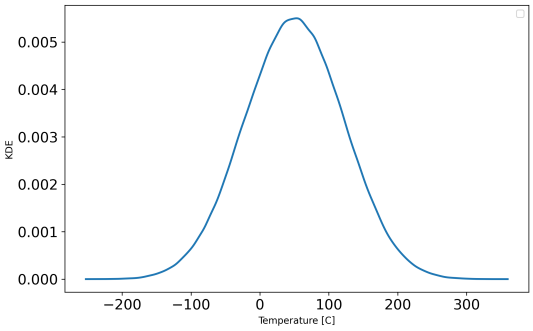


(b) Temperature
$\mu = 49.961°\text{C}$, $\sigma = 71.753°\text{C}$

Figure 5.4: KDEs of power loss and temperature using accuracy classes CT(0.1) and VT(0.2S).

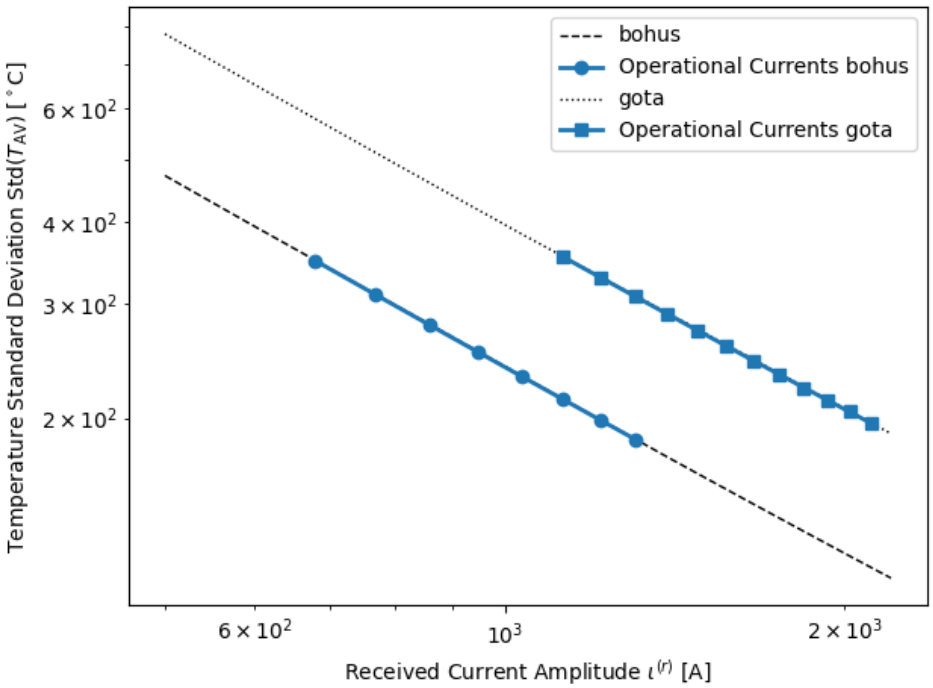


Figure 5.5: Temperature standard deviation over current for models bohus and gota using accuracy class CT(5P) VT(0.2S)

### 5.4.1 First-order contributions

Second order truncation of magnitude errors and second order approximations of cosines yields analytical expressions for first-order Sobol-indices as

$$S_{\tilde{r}_x^{(\cdot)}} = \frac{(\bar{A}^{(\cdot)} C'^{(\cdot)})^2 \operatorname{Var}(\tilde{r}_x^{(\cdot)})}{\operatorname{Var}(P_{\ell,\mathrm{meas}})}, \qquad S_{\tilde{\theta}_x^{(\cdot)}} = \frac{(\bar{A}^{(\cdot)} S'^{(\cdot)})^2 \operatorname{Var}(\tilde{\theta}_x^{(\cdot)})}{\operatorname{Var}(P_{\ell,\mathrm{meas}})}. \tag{5.7}$$

Furthermore, numerical computation for accuracy classes of choice give Sobol indices as per Figure 5.6.

Sweeping over multiple values of the power factor and summing all first-order Sobol indices associated with magnitude and phase errors yields the trends shown in Figure 5.7.

A clear shift in variance attribution is observed across the power-factor range. For higher power factors, where voltage and current phasors are more closely aligned, magnitude errors dominate the temperature variance. In this regime, real power transfer is driven primarily by amplitude terms, making the temperature estimate most sensitive to measurement uncertainty in voltage and current magnitudes.

Conversely, at lower power factors, phase-angle errors become the principal contributors to temperature variance. As the angular separation between phasors increases, the real-power calculation becomes more sensitive to phase differences, and uncertainty in angle measurements correspondingly exerts a stronger influence on the inferred temperature.

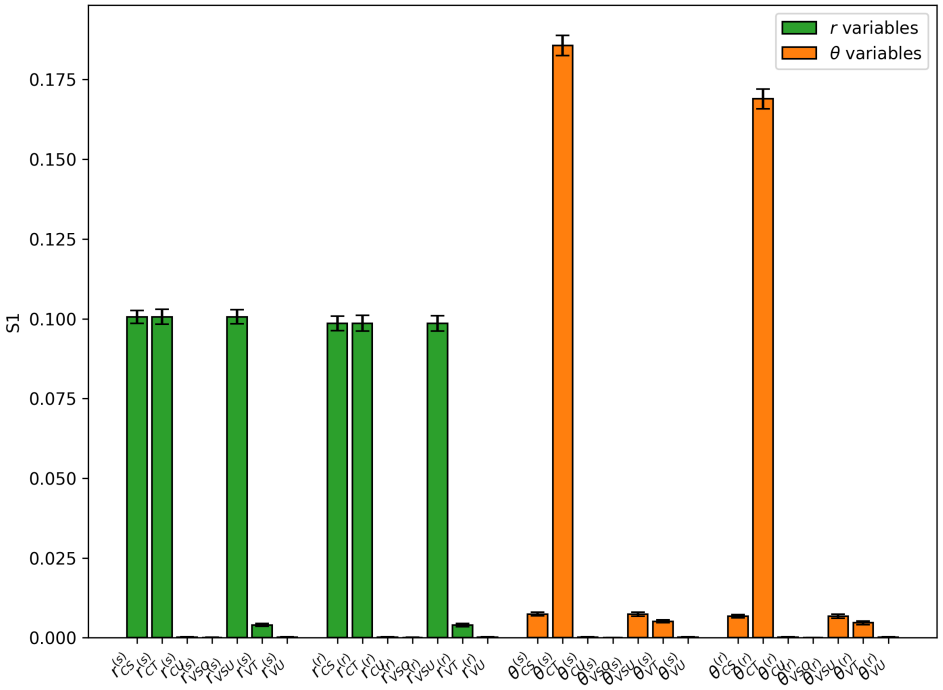


(a) Accuracy classes CT(5P) VT(0.2S)

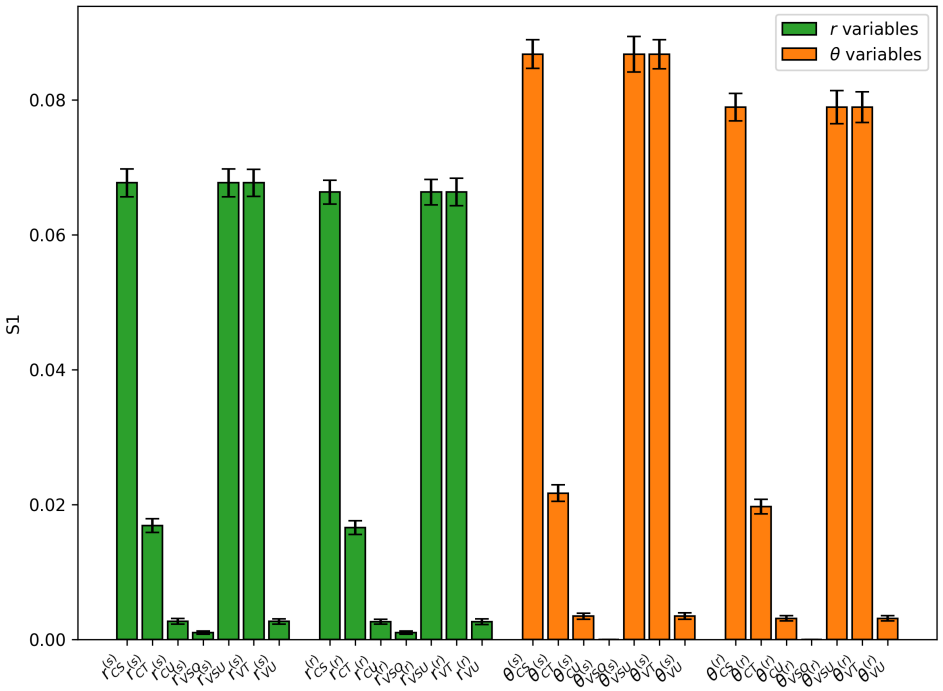


(b) Accuracy classes CT(0.1) VT(0.2S)

Figure 5.6: First-order Sobol indices.

Interaction effects remain almost negligible throughout the sweep. The summed contribution of higher-order Sobol terms is close to zero across the full power-factor interval, confirming that variance contributions are overwhelmingly governed by first-order effects. This behaviour aligns with analytical expectations, where cross-coupling between magnitude and angle uncertainties enters only weakly into the temperature formulation.

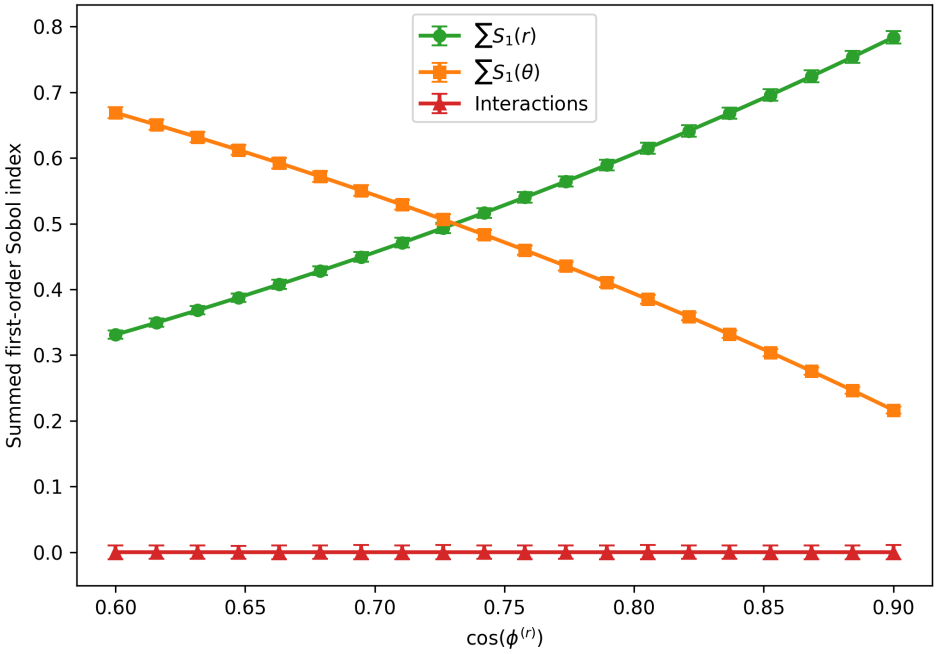


Figure 5.7: Magnitude and phase Sobol-indices over received end power factor for accuracy classes CT(5P) VT(0.2S).

### 5.4.2 Second-order and cross-branch interactions

The second-order interaction terms are defined as

$$S_{\tilde{r}_x^{(a)},\tilde{r}_y^{(b)}} = \frac{(\bar{A}^{(a)}C'^{(a)})(\bar{A}^{(b)}C'^{(b)})\,\mathrm{Var}(\tilde{r}_x^{(a)}\cdot\tilde{r}_y^{(b)})}{\mathrm{Var}(P_{\ell,\mathrm{meas}})}, \tag{5.8a}$$

$$S_{\tilde{r}_x^{(a)},\tilde{\theta}_y^{(b)}} = \frac{(\bar{A}^{(a)}C'^{(a)})(\bar{A}^{(b)}S'^{(b)})\,\mathrm{Var}(\tilde{r}_x^{(a)}\cdot\tilde{\theta}_y^{(b)})}{\mathrm{Var}(P_{\ell,\mathrm{meas}})}, \tag{5.8b}$$

$$S_{\tilde{\theta}_x^{(a)},\tilde{\theta}_y^{(b)}} = \frac{(\bar{A}^{(a)}S'^{(a)})(\bar{A}^{(b)}S'^{(b)})\,\mathrm{Var}(\tilde{\theta}_x^{(a)}\cdot\tilde{\theta}_y^{(b)})}{\mathrm{Var}(P_{\ell,\mathrm{meas}})}, \tag{5.8c}$$

where $(a),(b)\in\{(r),(s)\}$, and $(a)\neq(b)$ gives cross-branch terms. The numerical computations for accuracy classes CT(5P), VT(0.2S) yield the second-order Sobol sensitivity indices shown in Figure 5.8. To better resolve interaction structure, the indices are separated by interaction type and presented in three individual figures: magnitude–magnitude interactions in Figure 5.8a, angle–angle interactions in Figure 5.8b, and mixed magnitude–angle interactions in Figure 5.8c.

Across all interaction categories, the computed second-order indices remain extremely small. Even the largest interaction terms are on the order of $10^{-6}$ or lower, indicating a negligible contribution to the total variance of the inferred temperature. This behaviour is consistent with what was shown in Figure 5.7, where the sum of all interaction terms is almost negligible compared to first-order indices. Consequently, the temperature variance is dominated by first-order effects, with higher-order measurement interactions contributing only marginally.

### 5.4.3 Total-Effect Sobol Indices

The analytical expressions for total-effect Sobol indices for a source of error is easily defined as it's first-order index summed with all it's second-order interactions. The numerical computations are as per Figure 5.9. Further corroborating the assumption that second and higher-order interactions are negligible in size is the appearance of these indices as almost equivalent to the first order indices as presented in Figure 5.6.

## 5.5 Temperature Inference

This subsection presents results on temperature inference based on artificially generated measurements. We begin by introducing Bayesian inference results obtained from a single measurement, examining the impact of different prior choices and transformer accuracy classes. We then extend the analysis to the estimation of static temperatures using multiple measurements within the Bayesian framework. Finally, we present results for inferring conductor temperature from dynamic measurement data.

### 5.5.1 Single Measurement Static Estimation

Using the same conductor parameters, accuracy classes, and nominal phasors as in Section 5.3.1, the sampled measurements yield the posterior temperature distributions shown in Figures 5.10a and 5.10b for the different prior formulations. When a soft physical temperature constraint, as introduced in Section 4.3.5, is additionally imposed, the resulting posterior is shown in Figure 5.10c.

A clear contrast is observed between the three cases. Using only the engineer-informed prior without any physical regularization produces an extremely diffuse posterior, spanning a wide temperature range.

The introduction of either a physics-informed prior or a soft temperature constraint leads to a drastic contraction of the posterior distribution, as seen in Figures 5.10b, 5.10c, and more clearly in the rescaled comparison of Figure 5.11. With only a single measurement available, the likelihood contributes limited information in both formulations, and the resulting posteriors are therefore strongly governed by how the prior knowledge or constraint is specified.

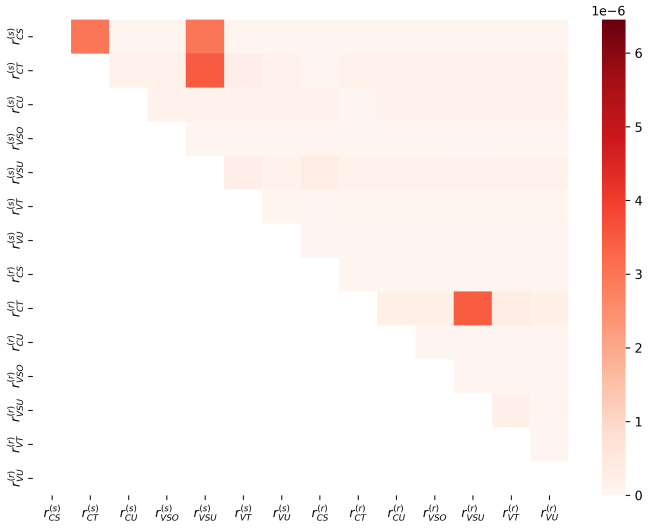


(a) Magnitude–magnitude interactions

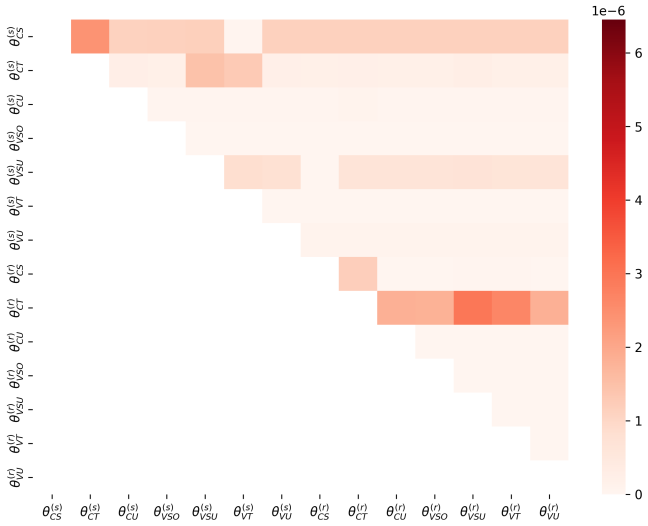


(b) Angle–angle interactions

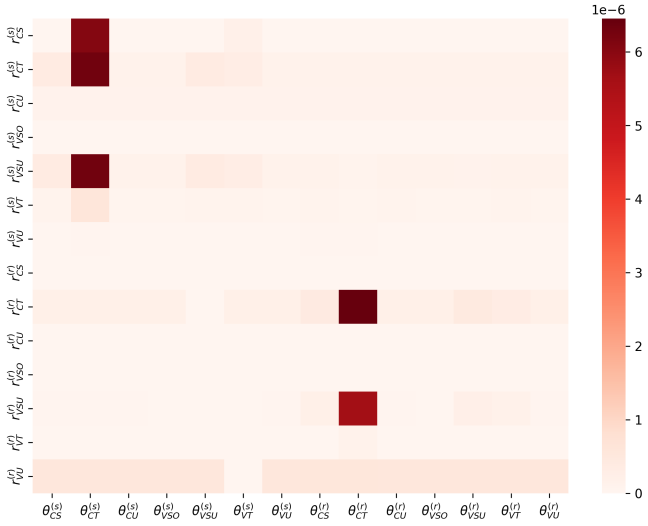


(c) Magnitude–angle interactions

Figure 5.8: Second-order Sobol indices split by variable types.

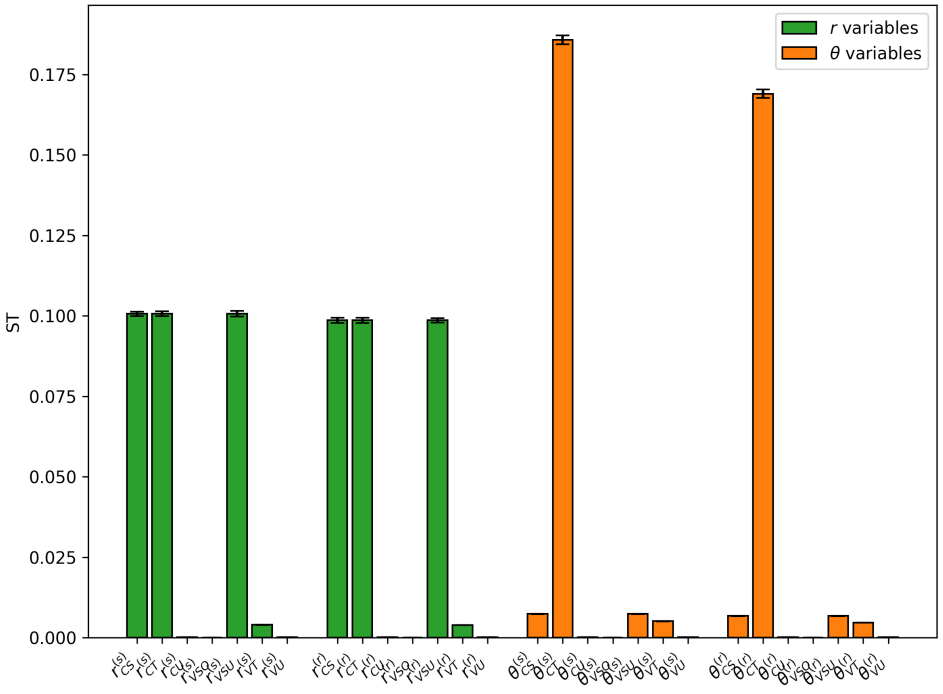


(a) Accuracy classes CT(5P) VT(0.2S)

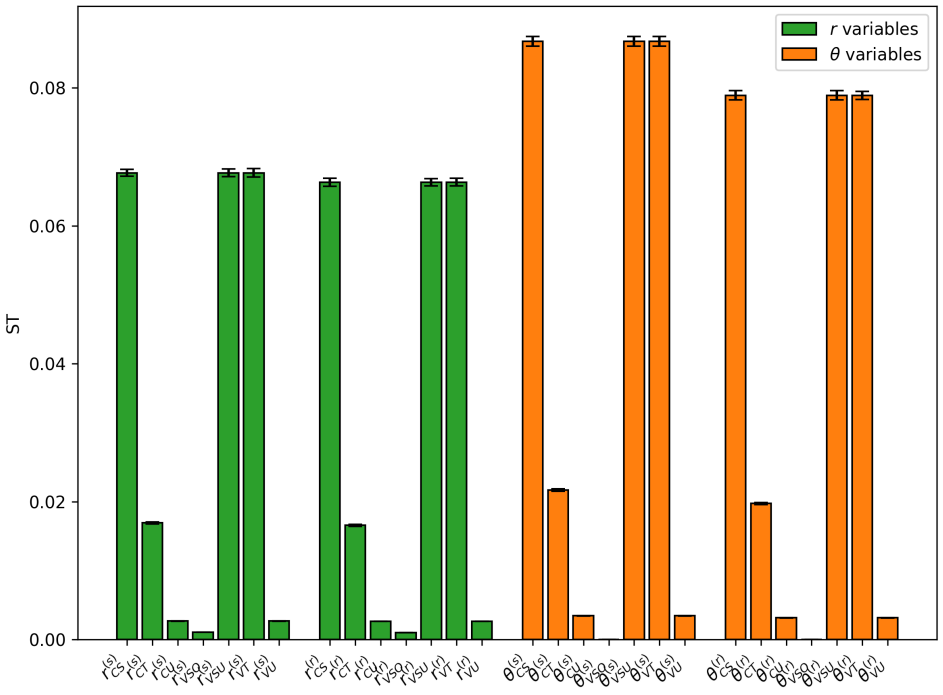


(b) Accuracy classes CT(0.1) VT(0.2S)

Figure 5.9: Total-effect Sobol indices.

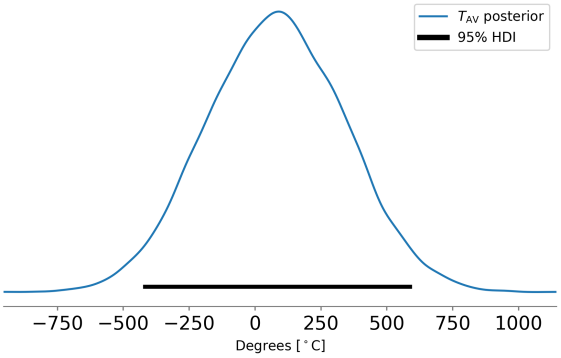


(a) Engineer-informed prior without physical constraint. Posterior mean 80.52 °C, mode 90.03 °C, variance $6.8892 \times 10^4$. The 95 % HDI spans [−424.96, 595.31] °C with half-width 510.14 °C.

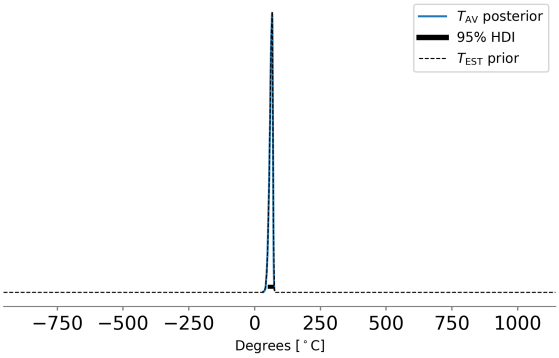


(b) Physics-informed prior without physical constraint. Posterior mean 62.02 °C, mode 66.58 °C, variance 39.40. The 95 % HDI spans [49.24, 72.18] °C with half-width 11.47 °C.

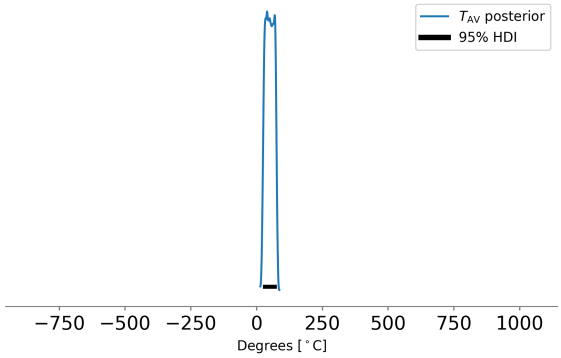


(c) Engineer-informed prior with physical constraint. Posterior mean 50.21 °C, mode 39.83 °C, variance 241.35. The 95 % HDI spans [23.93, 76.53] °C with half-width 26.30 °C.

Figure 5.10: Posterior temperature distributions for a single measurement using instrument transformer accuracy classes CT(5P) and VT(0.2S). The nominal conductor temperature is $T_{\mathrm{NOM}} = 50$ °C. The three cases compare the influence of engineer-informed and physics-informed priors, as well as the inclusion of a soft physical temperature constraint, on the inferred average conductor temperature.

For the physics-informed prior, this manifests as pronounced regularization, concentrating probability mass around the temperature prior and producing a sharply peaked posterior.

In contrast, the soft temperature constraint yields a posterior that, while restricted to a physically admissible interval, remains comparatively uniform across much of that domain, as evident in Figure 5.11b.

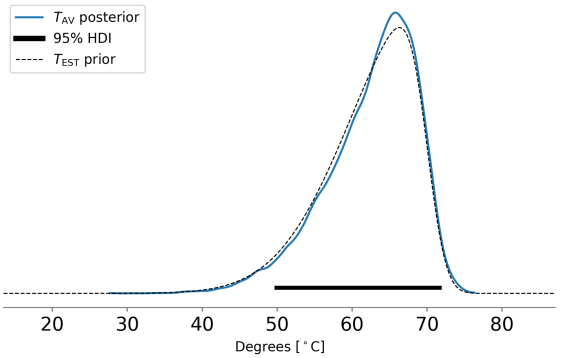


(a) Physics-informed prior without physical constraint. Posterior mean 62.02 °C, mode 66.58 °C, variance 39.40. The 95 % HDI spans [49.24, 72.18] °C with half-width 11.47 °C.

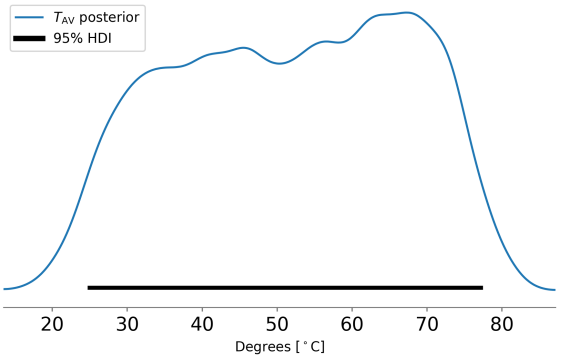


(b) Engineer-informed prior with physical constraint. Posterior mean 50.21 °C, mode 39.83 °C, variance 241.35. The 95 % HDI spans [23.93, 76.53] °C with half-width 26.30 °C.

Figure 5.11: Posterior temperature distributions for a single measurement using instrument transformer accuracy classes CT(5P) and VT(0.2S), with nominal conductor temperature $T_{\mathrm{NOM}} = 50$ °C. The engineer-informed prior without constraint is omitted to avoid axis scaling dominated by its extreme spread.

With increased instrument transformer accuracy, using classes CT(0.1) and VT(0.2S), the resulting posteriors are shown in Figures 5.12 and, for improved visualization of distributional shape, Figure 5.13.

Relative to the low-accuracy case, the engineer-informed prior without physical constraint now exhibits a noticeable contraction, nevertheless remaining substantially more diffuse than it's counterparts.

For the physics-informed prior and the soft temperature constraint, the inference continues to be dominated primarily by their respective regularization mechanisms. The physics-informed prior again concentrates probability mass tightly around thermally plausible temperatures, whereas the soft constraint mainly truncates the posterior support without strongly sharpening the distribution within the admissible interval, as more clearly seen in Figure 5.13b.

For each prior configuration, the measurement accuracy was increased by introducing a scaling factor $\eta$ applied uniformly to all uncertainty intervals listed in Tables 2.2, 2.3, and 2.4. This scaling enables an assessment of the instrumental accuracy required for the 95, % HDI to be fully contained within the operational tolerance band $T_{\mathrm{NOM}} \pm 5$ °C. The resulting posteriors for $\eta = \frac{1}{50}$ are shown in Figure 5.14.

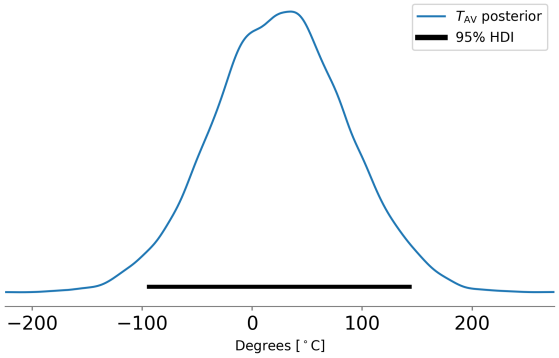


(a) Engineer-informed prior without physical constraint. Posterior mean 25.55 °C, mode 33.98 °C, variance $3.7324 \times 10^3$. The 95 % HDI spans [−95.93, 144.74] °C with half-width 120.33 °C.

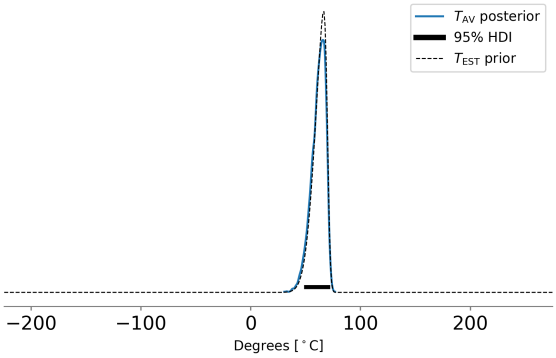


(b) Physics-informed prior without physical constraint. Posterior mean 61.44 °C, mode 65.61 °C, variance 42.73. The 95 % HDI spans [48.41, 72.35] °C with half-width 11.97 °C.

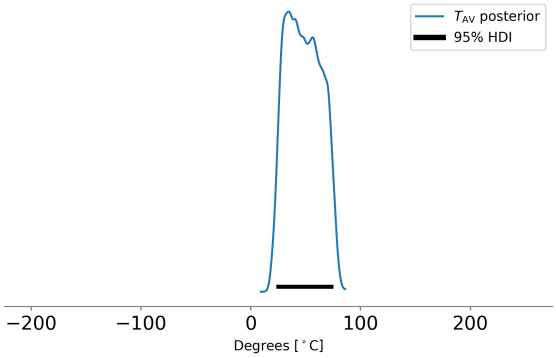


(c) Engineer-informed prior with physical constraint. Posterior mean 48.36 °C, mode 34.20 °C, variance 232.88. The 95 % HDI spans [23.00, 75.21] °C with half-width 26.10 °C.

Figure 5.12: Posterior temperature distributions for a single measurement using high-accuracy instrument transformer classes CT(0.1) and VT(0.2S). The nominal conductor temperature is $T_{\mathrm{NOM}} = 50$ °C. The two cases compare physics-informed priors and the effect of introducing a soft physical temperature constraint on the inferred average conductor temperature.

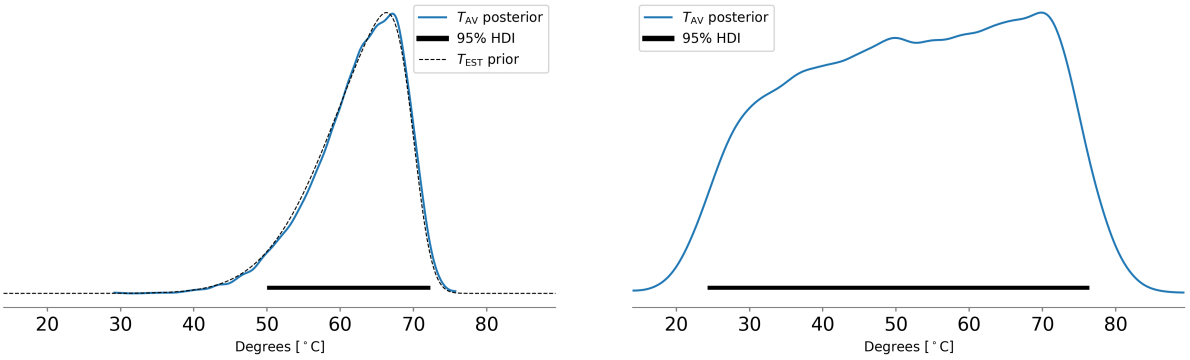


(a) Physics-informed prior without physical constraint. Posterior mean 61.44 °C, mode 65.61 °C, variance 42.73. The 95 % HDI spans [48.41, 72.35] °C with half-width 11.97 °C.

(b) Engineer-informed prior with physical constraint. Posterior mean 48.36 °C, mode 34.20 °C, variance 232.88. The 95 % HDI spans [23.00, 75.21] °C with half-width 26.10 °C.

Figure 5.13: Posterior temperature distributions for a single measurement using high-accuracy instrument transformer classes CT(0.1) and VT(0.2S). The nominal conductor temperature is $T_{\mathrm{NOM}} = 50$ °C. The engineer-informed prior without constraint is omitted to avoid axis scaling dominated by its extreme spread.

At this accuracy level a strong posterior contraction can be noted across all prior configurations. Furthermore, the engineer-informed configuration results in a posterior almost entirely within the constraint bounds, leading to near equivalence between the two configurations using the engineer-informed prior. The physics-informed prior still yields the most localized posterior; however, this increased precision is no longer concentrated

Thus, when the measurement uncertainties are reduced by the factor $\eta$, the estimation problem transitions into a likelihood-dominated regime in which posterior concentration is dictated primarily by data fidelity rather than by prior modelling choices.

### 5.5.2 Multiple measurements, static estimation

Using 100 measurement sets produces the posterior distributions shown in Figure 5.15, obtained with instrument transformer accuracy classes CT(5P) and VT(0.2S).

The inclusion of multiple measurements leads to a clear contraction of the posterior relative to the single-measurement case with similar accuracy classes, reflecting the cumulative information gained through repeated observations.

Despite this contraction, the combined information remains insufficient to fully confine the 95 % HDI within the operational tolerance band $T_{\mathrm{NOM}} \pm 5$ °C. The engineer-informed prior without constraint still yields a comparatively broad posterior, indicating that measurement information alone — even aggregated over 100 samples — is not strong enough to tightly localize the temperature estimate under the currently available accuracy classes.

The physics-informed prior produces the most concentrated posterior among the three cases, reflecting the additive effect of physically structured prior information and the

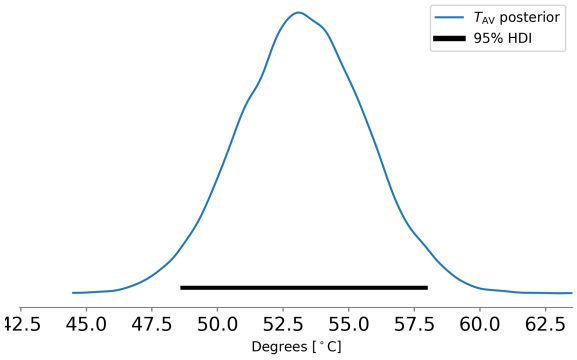


(a) Engineer-informed prior without physical constraint. Posterior mean 53.25 °C, mode 53.09 °C, variance 5.80. The 95 % HDI spans [48.57, 58.00] °C with half-width 4.71 °C.

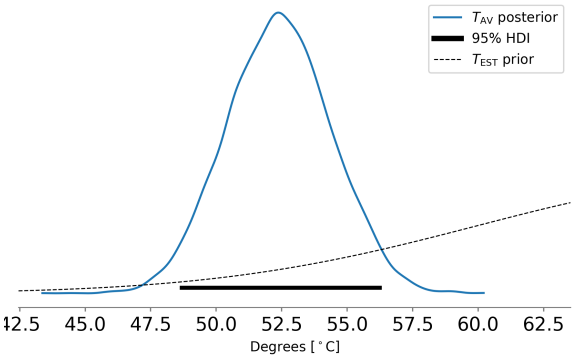


(b) Physics-informed prior without physical constraint. Posterior mean 52.38 °C, mode 52.36 °C, variance 3.98. The 95 % HDI spans [48.60, 56.31] °C with half-width 3.86 °C.

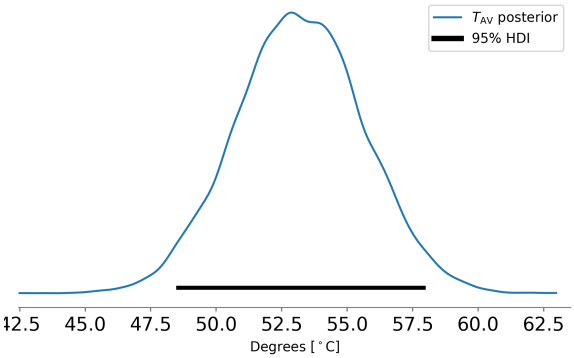


(c) Engineer-informed prior with physical constraint. Posterior mean 53.16 °C, mode 52.86 °C, variance 5.94. The 95 % HDI spans [48.47, 57.98] °C with half-width 4.76 °C.

Figure 5.14: Posterior temperature distributions for a single measurement using instrument transformer accuracy classes CT(0.1) and VT(0.2S), with error intervals scaled by a factor $\eta = \frac{1}{25}$. The nominal conductor temperature is $T_{\mathrm{NOM}} = 50$ °C. The three cases compare the influence of engineer-informed and physics-informed priors, as well as the inclusion of a soft physical temperature constraint, on the inferred average conductor temperature.

accumulated likelihood. Meanwhile, the introduction of a soft temperature constraint provides additional truncation of non-physical regions but does not lead to a contraction sufficient to meet the operational tolerance requirement.

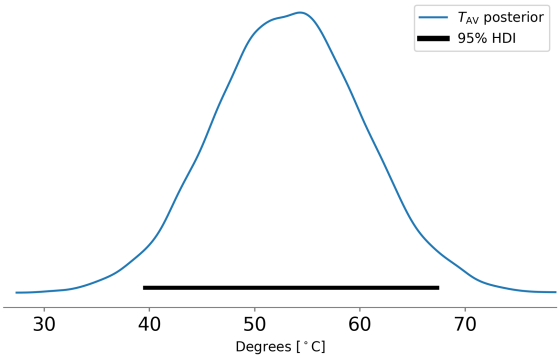


(a) Engineer-informed prior without physical constraint. Posterior mean 53.26 °C, mode 54.30 °C, variance 50.84. The 95 % HDI spans [39.40, 67.54] °C with half-width 14.07 °C.

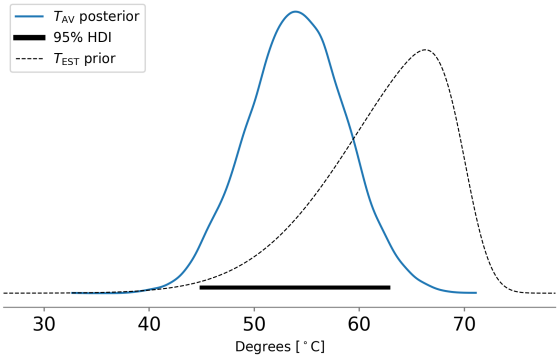


(b) Physics-informed prior without physical constraint. Posterior mean 53.98 °C, mode 53.90 °C, variance 21.81. The 95 % HDI spans [44.78, 62.95] °C with half-width 9.08 °C.

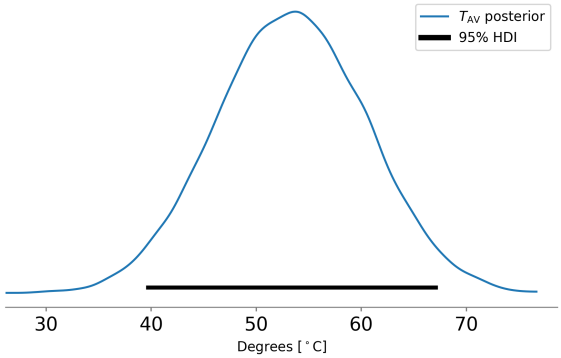


(c) Engineer-informed prior with physical constraint. Posterior mean 53.34 °C, mode 53.73 °C, variance 50.69. The 95 % HDI spans [39.50, 67.28] °C with half-width 13.89 °C.

Figure 5.15: Posterior temperature distributions obtained from 100 independent measurements using instrument transformer accuracy classes CT(0.1) and VT(0.2S). The nominal conductor temperature is $T_{\mathrm{NOM}} = 50$ °C.

For varying numbers of measurements N, the trends of the HDI half-width were evaluated to assess posterior contraction, see Figures 5.16a and 5.16b. Higher HDI percentages require more measurements to reduce the half-width below the given operational tolerance. Conversely, higher instrument transformer accuracy classes reduce the number of measurements needed to achieve the same level of posterior precision.

The choice of prior also strongly influences the convergence behaviour. Engineer-informed priors are weakly informative, meaning that the total information accumulates slowly with the number of measurements. This is reflected in the approximate exponential decay of the HDI half-width with increasing N, which appears as linear trends on the

logarithmic plots. In contrast, the physics-informed prior is highly informative from the outset. When only a few measurements are available, the measurements contributes relatively little, and the posterior is dominated by the prior. As more measurements are added, the likelihood gradually becomes more influential, leading to the same overall information gain as with the engineer-informed prior, but requiring fewer measurements in total due to the higher baseline information.

Similarly to the HDI half-width, the trend of posterior RMSE clearly indicates that it diminishes with increased number of measurements, and it benefits from improved accuracy classes, see Figure 5.17a. This behaviour is mirrored in the absolute temperature difference, shown in Figure 5.17b, where the magnitude of the estimation bias decreases as more measurements are incorporated. However, the prior choice influences the bias characteristics differently. The engineer-informed prior exhibits fluctuations between overestimation and underestimation of the temperature, indicating a less consistent directional bias. In contrast, the physics-informed prior consistently overestimates the temperature across the measurement range, only converging toward negligible bias once the absolute temperature difference falls below approximately one degree.

### 5.5.3 Multiple Measurements Dynamic Estimation

The results of estimating conductor temperature from multiple dynamic phasor measurements, rather than static operating points, are presented in Figure 5.18 for all cases, for measurement instrument accuracy classes CT(5P) and VT(0.2S). Figure 5.19 extends results by showing difference between estimated and nominal temperature, and clearly illustrating the wanted ±5 °C accuracy bounds. For all cases, there is a brief period in the beginning, where uncertainty is high and estimates vary dramatically, but after a short period the estimates converge toward the nominal temperatures. Furthermore, temperature difference appears very similar for all cases.

Using a higher accuracy class for the combination case yields temperature estimates and differences as per Figure 5.20. The temperature estimates show significantly higher accuracy and precision, significantly reducing the number of estimates outside the ±5 °C accuracy bound, albeit not to zero. Furthermore, the initial period of high uncertainty is not as stark as when using lower accuracy classes.

The corresponding Kalman gain per state for each case when using accuracy classes CT(5P) and VT(0.2S) is shown in Figure 5.21. The baseline and convection-driven cooling cases appear very similar, but the current-driven heating induces a large spikes at the point in time where the step in current magnitude is introduced. The spikes shows a reduction for current magnitude, and increase for conductor temperature. The combination case appears very similar to the current-driven heating case, which is expected, as the convection-driven cooling induced no significant changes in Kalman gain for any state.

Inducing the changes occurring for the combination-driven changes case over signifi-

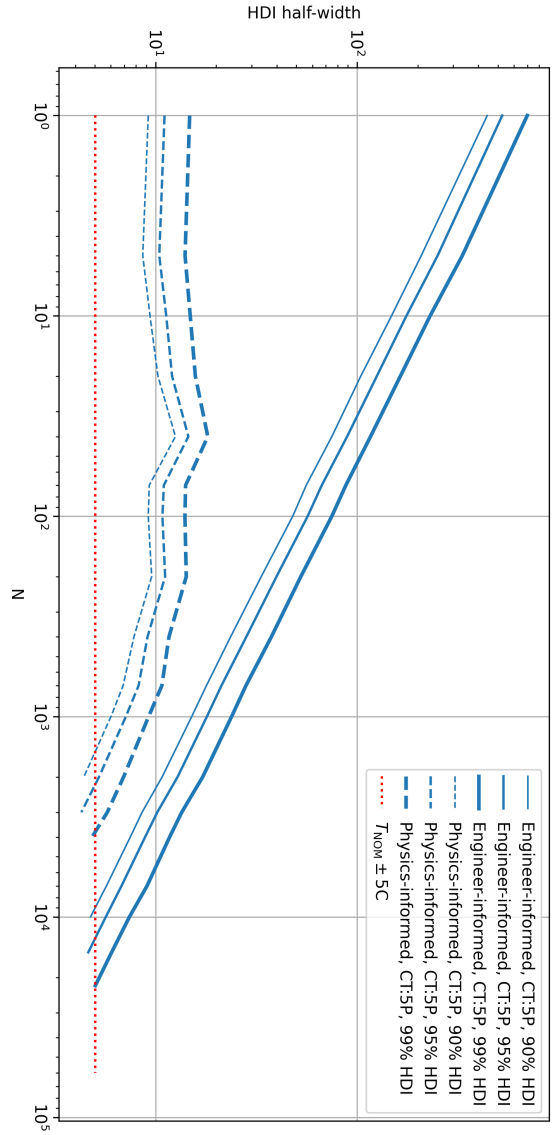


(a) HDI half-width versus number of measurements for different prior choices and credibility levels {90%, 95%, 99%}.

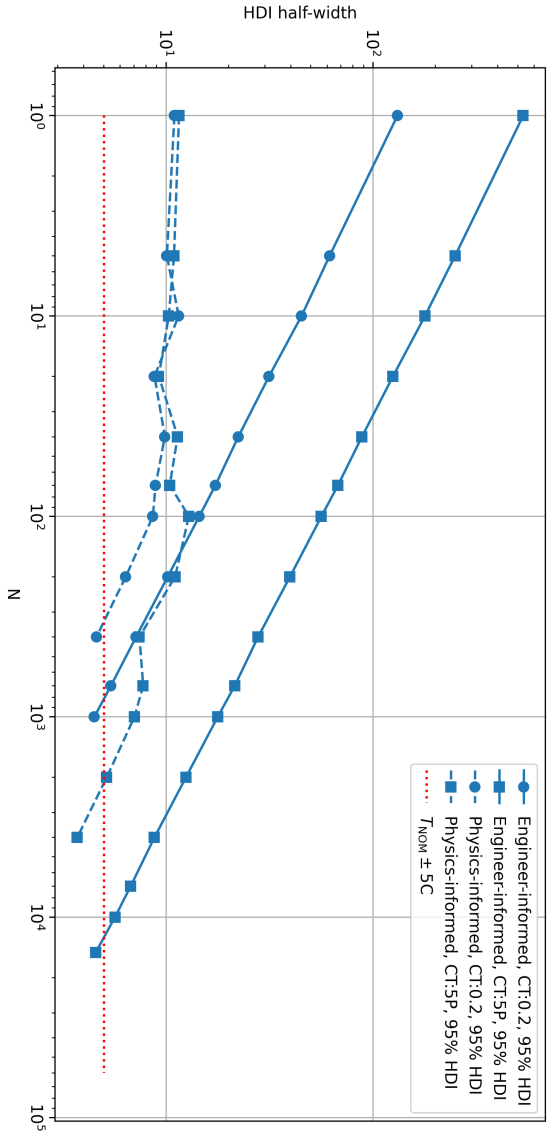


(b) HDI half-width versus number of measurements for different prior choices and accuracy classes: {CT(5P) & VT(0.2S), CT(0.1) & VT(0.2S)}.

Figure 5.16: Contraction of the posterior HDI half-width with increasing number of independent measurements. Comparisons are shown across prior assumptions, credibility levels, and measurement accuracy classes.

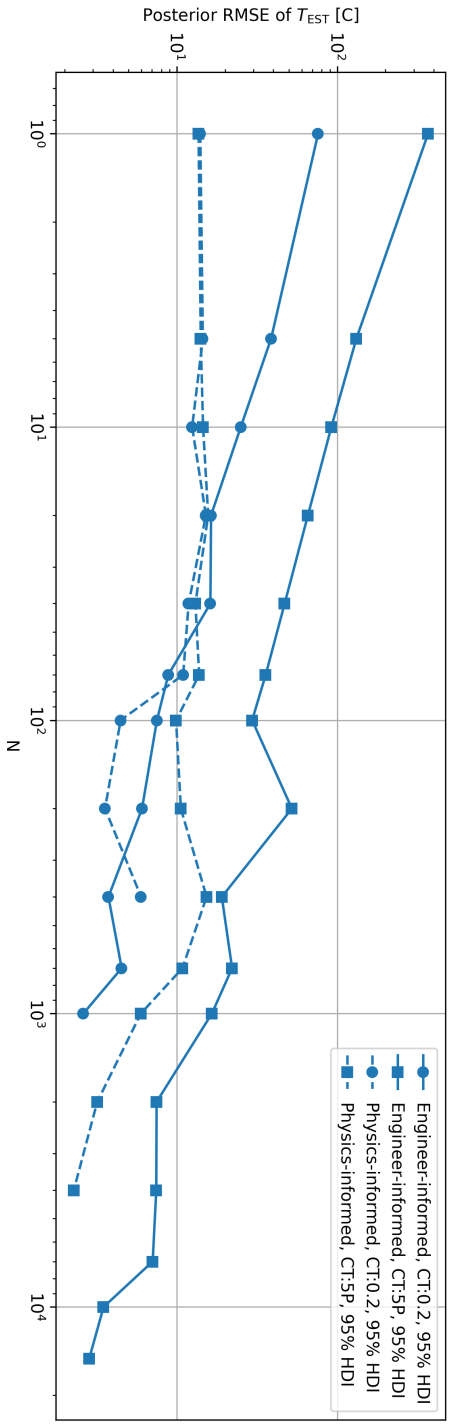


(a) Posterior RMSE vs number of measurements

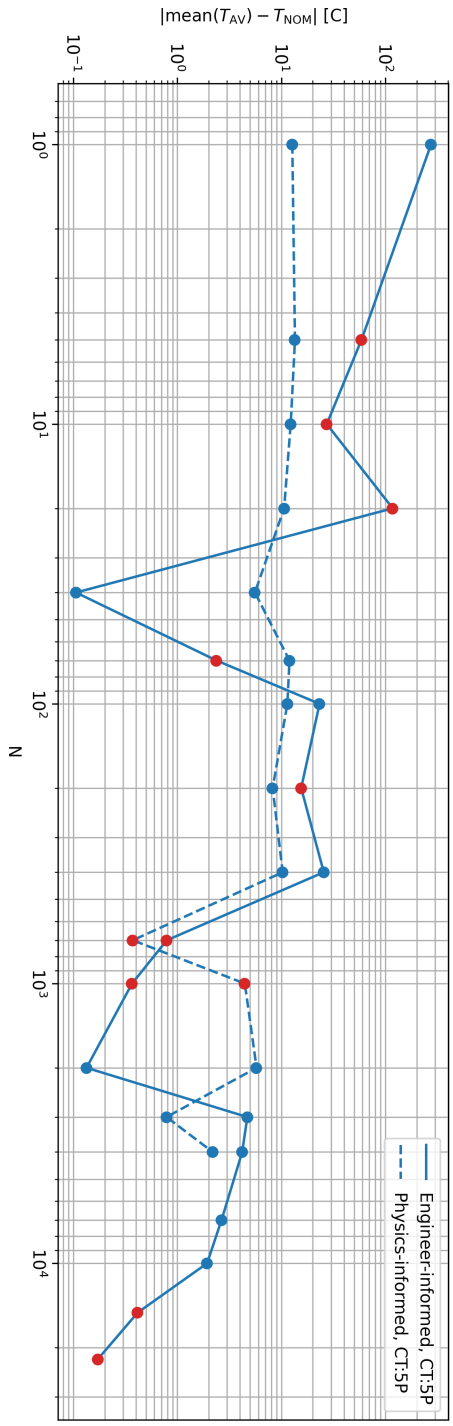


(b) Absolute temperature difference vs number of measurements

Figure 5.17: Comparisons of posterior RMSE and absolute temperature difference over number of measurements for accuracy classes CT(5P) VT(0.2S) as well as CT(0.1) VT(0.2S). Red markers in absolute temperature difference figure indicate temperature underestimation, a negative temperature difference in other words.

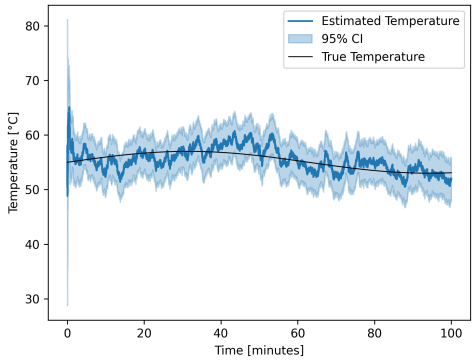


(a) Baseline.

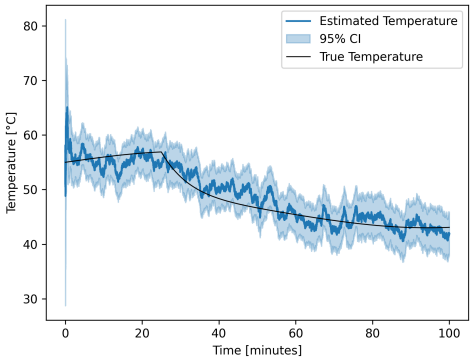


(b) Convective-driven cooling.

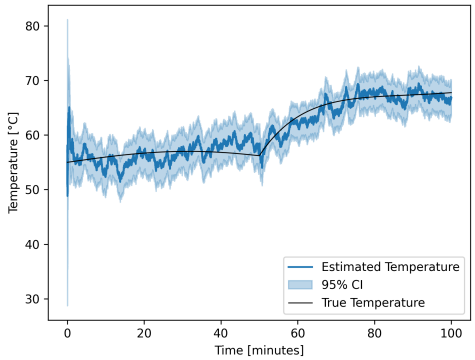


(c) Current-driven heating.

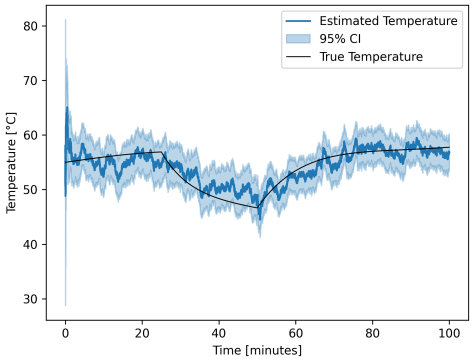


(d) Combination-driven changes.

Figure 5.18: Estimated temperatures over 100 minutes for all dynamic measurement cases. The estimated temperature is compared against the true temperature trajectory, and confidence intervals derived from the state covariance matrix are presented.

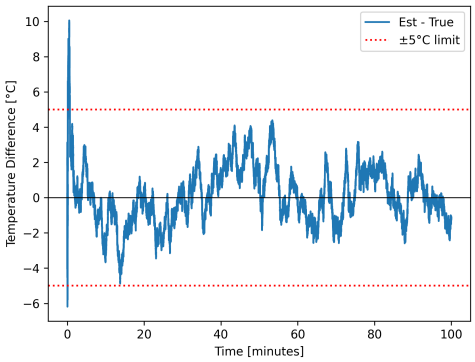


(a) Baseline.

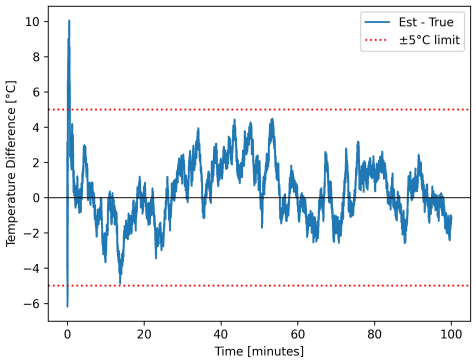


(b) Convective-driven cooling.

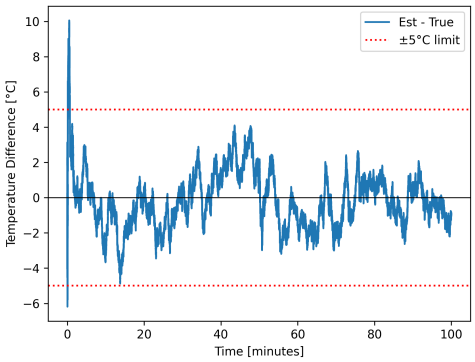


(c) Current-driven heating.

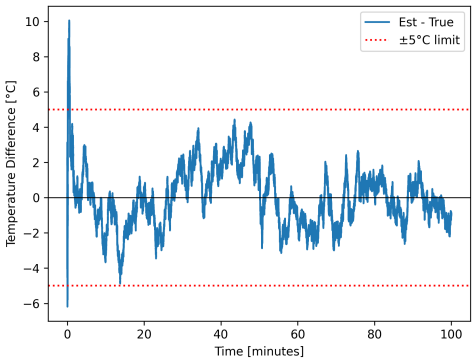


(d) Combination-driven changes.

Figure 5.19: Estimated temperature differences over 100 minutes for all dynamic measurement cases.

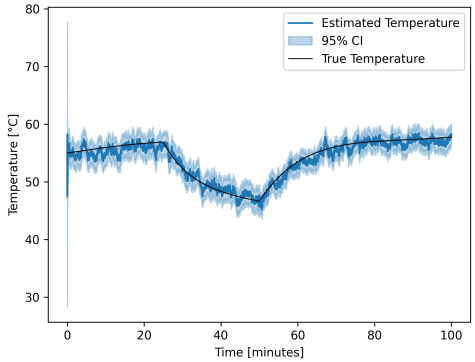


(a) Temperature estimate and 95 % confidence interval.

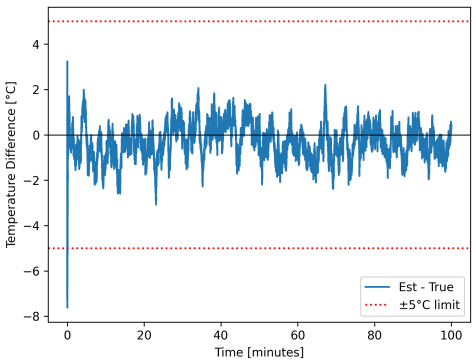


(b) Temperature difference and ±5 °C accuracy bounds.

Figure 5.20: Temperature estimate and difference for combination-driven changes when using accuracy classes CT(0.1) VT(0.2S) and measurement period length of 100 minutes.

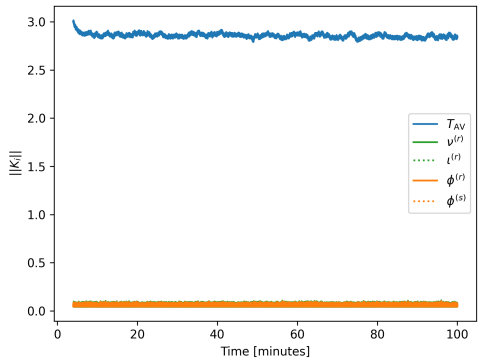


(a) Baseline.

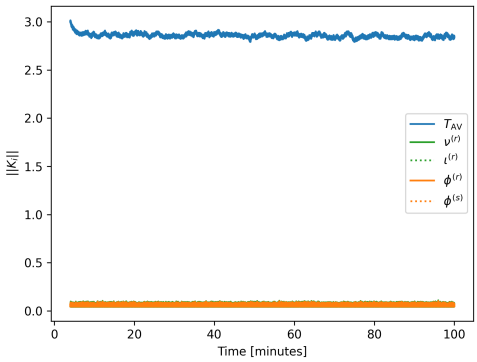


(b) Convection-driven cooling.

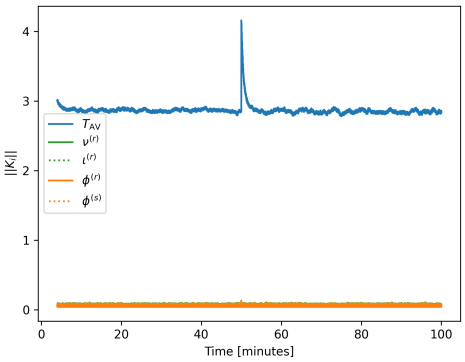


(c) Current-driven heating.

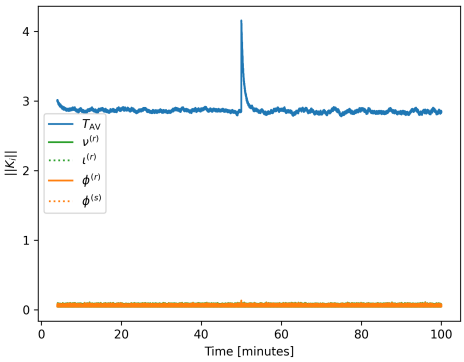


(d) Combination-driven changes.

Figure 5.21: Kalman gain per state for the different cases when using accuracy classes CT(5P) and VT(0.2S) and measurement period length of 100 minutes.

cantly shorter measurement periods greatly reduces estimate accuracy, see Figure 5.22. The beginning of the measurement period is more clearly shown, which makes it evident that initially, estimates are widely inaccurate. Furthermore, estimates are even less responsive to the changes occurring due to current magnitude steps.

For all cases, measurement period lengths, and accuracy classes the RMSE and MAE values, as well as average temperature variance, are brought forth in Table 5.3. The effect of measurement period lengths and accuracy classes are there shown, where it can be seen that increased accuracy leads to lower errors and variances, while shorter measurement period lengths significantly increases errors and variances.

Table 5.3: Comparison of RMSE, MAE and temperature variance for all tested dynamic cases, using all measurement period lengths and accuracy classes.

| Case | $m$ | CT(5P) | | | CT(0.1) | | |
|---|---|---|---|---|---|---|---|
| | | RMSE | MAE | Variance | RMSE | MAE | Variance |
| Baseline | 100 | 1.62 | 1.28 | 1.94 | 0.86 | 0.68 | 1.05 |
| | 10 | 2.08 | 1.85 | 2.27 | 1.09 | 0.78 | 1.11 |
| | 1 | 4.58 | 4.12 | 4.59 | 2.61 | 2.24 | 1.63 |
| Convection | 100 | 1.72 | 1.36 | 1.94 | 0.85 | 0.68 | 1.05 |
| | 10 | 2.55 | 2.06 | 2.27 | 1.10 | 0.82 | 1.11 |
| | 1 | 4.44 | 3.88 | 4.59 | 2.52 | 2.07 | 1.63 |
| Current | 100 | 1.59 | 1.25 | 1.78 | 0.83 | 0.66 | 0.96 |
| | 10 | 2.41 | 2.24 | 2.13 | 1.14 | 0.84 | 1.02 |
| | 1 | 4.47 | 3.90 | 4.40 | 2.52 | 2.06 | 1.56 |
| Combination | 100 | 1.59 | 1.25 | 1.78 | 0.83 | 0.66 | 0.96 |
| | 10 | 2.41 | 2.24 | 2.13 | 1.14 | 0.84 | 1.02 |
| | 1 | 4.47 | 3.90 | 4.40 | 2.52 | 2.06 | 1.56 |

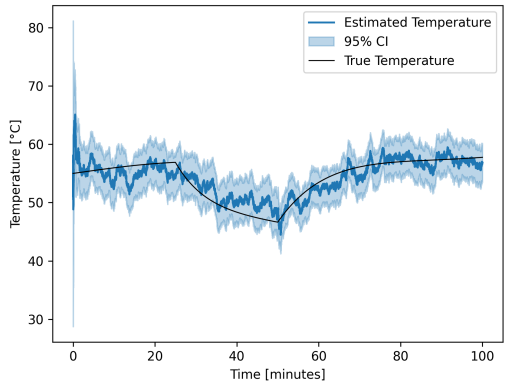


(a) Estimated temperature with confidence bounds (100 min window).

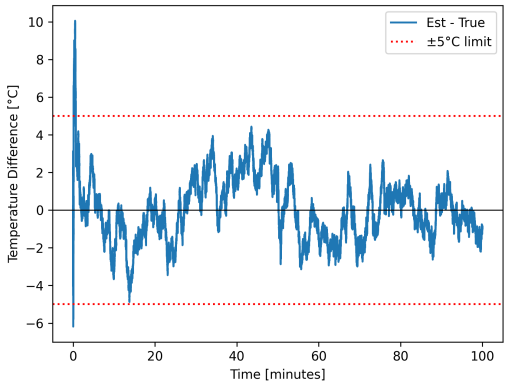


(b) Temperature estimation error with confidence bounds (100 min window).

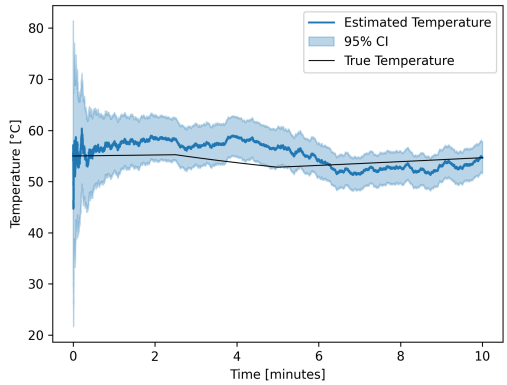


(c) Estimated temperature with confidence bounds (10 min window).

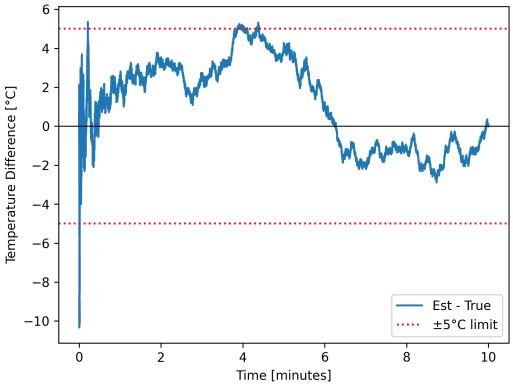


(d) Temperature estimation error with confidence bounds (10 min window).

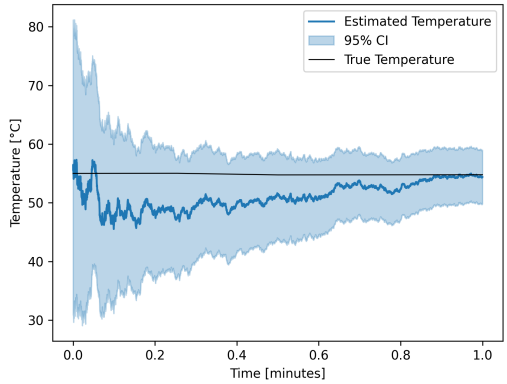


(e) Estimated temperature with confidence bounds (1 min window).

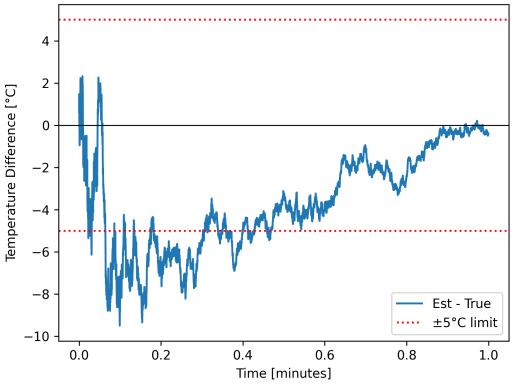


(f) Temperature estimation error with confidence bounds (1 min window).

Figure 5.22: Temperature estimates and associated confidence bounds for combination-driven dynamic changes, evaluated over 100, 10, and 1 minute aggregation windows. Instrument transformer accuracy classes CT(5P) and VT(0.2S) are applied.

# 6 Discussion

The purpose of this thesis was to assess the feasibility of inferring conductor temperature from phasor measurements under realistic uncertainty. This chapter synthesizes the results with respect to measurement uncertainty, inference methodology, and model assumptions.

## 6.1 Model and Measurement Drivers of Temperature Uncertainty

The temperature estimation uncertainty is governed by a combination of modelling assumptions and the structure of the measurement chain.

A foundational assumption in the model is the linear approximation of the temperature-resistance relationship. This introduces a second-order error with respect to the deviation between the average conductor temperature and the chosen reference temperature. For the reference temperature used in this thesis, $T_{\text{ref}} = 20$, when operating close to $T_{\text{MO}}$ one can expect errors upwards of 10 °C, as evident in Table 5.1. If the difference between reference and conductor temperature is reduced this error can be strongly suppressed, to the point where it can be regarded as negligible, see Table 5.2. Consequently, this dependence highlights that the validity of the linear approximation is conditional, and deviations from the intended operating range directly degrade temperature accuracy.

In contrast, the dominant contribution to temperature uncertainty originates from the estimation of power loss. Although voltage and current measurements exhibit narrow uncertainty ranges, the power loss is obtained as the difference between quantities of significantly larger magnitudes. This structural imbalance results in a large relative variance, even when absolute measurement errors are small. As demonstrated in Figures 5.1 and 5.3, overlap in the real-time average power distributions permits non-physical negative power loss estimates. These values propagate directly into the temperature inference, producing unrealistically low temperature estimates, as observed in Figures 5.2 and 5.4. This behaviour underscores a fundamental limitation of the current inference approach: the uncertainty is dominated by the formulation of the power loss rather than by the raw measurement precision itself.

### 6.1.1 Dominant Error Sources in the Measurement Chain

The relative influence of different measurement errors is determined by how they propagate through the power variance expression in Equation (5.6a). In particular, the angle difference $\phi$ between voltage and current governs whether magnitude or phase errors dominate the resulting temperature variance. For small values of $\phi$, the cosine factor approaches one while the sine factor becomes negligible, causing magnitude errors to be

the primary contributors. As $\phi$ increases, the contribution from phase errors grows, and angle uncertainty plays an increasingly significant role. This dependence is corroborated by the Sobol sensitivity indices. As shown in Equation (5.7) and Figure 5.7, which shows that the sensitivity of the temperature estimate is not fixed, but varies with the electrical operating point, reinforcing the conclusion that the power loss formulation inherently amplifies specific error sources depending on phase conditions.

Given the small magnitude of the underlying measurement errors, truncating multiplicative error terms at second order is justified. The Sobol indices show a pronounced reduction in magnitude between first- and second-order contributions, with higher-order terms diminishing further, see Figures 5.7 and 5.8. As a result, the total variance of the temperature estimate is overwhelmingly dominated by first-order effects, and non-linear error interactions have a negligible impact on the uncertainty observed in the results.

### 6.1.2 Information Limits of Single-Measurement Inference

The engineer-informed prior configurations reflect the limited information content of a single low-accuracy measurement, as the diffuse posterior lacks any significant information on temperature estimate as evident from Figure 5.10. This is the result from combining weak prior and likelihood information. The contractions shown through adjusting prior configurations as per Figures 5.10b and 5.10c may lead one to think that more information is gained, but that is not entirely the case. The physics-informed prior configuration leading to a posterior appearing similar to the prior as evident from Figure 5.11a itself implies that the contraction is driven primarily by the structural information embedded in the prior rather than by measurement evidence.

Similarly, the constraint posterior 5.11b indicates that the constraint acts mainly as a truncation mechanism, excluding non-physical regions without substantially increasing information density within the feasible range. Consequently, under single-measurement conditions with low-accuracy instrumentation, both approaches remain heavily dependent on their respective prior or constraint formulations, with the likelihood playing only a secondary role in shaping the posterior.

Using higher accuracy instrumentation does contract the posterior for all prior configurations, see Figure 5.12, indicating that the higher-accuracy measurements do contribute additional information to the inference. Nevertheless, the engineer-informed posterior remains highly diffuse, spanning a wide temperature interval that still includes physically implausible regions. Thus, while the likelihood influence has increased, it is not yet sufficient to localize the estimate in a practically meaningful sense from a single observation. As in the low-accuracy scenario, the likelihood contributes comparatively little information beyond what is already imposed structurally as evident from Figure 5.13. Consequently, even under improved measurement accuracy, single-measurement static estimation remains heavily prior- and constraint-dependent, with the likelihood playing

a secondary role in determining posterior concentration.

Beyond the identified error sources, the results also reveal a fundamental limitation related to the information content of a single measurement; variations in prior selection, imposed constraints, or accuracy class do not yield temperature estimates with sufficient reliability for practical use. This indicates that the uncertainty is not merely a consequence of suboptimal inference choices, but instead reflects an intrinsic limitation of single-measurement temperature estimation within the current framework.

Achieving a practically useful temperature estimate from a single measurement would require substantial improvements in measurement accuracy. As illustrated in Figure 5.14, the phasor measurement accuracy would need to be improved by approximately one by approximately 25 times, varying only slightly with prior configuration. For this case the likelihood becomes overwhelmingly informative, leading to a strong posterior contraction across all prior configurations. In contrast to the previous accuracy class configurations, the inference is no longer driven primarily by prior assumptions or constraint formulations. Instead, the measurement information dominates the posterior structure. This is particularly evident in the near equivalence between the engineer-informed prior with and without the soft physical constraint, whose posteriors become almost indistinguishable once the likelihood is sufficiently concentrated. The constraint no longer provides meaningful additional regularization, as the feasible region imposed by the data is already narrower than the constraint interval itself. The physics-informed prior does provide a tighter posterior, however, this increased precision now arises from alignment between prior structure and an already highly informative likelihood, rather than from prior dominance. Consequently, prior influence is reduced to a secondary refinement effect rather than a governing one.

Collectively, this indicates that the required instrument accuracy to achieve wanted precision far exceed incremental refinement and emphasizes that, under realistic measurement conditions, single-measurement inference is fundamentally constrained by insufficient information content rather than by modelling or estimation strategy alone.

## 6.2 Information Gain from Multiple Measurements

Incorporating multiple measurements over time significantly improves the accuracy of temperature estimation. However, this approach introduces additional assumptions and practical considerations that must be carefully evaluated, particularly regarding the temporal behaviour of the system and the validity of statistical models.

### 6.2.1 Static Bayesian Inference: Identifiability and Variance Reduction

Static Bayesian inference assumes that the underlying quantities remain constant over the measurement period. In practice, this assumption is rarely guaranteed, as environmen-

tal conditions, load profiles, or power supply may vary over time. However, the system exhibits a relatively slow response to such changes, and under certain circumstances, the stationarity assumption can be reasonable. Specifically, when using the highest measurement accuracy class together with physics-informed priors, the number of measurements required to achieve a precision of ±5 °C can fall below 500. At a sampling rate of 100 measurements per second, this corresponds to a measurement duration of approximately 5 seconds. Provided that no active changes occur in the load profile—such as a step in current magnitude—the static Bayesian method can deliver reliable temperature estimates within this time frame. On the other hand, if measurement accuracy can only be guaranteed to be at the required level for accuracy classes CT(5P) and VT(0.2S), then measurement time scales by almost a factor of 10, which reduces reliability of assumed static conditions.

Nevertheless, the reliability of static inference is fundamentally constrained by the trade-off between variance reduction from repeated measurements and the validity of the stationarity assumption. While multiple measurements reduce posterior variance relative to single-measurement inference, any temporal changes during the measurement period introduce potential bias. Careful consideration of system dynamics and measurement conditions is therefore essential when applying static Bayesian methods in practical applications.

### 6.2.2 Dynamic Estimation: Trade-offs and Benefits of Unscented Filtering

Relaxing the static assumption and adopting a dynamic estimation framework based on the UKF allows the model to accommodate non-linear variations in both temperature and measured quantities over time. Within this framework, the estimated temperature frequently falls within the wanted ±5 °C accuracy range. However, although the estimates are accurate, the associated posterior variance remains sufficiently large that a 95% confidence interval does not always guarantee adherence to the wanted precision. Despite this limitation, dynamic estimation offers a substantial improvement in reliability compared to static inference under time-varying conditions and represents a promising direction for further consideration.

However, the UKF requires time to properly initialize its state and all covariance matrices. As shown in Figure 5.22, this initialization can cause significant deviations from the true temperature over shorter time periods. The model compensates for this by producing a considerably wider confidence interval. During this phase, the filter is also less responsive to abrupt measurement changes, as it has insufficient confidence in its predictions, making it harder to distinguish between true state changes and measurement noise.

The similarity of estimated temperature difference for all cases, as evident in Figure 5.19, indicates that rather than dynamic changes themselves, the biggest cause of estima-

tion inaccuracy are the measurement errors. Even abrupt changes in operating conditions, such as steps in current magnitude, only cause additional differences for a brief period of time. As seen in Figure 5.21, for the cases that include current steps there is a clear increase in Kalman gain at the point of time where the step occurs. This implies that the model can accurately account for the deviation between predictions and measurements, and from that decrease the trust in its prediction and more rapidly converge toward the changed state.

## 6.3 Influence of Modelling Choices on Inference Results

The temperature inference results are sensitive to a number of modelling choices. These include the selection of prior distributions, the representation of error likelihoods, and the interaction between model assumptions and measurement availability. Each of these choices can have a significant impact on posterior distributions and the reliability of inferred temperatures.

### 6.3.1 Thermal and Electrical Properties

The variance of the estimated temperature is strongly dependent on the current magnitude. As indicated by Equation (5.6a), the temperature variance is proportional to $\iota^{-2}$, implying that temperature estimation improves with increasing current magnitude. This suggests that, all else being equal, transmission line models with higher static ampacities would be more favourable for phasor-based temperature estimation. However, higher static ampacity is typically associated with a lower AC resistance, which in turn increases the temperature variance. The opposing effects of increased operating current and reduced resistance therefore counterbalance each other. As a result, the temperature variance remains approximately constant across the studied transmission line models when evaluated at their respective expected operating current levels, as illustrated in Figure 5.5.

### 6.3.2 Prior Distributions and Physical Constraints

The choice of prior strongly influences the posterior distribution, particularly when the number of available measurements is limited. As shown in Figure 5.10a, the use of an engineering-informed prior results in a very wide posterior, as each measurement error is propagated in full, leading to substantial uncertainty in the inferred temperature.

Applying a soft physical constraint to restrict the posterior to a plausible temperature interval does not substantially improve inference for a single measurement. As illustrated in Figure 5.10c, although the constraint limits the posterior to a reasonable range, the lack of informative measurement data causes the posterior mass to remain nearly uni-

form within the interval $[T_{\min}, T_{\max}]$, rendering it impractical for meaningful temperature estimation.

Physics-informed priors, by contrast, lead to a substantial contraction of the posterior distribution. When only a few measurements are available, the posterior probability mass is concentrated near the prior temperature, resulting in significantly reduced variance compared to engineering-informed priors and soft constraints, leading to a more precise albeit inaccurate estimate. As the number of measurements increases, the influence of the prior gradually diminishes and the posterior shifts toward a more accurate estimate of the nominal temperature. In this regime, the deterministic physical relationships between measured quantities suppress the propagation of measurement noise, thereby reducing posterior variance. This effect substantially lowers the number of measurements required to meet the target estimation accuracy and precision compared to approaches that rely solely on weakly informative priors. Further benefits from choosing a physics-informed prior with a skewed-normal temperature prior is that the model heavily encourages temperature overestimation, as evident in Figure 5.17b.

### 6.3.3 Error Likelihood Assumptions

Assumptions regarding the error likelihood also play a critical role in inference quality. Both Bayesian and UKF methods assume that errors are zero-mean and normally distributed. In reality, as shown in Figures 5.1 and 5.3, the error distributions deviate from normality and exhibiting bounded support. Approximating these errors as normal distributions introduces additional inaccuracies: the normal distribution places more probability mass near the nominal value and allows longer tails, which can misrepresent the true uncertainty of the measurement.

Alternative likelihood models, such as Beta distributions fitted to the computed error KDEs, could provide a more accurate representation. However, this introduces technical challenges for sampling-based methods, e.g., HMC, as Beta distributions are defined on a bounded interval. Sharp edges at the support boundaries can cause divergence or spikes in the posterior. This could perhaps be mitigated using suitable transforms to map the Beta distribution to the real line.

Another potential approach is to construct likelihoods based on the amplitude of real power rather than voltage and current. By aggregating multiple measurement errors, the resulting distribution approximates a normal distribution more closely, improving the fit of the likelihood. This comes at the cost of reduced observability: power measurements alone provide weaker information about underlying quantities, increasing the dependence on priors. This would furthermore potentially limit the effectiveness of physics-informed priors such as the pi-model, as they strictly require current and voltage amplitudes separately, the same quantities that would have reduced observability in this approach.

### 6.3.4 Interaction Between Model Choices and Measurement Availability

Finally, the interaction between modelling assumptions and the source of measurements can influence the perceived inference accuracy. In this thesis, measurements used for Bayesian inference and UKF are generated from the pi-model, which is also employed as the basis for priors and update sequences. This circularity may lead to artificially improved performance compared to using real-world measurements, where model mismatch would likely increase uncertainty.

Assessing the robustness of the inference framework to true measurements is beyond the scope of this thesis. Nevertheless, future work should evaluate the sensitivity of Bayesian and Kalman-based methods to real measurement data to determine how well these modelling choices translate to practical applications.

## 6.4 Method Performance Comparison

Comparing static and dynamic phasor-based temperature estimation with the known accuracy of weather-based DLR demonstrates that phasor-based methods have the potential to estimate average conductor temperature with similar precision. As shown in Figure 5.17a, the RMSE of static estimates trends toward zero as the number of measurements increases, indicating that under sufficiently stable conditions, static phasor-based inference can achieve very low errors.

Table 5.3 shows that using the highest accuracy class, CT(0.1), the RMSE of UKF estimates reach values as low as 0.86, which is comparable to the current state of weather-based DLR, for which presented RMSE values are between 1.5-2.5. However, the weather-based methods indicate high confidence for the estimates, which is an are where they UKF does not perform as well. In contrast, the static estimation indicates that under the right conditions, phasor-based DLR can reach precisions even exceeding those of current weather-based DLR methods.

It is important to note that this comparison comes with trade-offs. Weather-based DLR provides temperature and ampacity estimates at high spatial resolution along the line, whereas phasor-based DLR produces only an average temperature estimate. Additionally, the RMSE values reported here are based on synthetic measurements and do not account for modelling errors discussed in Section 5.1, which would likely increase estimation uncertainty in practice.

Overall, these results suggest that phasor-based DLR may be able to achieve accuracy comparable to weather-based methods under idealized conditions, but further work is required to evaluate performance under realistic measurements and modelling uncertainties.

## 6.5 Limitations and Directions for Future Work

This thesis has investigated the feasibility and limitations of inferring conductor temperature from phasor-based measurements, with particular emphasis on uncertainty propagation, information content, and Bayesian inference strategies. While the presented results demonstrate that meaningful temperature estimation is possible under specific modelling and measurement conditions, they also reveal fundamental constraints related to measurement realism, modelling assumptions, and inference structure. This section contextualizes the contributions of this work by outlining their limitations and identifying directions for future research that are necessary to address the identified gaps and advance phasor-based dynamic line rating toward practical deployment.

### 6.5.1 Measurement Realism

A key limitation of the presented results lies in the assumed uncertainty levels of the secondary measurement circuits. Reducing secondary circuit uncertainty to the same order of magnitude as transformer errors is not currently supported by any established standard and may be difficult to guarantee in practice. Nevertheless, if such accuracy can be achieved, the estimation performance demonstrated in this thesis remains valid.

Future work should therefore focus on characterizing realistic uncertainty levels for secondary circuits and assessing how deviations from the assumed accuracy affect temperature inference. Experimental validation using real measurement hardware would be particularly valuable in determining whether the assumed error bounds are attainable in operational environments.

### 6.5.2 Prior Information

The engineering-informed priors used in this work are constructed as uniform distributions spanning $\pm 10\%$ around nominal values. While this reflects limited prior knowledge, it results in weakly informative priors that contribute little to posterior contraction. Improved prior knowledge—such as tighter bounds derived from historical data or auxiliary measurements—could significantly enhance inference performance, in a manner similar to the physics-informed priors examined in this thesis.

Additionally, soft physical constraints were in this thesis applied exclusively to the temperature posterior. A promising direction for future research is to extend such constraints to other physical quantities, including voltage drop and power loss, which also possess predictable behaviour based on system physics. Applying constraints at multiple levels of the model may enable posterior contraction while preserving physical stability, thereby improving inference reliability beyond what is achieved by constraining temperature alone.

### 6.5.3 Random versus Systematic Measurement Errors

All error sources considered in this thesis are assumed to be random. In practice, some measurement errors may instead be systematic, which would violate the assumptions underlying both the Bayesian inference and Kalman filtering frameworks employed.

For static temperature inference, systematic errors could potentially be addressed by modifying the likelihood model to include bias terms or offset parameters. Estimating such offsets jointly with temperature would allow the inference framework to remain valid even in the presence of persistent measurement bias. Extending this approach to dynamic estimation remains an open challenge and warrants further investigation.

### 6.5.4 Considerations for Real-World Deployment

Several practical aspects of dynamic estimation remain unresolved. In particular, the current approach for selecting the initial process noise covariance $\mathbf{Q}_0$ and the scaling factor $\gamma_k$ relies on empirical tuning. Estimation results are highly affected by these parameter choices, so developing systematic methods for determining these parameters would significantly improve robustness and reproducibility. One potential avenue is the use of multiple scaling factors that adapt based on the discrepancy between model predictions and measurements.

Finally, the accuracy of phasor-based temperature inference is strongly dependent on the combined measurement quality at both measurement stations. For engineering-informed priors, the variance of the power loss estimate is directly influenced by the variances at each station, making balanced improvements in measurement accuracy on both sides essential for meaningful uncertainty reduction. While physics-informed priors can partially mitigate asymmetric measurement quality through deterministic coupling between measurements, achieving high-confidence temperature estimates ultimately benefits from improved accuracy at all measurement locations. Future research should therefore prioritize coordinated improvements in measurement accuracy across stations and investigate how such enhancements interact with physics-informed inference frameworks.

# 7 Conclusion

This thesis has investigated the feasibility of estimating conductor temperature from phasor-based measurements, with particular emphasis on uncertainty propagation, information content, and Bayesian inference frameworks. By systematically comparing static and dynamic estimation approaches, the work clarifies the conditions required for phasor-based DLR to achieve performance comparable to established weather-based methods.

The results demonstrate that temperature inference from a single phasor measurement is fundamentally limited by variance amplification in the power loss formulation. Even with narrow voltage and current uncertainties, the resulting temperature estimates require measurement precision that exceeds what is currently achievable in practice. This limitation is structural and cannot be mitigated through inference strategy alone.

Incorporating multiple measurements substantially increases the available information and enables accurate temperature estimation under favourable conditions. Static Bayesian inference achieves the wanted precision of $\pm 5°C$ when high-accuracy measurements are combined with physics-informed priors and sufficiently stationary operating conditions. Furthermore, the physics-informed priors significantly reduces the risk of underestimating temperature. In such regimes, static phasor-based inference can achieve accuracy comparable to, and in some cases exceeding, that of weather-based DLR, albeit with the limitation that only an average conductor temperature is estimated.

For time-varying operating conditions, dynamic estimation using the UKF removes the stationarity requirement and successfully captures non-linear temperature dynamics. While the resulting mean temperature estimates frequently fall within the desired accuracy range, the posterior uncertainty remains too large to guarantee it with high confidence. This behaviour reflects a fundamental trade-off between model flexibility and estimation certainty, further magnified during shorter measurement period lengths.

Overall, the findings indicate that the primary limitations of phasor-based temperature inference arise not from insufficient model complexity, but from the interaction between measurement uncertainty, inference assumptions, and information availability. Comparisons with weather-based DLR highlight that phasor-based methods are competitive in terms of accuracy under controlled static conditions, but that dynamic conditions do not reach the same level of precision. Advancing phasor-based DLR toward practical deployment will therefore require coordinated improvements in measurement accuracy, refined uncertainty modelling, further knowledge on the nature of measurement errors, and enhanced exploitation of physical structure within both static and dynamic inference frameworks.

# References

[1] E. Fernandez et al. "Review of Dynamic Line Rating Systems for Wind Power Integration". In: *Renewable and Sustainable Energy Reviews* 53 (Jan. 2016), pp. 80–92. ISSN: 13640321. DOI: 10.1016/j.rser.2015.07.149. URL: https://linkinghub.elsevier.com/retrieve/pii/S1364032115007960 (visited on 12/29/2025).

[2] David L. Alvarez et al. "Methodology to Assess Phasor Measurement Unit in the Estimation of Dynamic Line Rating". In: *IET Generation, Transmission & Distribution* 12.16 (Sept. 2018), pp. 3820–3828. ISSN: 1751-8687, 1751-8695. DOI: 10.1049/iet-gtd.2017.0661. URL: https://ietresearch.onlinelibrary.wiley.com/doi/10.1049/iet-gtd.2017.0661 (visited on 10/20/2025).

[3] *Thermal Behaviour of Overhead Conductors*. Technical TB207. CIGRE, 2022.

[4] Sanna Uski. "Estimation Method for Dynamic Line Rating Potential and Economic Benefits". In: *International Journal of Electrical Power & Energy Systems* 65 (Feb. 1, 2015), pp. 76–82. DOI: 10.1016/j.ijepes.2014.09.034.

[5] A.G. Phadke and J.S. Thorp. *Synchronized Phasor Measurements and Their Applications*. Power Electronics and Power Systems. Boston, MA: Springer US, 2008. ISBN: 978-0-387-76535-8 978-0-387-76537-2. DOI: 10.1007/978-0-387-76537-2. URL: http://link.springer.com/10.1007/978-0-387-76537-2 (visited on 12/29/2025).

[6] *IEEE Standard for Calculating the Current-Temperature Relationship of Bare Overhead Conductors*. Standard 738. IEEE Power and Energy Society, 2023.

[7] D. M. Newbery. "Reforming Competitive Electricity Markets to Meet Environmental Targets | Faculty of Economics". In: *Cambridge Working Papers in Economics* (2011). URL: https://www.econ.cam.ac.uk/publications/cwpe/1154 (visited on 12/29/2025).

[8] Lotfi Belkhir and Ahmed Elmeligi. "Assessing ICT Global Emissions Footprint: Trends to 2040 & Recommendations". In: *Journal of Cleaner Production* 177 (Mar. 10, 2018), pp. 448–463. ISSN: 0959-6526. DOI: 10.1016/j.jclepro.2017.12.239. URL: https://www.sciencedirect.com/science/article/pii/S095965261733233X (visited on 12/29/2025).

[9] *Guide for Thermal Rating Calculations of Overhead Lines - Electra*. Technical Brochure TB601. CIGRE, 2015. URL: https://www.e-cigre.org/publications/detail/elt-278-4-guide-for-thermal-rating-calculations-of-overhead-lines.html (visited on 12/29/2025).

[10] *Sag-Tension Calculation Methods for Overhead Lines - Technical Brochures*. Technical Brochure TB324. CIGRE, 2016. URL: https://www.e-cigre.org/publications/detail/324-sag-tension-calculation-methods-for-overhead-lines.html (visited on 12/29/2025).

[11] *Guide For Selection of Weather Parameters For Bare Overhead Conductor Ratings*. Scribd. URL: https://www.scribd.com/document/458777917/CIGRE-Guide-for-Selection-of-Weather-Parameters-for-Bare-Overhead-Conductor-Ratings-pdf (visited on 02/11/2026).

[12] Raquel Martinez et al. "Dynamic Rating Management of Overhead Transmission Lines Operating under Multiple Weather Conditions". In: *Energies* 14.4 (Jan. 2021), p. 1136. ISSN: 1996-1073. DOI: 10.3390/en14041136. URL: https://www.mdpi.com/1996-1073/14/4/1136 (visited on 01/06/2026).

[13] Levente Rácz et al. "Performance Analysis of a Dynamic Line Rating System Based on Project Experiences". In: *Energies* 15.3 (Jan. 2022), p. 1003. ISSN: 1996-1073. DOI: 10.3390/en15031003. URL: https://www.mdpi.com/1996-1073/15/3/1003 (visited on 02/11/2026).

[14] Raúl Peña, Antonio Colmenar-Santos, and Enrique Rosales-Asensio. "Dynamic Line Rating: Technology and Future Perspectives". In: *Electronics* 14.14 (Jan. 2025), p. 2828. ISSN: 2079-9292. DOI: 10.3390/electronics14142828. URL: https://www.mdpi.com/2079-9292/14/14/2828 (visited on 02/11/2026).

[15] Di Shi et al. "Transmission Line Parameter Identification Using PMU Measurements". In: *European Transactions on Electrical Power* 21.4 (2011), pp. 1574–1588. ISSN: 1546-3109. DOI: 10.1002/etep.522. URL: https://onlinelibrary.wiley.com/doi/abs/10.1002/etep.522 (visited on 10/22/2025).

[16] *Phasor Measurement | Hitachi Energy*. URL: https://www.hitachienergy.com/products-and-solutions/substation-automation-protection-and-control/products/protection-and-control/phasor-measurement (visited on 01/02/2026).

[17] *Synchrophasor for Power Systems – Measurements*. Standard 118–1. IEC/IEEE, Dec. 2018.

[18] *Mättransformatorer Del 1: Allmänna Fordringar*. Standard. Svensk Standard, Nov. 16, 2009.

[19] *Mättransformatorer Del 2: Tilläggsfordringar För Strömtransformatorer*. Standard. Svensk Standard, Jan. 22, 2013.

[20] Elisabeth Lindberg. "The Overhead Line Sag Dependence on Weather Parameters and Line Current".

[21] George S. Fishman. *Monte Carlo: Concepts, Algorithms, and Applications*. Springer, 1996.

[22] Trevor Hastie, Robert Tibshirani, and Jerome Friedman. "Kernel Smoothing Methods". In: *The Elements of Statistical Learning: Data Mining, Inference, and Prediction*. Ed. by Trevor Hastie, Robert Tibshirani, and Jerome Friedman. New York, NY: Springer, 2009, pp. 191–218. ISBN: 978-0-387-84858-7. DOI: 10.1007/978-0-387-84858-7_6. URL: https://doi.org/10.1007/978-0-387-84858-7_6 (visited on 12/29/2025).

[23] "Bandwidth Selection in Kernel Density Estimation: A Review". In: *ResearchGate* (1999). URL: https://www.researchgate.net/publication/2316108_Bandwidth_Selection_in_Kernel_Density_Estimation_A_Review (visited on 12/29/2025).

[24] M van der Rijst, J Hugo, and A.J. vand der Merwe. "Performance of Confidence Intervals on Tha among Group Variance in the Unbalanced One-Factor Random Effects Model". In: ().

[25] Andrea Saltelli, ed. *Global Sensitivity Analysis: The Primer*. Chichester, England Hoboken, NJ: John Wiley, 2008. 1 p. ISBN: 978-0-470-05997-5 978-0-470-72518-4 978-0-470-72517-7. DOI: 10.1002/9780470725184.

[26] Andrew Gelman et al. "Bayesian Data Analysis Third Edition". In: ().

[27] José M. Bernardo. *Bayesian Theory*. Wiley Series in Probability and Statistics. Wiley, 2000.

[28] Christian P. Robert, ed. *The Bayesian Choice: From Decision-Theoretic Foundations to Computational Implementation*. Springer Texts in Statistics. New York, NY: Springer New York, 2007. ISBN: 978-0-387-71598-8 978-0-387-71599-5. DOI: 10.1007/0-387-71599-1.

[29] Radford M. Neal. *MCMC Using Hamiltonian Dynamics*. May 10, 2011. DOI: 10.1201/b10905. arXiv: 1206.1901 [stat]. URL: http://arxiv.org/abs/1206.1901 (visited on 12/26/2025).

[30] Michael Betancourt. *A Conceptual Introduction to Hamiltonian Monte Carlo*. July 16, 2018. DOI: 10.48550/arXiv.1701.02434. arXiv: 1701.02434 [stat]. URL: http://arxiv.org/abs/1701.02434 (visited on 12/26/2025). Pre-published.

[31] Matthew D Hoffman and Andrew Gelman. "The No-U-Turn Sampler: Adaptively Setting Path Lengths in Hamiltonian Monte Carlo". In: *Journal of Machine Learning Research* ().

[32] *Cholesky's Decomposition - an Overview | ScienceDirect Topics*. URL: https://www.sciencedirect.com/topics/engineering/choleskys-decomposition (visited on 01/03/2026).

[33] *PyMC*. PyMC project website. URL: https://www.pymc.io/welcome.html (visited on 12/26/2025).

# Appendices

## A Code

All numerical implementations have been done in Python and the code can be found at https://github.com/Kakdu/phasor_dlr.